

DUAL-FUNCTION HEATSINK ANTENNAS FOR HIGH-DENSITY THREE-
DIMENSIONAL INTEGRATION OF HIGH-POWER TRANSMITTERS

By

LANCE NICHOLAS COVERT

A DISSERTATION PRESENTED TO THE GRADUATE SCHOOL
OF THE UNIVERSITY OF FLORIDA IN PARTIAL FULFILLMENT
OF THE REQUIREMENTS FOR THE DEGREE OF
DOCTOR OF PHILOSOPHY

UNIVERSITY OF FLORIDA

2008

© 2008 Lance Nicholas Covert

To my parents, my brother and my wife

ACKNOWLEDGMENTS

I would like to thank my advisor Dr. Jenshan Lin for the opportunity to work under him and for his advice, encouragement, and mentoring throughout the process. I have truly enjoyed working for him over the years. I would also like to thank Dr. Huikai Xie, Dr. Henry Zmuda, and Dr. Fan Ren for their time and for being on my committee. All of the previous and current RFSOC group members up to date have helped in some way either technically or with comic relief and friendship, so I thank all of them. I would like to thank the Air Force Research Laboratory and Thomas Dalrymple for funding this project. The antenna measurements performed by Dan Janning at the AFRL are greatly appreciated. Mr. Bob Helsby of the Ansoft Corporation helped out by providing UF with Ansoft tools. I would also like to thank Shannon Chillingworth and all of the personnel in the EE office.

Finally, I would like to thank my wife, my brother and my parents for their encouragement and unconditional support. Without them it would not be possible. I would also like to thank my wife's family and my brother's family for their support.

TABLE OF CONTENTS

	<u>page</u>
ACKNOWLEDGMENTS	4
LIST OF TABLES	8
LIST OF FIGURES	9
ABSTRACT	18
CHAPTER	
1 INTRODUCTION	19
1.1 Introduction.....	19
1.2 3-D System-on-Chip (SOC) with Integrated 3-D Heatsink Antenna	20
1.3 Heatsink Antenna.....	21
2 BACKGROUND INFORMATION	24
2.1 Introduction.....	24
2.2 RF Transceivers and the Transmitter.....	24
2.3 Antenna-Related Parameters.....	26
2.3.1 Input Impedance and Reflected Power	27
2.3.2 Radiation Efficiency	30
2.3.3 Directivity	30
2.3.4 Gain.....	31
2.3.5 Friis Transmission Equation	32
2.4 Microstrip Patch Antennas.....	34
2.5 Thermal Issues	35
3 PIN-FIN HEATSINK ANTENNA AT 2.4 GHz.....	39
3.1 Introduction.....	39
3.2 Design Overview	40
3.2.1 Microstrip Patch Antenna Design and Simulation.....	40
3.2.2 Fabricated Patch and Heatsink Antenna	41
3.2.3 HFSS Model Description.....	43
3.3 Results and Measurements.....	44
3.3.1 Radiation Efficiency	44
3.3.2 Input Reflection Coefficient (S_{11}) and Bandwidth.....	47
3.3.3 Far-Field Radiation Patterns	50
3.3.4 E-Field Magnitude Plots	52
3.3.5 Summary of Results.....	53
3.4 Conclusion	54

4	EXTRUDED-FIN HEATSINK ANTENNAS AT 5.8 GHz.....	56
4.1	Introduction.....	56
4.2	Design Overview	56
4.2.1	Antenna Design.....	56
4.2.2	HFSS Model Description.....	59
4.3	Results and Measurements.....	60
4.3.1	Radiation Efficiency	60
4.3.2	Bandwidth and Return Loss.....	61
4.3.3	Far-Field Radiation Patterns	67
4.3.4	E-Field Plots.....	69
4.3.5	Summary of Results.....	72
4.4	Conclusion	74
5	FIN HEIGHT AND ORIENTATION EFFECTS OF EXTRUDED-FIN AND PIN-FIN HEATSINK ANTENNAS.....	75
5.1	Introduction.....	75
5.2	Simulation and Measurement Setup	75
5.2.1	Simulation Setup.....	75
5.2.2	Measurement Setup.....	79
5.3	Three-Finned Heatsink Antenna Results	79
5.3.1	Input Reflection Coefficient and Resonant Frequency Analysis.....	80
5.3.2	Antenna Parameters and Radiation Patterns.....	95
5.3.3	Fin Thickness Sweep	116
5.4	Two-Finned Heatsink Antenna Results	118
5.4.1	Resonant Frequency and Input Reflection Coefficient.....	118
5.4.2	Antenna Parameters	123
5.5	Multiple Fin Results.....	126
5.6	Pin-Fin Results.....	129
5.7	Summary of Results.....	133
5.8	Conclusion	134
6	BOXED AND CUBIC HEATSINK ANTENNAS.....	137
6.1	Introduction.....	137
6.2	Simulations and Results.....	137
6.2.1	Simulation Setup.....	137
6.2.2	Results of Boxed Heatsink Antenna Simulations.....	140
6.2.3	Results of Cubic Heatsink Antenna Simulations	148
6.2.4	Summary of Results.....	151
6.3	Conclusion	152
7	INTEGRATED POWER AMPLIFIER AND HEATSINK ANTENNA MODULE.....	153
7.1	Introduction.....	153
7.2	Description.....	153

7.3	Results.....	157
7.4	Conclusion	163
8	SUMMARY AND FUTURE WORK.....	164
8.1	Summary.....	164
8.2	Future Work.....	167
	LIST OF REFERENCES.....	169
	BIOGRAPHICAL SKETCH	173

LIST OF TABLES

<u>Table</u>		<u>page</u>
3-1	Comparison of antenna parameters (simulated)	45
3-2	Comparison of radiation efficiencies	47
3-3	Measured 10-dB bandwidth.....	48
4-1	Comparison of radiation efficiencies	61
4-2	Measured impedance bandwidth.....	63
4-3	Measured antenna Q	64
5-1	Antenna and heatsink dimensions for HFSS setup.....	76
5-2	Antenna parameters for the basic patch antenna (simulated)	80
5-3	Primary and alternate resonant frequencies associated used for frequency-tracking heatsink antenna parameters	113
6-1	Antenna dimensions for HFSS setup (simulated).....	138
7-1	Thermal conductivity of materials	155
7-2	Parameters used in gain measurement	159
7-3	Measured received power at various distances from PA/HSA module with corresponding calculated peak antenna gain.....	160

LIST OF FIGURES

<u>Figure</u>	<u>page</u>
1-1 Illustration of 3-D SOC structure with integrated heatsink antenna.....	20
1-2 Common heatsink types: a) extruded-fin heatsink and b) pin-fin heatsink	22
2-1 RF transceiver block diagram	25
2-2 Direct-conversion transmitter block diagram	26
2-3 Thevenin equivalent circuit of antenna.....	27
2-4 Antenna connected to source via a transmission line	30
2-5 Electrical equivalent circuit of heat flow from the device to the air.....	36
3-1 Planar dimensions of the patch antennas	41
3-2 FR4 square patch antenna designed at 2.4 GHz	42
3-3 Fabricated 2.4 GHz FR4 heatsink antenna	42
3-4 HFSS model of 2.4 GHz FR4 heatsink antenna	43
3-5 Measured S_{11} for 2.4 GHz antennas.....	49
3-6 Return loss ($ S_{11} $ (dB)) of the 2.4 GHz patch antenna and heatsink antenna without tuning stub.....	50
3-7 Return loss ($ S_{11} $ (dB)) of the 2.4 GHz patch antenna and heatsink antenna with tuning stub.....	50
3-8 E-plane gain patterns of 2.4 GHz patch antenna.....	51
3-9 E-plane gain patterns of 2.4 GHz heatsink antenna.....	52
3-10 E-field magnitude plot in E-plane for 2.4 GHz basic patch.....	53
3-11 E-field magnitude plot in E-plane for 2.4 GHz HS antenna.....	53
4-1 Fabricated 5.8 GHz FR4 square patch antenna.....	57
4-2 Fabricated heatsink antenna with fins parallel to the non-radiating edges (FPNRE) of the patch.....	58
4-3 Fabricated heatsink antenna with fins parallel to the non-radiating edges (FPNRE) of the patch.....	58

4-4	HFSS model of heatsink antenna with fins parallel to the non-radiating edges (FPNRE) of the patch.....	59
4-5	HFSS model of heatsink antenna with fins parallel to the radiating edges (FPRE) of the patch.....	60
4-6	Measured input impedance for the basic patch antenna, the heatsink antenna (FPNRE) without a tuning stub, and the heatsink antenna (FPNRE) with a tuning stub.....	62
4-7	Measured return loss of the patch and heatsink antennas.....	63
4-8	Radiation efficiency vs. frequency.....	66
4-9	Peak directivity (dBi) vs. frequency.....	66
4-10	Peak gain (dBi) vs. frequency.....	67
4-11	E-plane gain patterns.....	68
4-12	H-plane gain patterns.....	69
4-13	E-field vector plot in E-plane for basic patch antenna at 5.80 GHz.....	70
4-14	E-field vector plot in E-plane for heatsink antenna with Fins PNRE at 5.80 GHz.....	70
4-15	E-field vector plot in E-plane for heatsink antenna with Fins PRE at 5.80 GHz.....	71
4-16	E-field magnitude plot in E-plane for 5.8 GHz basic patch.....	71
4-17	E-field magnitude plot in E-plane for the FPNRE case at 5.8 GHz.....	72
4-18	E-field magnitude plot in E-plane for the FPRE case at 5.8 GHz.....	72
5-1	HFSS model of 3-finned 5.8 GHz heatsink antenna with fins parallel to non-radiating edges.....	77
5-2	HFSS model of 5.8 GHz heatsink antenna with fins parallel to radiating edges.....	77
5-3	Cross-section of patch antenna along the length showing electric field lines.....	77
5-4	HFSS model of 2-finned 5.8 GHz heatsink antenna with fins parallel to non-radiating edges.....	78
5-5	HFSS model of 2-finned 5.8 GHz heatsink antenna with fins parallel to non-radiating edges.....	78
5-6	Fabricated 5.8 GHz heatsink antennas for fin height sweep.....	79

5-7	S_{11} of 5.8 GHz basic patch antenna	81
5-8	S_{11} of 5.8 GHz heatsink antenna with fin height = 12 mm along the radiating edges (FPRE)	81
5-9	S_{11} of 5.8 GHz heatsink antenna with fin height = 16 mm along the non-radiating edges (FPNRE)	82
5-10	S_{11} of FPNRE with fin height = 2 mm	82
5-11	S_{11} of FPNRE with fin height = 6 mm	83
5-12	S_{11} of FPNRE with fin height = 12 mm	83
5-13	S_{11} of FPNRE with fin height = 16 mm	83
5-14	S_{11} of FPNRE with fin height = 20 mm	84
5-15	S_{11} of FPRE with fin height = 2 mm	84
5-16	S_{11} of FPRE with fin height = 6 mm	84
5-17	S_{11} of FPRE with fin height = 12 mm	85
5-18	S_{11} of FPRE with fin height = 16 mm	85
5-19	S_{11} of FPRE with fin height = 20 mm	85
5-20	Measured and simulated resonant frequencies of the 3-finned heatsink antenna with fins parallel to the non-radiating edges (FPNRE)	90
5-21	Measured and simulated resonant frequencies of the 3-finned heatsink antenna with fins parallel to the radiating edges (FPRE)	90
5-22	E-field vector plots showing primary (left, E-plane) and alternate resonances (right, H-plane) of 3-fin extruded-fin heatsink antenna with 12 mm fins parallel to the non-radiating edges (FPNRE)	91
5-23	E-field vector plots showing primary (left, E-plane) and alternate resonances (right, H-plane) of 2-fin extruded-fin heatsink antenna with 12 mm fins parallel to the non-radiating edges (FPNRE)	91
5-24	E-field vector plots showing primary (left, E-plane) and alternate resonances (right, E-plane) of 3-fin extruded-fin heatsink antenna with 12 mm fins parallel to the radiating edges (FPRE)	92
5-25	E-field vector plots showing primary (left, E-plane) and alternate resonances (right, E-plane) of 2-fin extruded-fin heatsink antenna with 12 mm fins parallel to the radiating edges (FPRE)	92

5-26	Equivalent circuit model of 3-fin extruded-fin heatsink antenna with fins parallel to the non-radiating edges (FPNRE).....	93
5-27	Comparison of S_{11} given by equivalent circuit model and HFSS electromagnetic solver of 3-fin extruded-fin heatsink antenna (FPNRE) with 14-mm fins	93
5-28	Comparison of return loss given by equivalent circuit model and HFSS electromagnetic solver of 3-fin extruded-fin heatsink antenna (FPNRE) with 14-mm fins.....	94
5-29	Equivalent circuit model of 3-fin extruded-fin heatsink antenna with fins parallel to the radiating edges (FPRE).....	94
5-30	Comparison of S_{11} given by equivalent circuit model and HFSS electromagnetic solver of 3-fin extruded-fin heatsink antenna (FPRE) with 12-mm fins	95
5-31	Comparison of return loss given by equivalent circuit model and HFSS electromagnetic solver of 3-fin extruded-fin heatsink antenna (FPRE) with-12 mm fins.....	95
5-32	Simulated radiation efficiency vs. fin height for 3-finned antennas at 5.80 GHz	97
5-33	Measured radiation efficiency vs. fin height for 3-finned antennas at 5.80 GHz.....	97
5-34	Simulated peak directivity vs. fin height for 3-finned antennas at 5.80 GHz.....	100
5-35	Measured peak directivity vs. fin height for 3-finned antennas at 5.80 GHz.....	100
5-36	Surface currents on the heatsink fins for the 3-fin FPNRE case (left) and the 3-fin FPRE case (right).....	101
5-37	Simulated 3-D radiation patterns for fin height sweep of 3-finned antenna with fins parallel to the non-radiating edges (FPNRE) at 5.80 GHz	102
5-38	Simulated 3-D radiation patterns for fin height sweep of 3-finned antenna with fins parallel to the radiating edges (FPRE) at 5.80 GHz.....	102
5-39	Simulated 2-D gain patterns (linear scale) of extruded-fin heatsink antenna with fins parallel to the non-radiating edges (FPNRE) at various fin heights at 5.80 GHz.....	103
5-40	Simulated 2-D gain patterns (linear scale) of extruded-fin heatsink antenna with fins parallel to the radiating edges (FPRE) at various fin heights at 5.80 GHz.....	103
5-41	Simulated 2-D gain patterns (dB scale) of extruded-fin heatsink antenna with fins parallel to the non-radiating edges (FPNRE) at various fin heights at 5.80 GHz.....	104
5-42	Simulated 2-D gain patterns (dB scale) of extruded-fin heatsink antenna with fins parallel to the radiating edges (FPRE) at various fin heights at 5.80 GHz.....	104

5-43	Measured 2-D gain patterns (dB scale) of extruded-fin heatsink antenna with fins parallel to the non-radiating edges (FPNRE) at various fin heights at 5.80 GHz.....	105
5-44	Measured 2-D gain patterns (dB scale) of extruded-fin heatsink antenna with fins parallel to the radiating edges (FPRE) at various fin heights at 5.80 GHz.....	105
5-45	Coordinate system for 3-D far-zone antenna array factor [Bal]	106
5-46	3-D far-zone array factor for 2 elements spaced $\lambda/2$ apart along the x-axis with an excitation phase difference of 180 degrees.....	106
5-47	3-D far-field dipole pattern	107
5-48	Radiation pattern of two-element dipole array resulting from pattern multiplication of array factor and single element patterns.....	107
5-49	Simulated peak gain vs. fin height for 3-finned antennas at 5.80 GHz	109
5-50	Measured peak gain vs. fin height for 3-finned antennas at 5.80 GHz.....	109
5-51	Frequency-tracking comparison of simulated radiation efficiency vs. fin height for 3-fin FPNRE heatsink antenna.....	110
5-52	Frequency-tracking comparison of simulated radiation efficiency vs. fin height for 3-fin FPRE heatsink antenna.....	110
5-53	Frequency-tracking comparison of simulated peak directivity vs. fin height for 3-fin FPNRE heatsink antenna	111
5-54	Frequency-tracking comparison of simulated peak directivity vs. fin height for 3-fin FPRE heatsink antenna	111
5-55	Frequency-tracking comparison of simulated peak gain vs. fin height for 3-fin FPNRE heatsink antenna	112
5-56	Frequency-tracking comparison of simulated peak gain vs. fin height for 3-fin FPRE heatsink antenna.....	112
5-57	E-field vector (top) and magnitude (bottom) plots of FPRE heatsink antenna at 8 mm and 10 mm fin heights given at the respective primary resonances	114
5-58	Simulated 3-D radiation patterns for fin height sweep of 3-finned extruded-fin heatsink antenna (FPNRE case) at both the primary and alternate resonances	115
5-59	Simulated 3-D radiation patterns for fin height sweep of 3-finned extruded-fin heatsink antenna (FPRE case) at both the primary and alternate resonances.....	115
5-60	Fin thickness sweep for radiation efficiency vs. fin height for 3-finned antennas with a heatsink base thickness = 1 mm at 5.80 GHz	117

5-61	Fin thickness sweep for peak directivity vs. fin height for 3-finned antennas with a heatsink base thickness = 1 mm at 5.80 GHz	117
5-62	Fin thickness sweep for peak gain vs. fin height for 3-finned antennas with a heatsink base thickness = 1 mm at 5.80 GHz.....	118
5-63	Simulated resonant frequencies of 2-finned and 3-finned antennas vs. fin height for fins parallel to the radiating edges (FPRE).....	119
5-64	Simulated primary resonant frequencies of 2-finned and 3-finned antennas vs. fin height for fins parallel to the non-radiating edges (FPNRE).....	119
5-65	Comparison of simulated return loss data for 2-finned vs. 3-finned heatsink antennas at a fin height of 2 mm with fins along the non-radiating edges (FPNRE)	120
5-66	Comparison of simulated return loss data for 2-finned vs. 3-finned heatsink antennas at a fin height of 6 mm with fins along the non-radiating edges (FPNRE)	120
5-67	Comparison of simulated return loss data for 2-finned vs. 3-finned heatsink antennas at a fin height of 12 mm with fins along the non-radiating edges (FPNRE)	121
5-68	Comparison of simulated return loss data for 2-finned vs. 3-finned heatsink antennas at a fin height of 16 mm with fins along the non-radiating edges (FPNRE)	121
5-69	Comparison of simulated return loss data for 2-finned vs. 3-finned heatsink antennas at a fin height of 20 mm with fins along the non-radiating edges (FPNRE)	121
5-70	Comparison of simulated return loss data for 2-finned vs. 3-finned heatsink antennas at a fin height of 2 mm with fins along the radiating edges (FPRE)	122
5-71	Comparison of simulated return loss data for 2-finned vs. 3-finned heatsink antennas at a fin height of 6 mm with fins along the radiating edges (FPRE)	122
5-72	Comparison of simulated return loss data for 2-finned vs. 3-finned heatsink antennas at a fin height of 12 mm with fins along the radiating edges (FPRE)	122
5-73	Comparison of simulated return loss data for 2-finned vs. 3-finned heatsink antennas at a fin height of 16 mm with fins along the radiating edges (FPRE)	123
5-74	Comparison of simulated return loss data for 2-finned vs. 3-finned heatsink antennas at a fin height of 20 mm with fins along the radiating edges (FPRE)	123
5-75	Comparison of radiation efficiency vs. fin height for 2-finned and 3-finned 5.8 GHz heatsink antennas	124
5-76	Comparison of peak directivity vs. fin height for 2-finned and 3-finned 5.8 GHz heatsink antennas	124

5-77	Comparison of peak gain vs. fin height for 2-finned and 3-finned 5.8 GHz heatsink antennas.....	125
5-78	Comparison number of fins on radiation efficiency vs. fin height with fins parallel to the non-radiating edges (FPNRE) at 5.80 GHz	126
5-79	Comparison number of fins on peak directivity vs. fin height with fins parallel to the non-radiating edges (FPNRE) at 5.80 GHz	127
5-80	Comparison number of fins on peak gain vs. fin height with fins parallel to the non-radiating edges (FPNRE) at 5.80 GHz.....	127
5-81	Comparison number of fins on radiation efficiency vs. fin height with fins parallel to the radiating edges (FPRE) at 5.80 GHz.....	128
5-82	Comparison number of fins on peak directivity vs. fin height with fins parallel to the radiating edges (FPRE) at 5.80 GHz.....	128
5-83	Comparison number of fins on peak gain vs. fin height with fins parallel to the radiating edges (FPRE) at 5.80 GHz.....	129
5-84	HFSS model of 36-fin (6x6) pin-fin heatsink antenna.....	130
5-85	Resonant frequencies of the pin-fin heatsink antenna compared with the 3-finned extruded heatsink antenna with fins parallel to the radiating edges (FPRE)	131
5-86	Comparison of pin-fin and extruded-fin heatsink antenna radiation efficiency vs. fin height.....	131
5-87	Comparison of pin-fin and extruded-fin heatsink antenna peak directivity vs. fin height.....	132
5-88	Comparison of pin-fin and extruded-fin heatsink antenna peak gain vs. fin height.....	132
5-89	Simulated 3-D radiation patterns vs. fin height for 6x6 pin-fin heatsink antenna.....	133
6-1	HFSS model of 5.8 GHz boxed heatsink antenna with 6 mm fins parallel to the non-radiating edges	138
6-2	HFSS model of 5.8 GHz boxed heatsink antenna with 6 mm fins parallel to the radiating edges	139
6-3	HFSS model of cubic heatsink antenna	139
6-4	Simulated return loss of boxed and 3-finned heatsink antennas with 9 mm fins parallel to the non-radiating edges (FPNRE).....	140
6-5	Simulated return loss of boxed and 3-finned heatsink antennas with 11 mm fins parallel to the radiating edges (FPRE).....	141

6-6	Resonant frequency of boxed and 3-finned heatsink antennas for the non-radiating edge case (FPNRE).....	142
6-7	Resonant frequency of boxed and 3-finned heatsink antennas for the radiating edge case (FPRE)	143
6-8	S_{11} of boxed heatsink for various fin heights (1 mm to 21.1 mm in 4 mm increments) along the non-radiating edges	144
6-9	S_{11} of boxed heatsink for various fin heights (1 mm to 21 mm in 4 mm increments) along the radiating edges	144
6-10	Radiation efficiency of boxed heatsink antennas compared to the 3-finned heatsink antennas at 5.80 GHz	146
6-11	Peak directivity of boxed heatsink antennas compared to the 3-finned heatsink antennas at 5.80 GHz	146
6-12	Peak gain of boxed heatsink antennas compared to the 3-finned heatsink antennas at 5.80 GHz.....	147
6-13	Three-dimensional gain patterns of boxed heatsink antenna versus fin height for both fin orientations (FPNRE and FPRE).....	147
6-14	Resonant frequencies of cubic heatsink antenna compared to the boxed heatsink antenna primary resonances.....	149
6-15	Radiation efficiency vs. fin height of cubic heatsink antenna compared with the boxed and 3-finned antennas	149
6-16	Peak directivity vs. fin height of cubic heatsink antenna compared with the boxed 3-finned antennas	150
6-17	Peak gain vs. fin height of cubic heatsink antenna compared with the boxed 3-finned antennas.....	150
7-1	Power amplifier schematic for 2.45 GHz operation [Dat].....	153
7-2	Layout of power amplifier circuit.....	154
7-3	Diagram showing top view (left) and side view (right) of electrical and thermal vias (note: not to scale, heatsink rotated 90 degrees for illustrative purposes).....	155
7-4	Backside of heatsink antenna/PA module showing circuit.....	156
7-5	Topside of heatsink antenna/PA module	157
7-6	Measured return loss of heatsink antenna.....	158

7-7	Measurement setup for the PA/HSA testing.....	159
7-8	Simulated temperature distribution in the heatsink, thermal via, and electrical via at an output power level of 27dBm.....	161
7-9	Simulated temperature distribution in the heatsink, thermal via, and electrical via at an output power level of 31dBm.....	162

Abstract of Dissertation Presented to the Graduate School
of the University of Florida in Partial Fulfillment of the
Requirements for the Degree of Doctor of Philosophy

DUAL-FUNCTION HEATSINK ANTENNAS FOR HIGH-DENSITY THREE-
DIMENSIONAL INTEGRATION OF HIGH-POWER TRANSMITTERS

By

Lance Nicholas Covert

May 2008

Chair: Jenshan Lin

Major: Electrical and Computer Engineering

Radiation from heatsinks is typically undesirable and should be minimized to reduce electromagnetic interference (EMI). However, in certain applications it can be advantageous to maximize the radiation from a heatsink by using the heatsink as the antenna. For example, high-power RF transmitters require both a heatsink and an antenna. The heatsink is needed to remove the excessive thermal energy generated by the power amplifier, and the antenna is needed to launch the electromagnetic waves. The heatsink antenna combines these two functions into one reducing the total component count in the transmitter and improving antenna performance.

Heatsink antennas were developed at 5.8 GHz and 2.4 GHz using a patch antenna as a mounting and feeding structure. These antennas demonstrated increased radiation efficiency, bandwidth and gain. Parametric studies were performed including fin height, fin thickness and fin orientation to determine the effects on the antenna performance. The orientation of the fins plays a significant role in the behavior of the antenna and must be considered. The radiation patterns can be changed significantly depending fin orientation. Other types of antennas were considered including a pin-fin heatsink antenna, two-finned heatsink antenna, a boxed three-fin heatsink antenna and a cubic antenna. Finally, a heatsink antenna was integrated with a commercial power amplifier to demonstrate the concept.

CHAPTER 1 INTRODUCTION

1.1 Introduction

In 1958 Jack Kilby of Texas Instruments realized that each electronic component could be fabricated in silicon reducing the size of the components and the overall circuit. Around the same time, Robert Noyce of Fairchild Semiconductor (a small startup company at the time) also realized that an entire circuit could be put on chip. The result of the work done by these two researchers was the integrated circuit (IC) [Rab].

Before the integrated circuit each component including resistors, capacitors, inductors and transistors was relatively large as were the interconnections between the components. With the advent of the IC, much higher integration was possible resulting in much smaller circuits. Where circuits of thousands of transistors were possible, current technologies allow billions of transistors to be placed on a single chip. This revolutionized the electronics industry and sent the room-sized computer packing into the laptop. However, digital computing was not the only application to flourish in direct consequence of the IC.

The wireless communications arena has also benefited from the integrated circuit and MMIC (monolithic microwave integrated circuit). Today, cellular phones and GPS devices not only have more computing power than the first supercomputers [Rab], but they contain RF and microwave circuitry as well. Clearly, the trend of electronics is in a direction of higher integration and complexity.

The ICs and MMICs common today are two-dimensional (2-D) circuits. Although these ICs have several metal layers, transistors are only fabricated on a single layer. Thus, the circuit is limited to the x- and y-dimensions only. If the z-dimension could be utilized to realize integrated circuits, then three-dimensional (3-D) ICs could lead to even higher chip densities and

may also provide better performance including less loss, less delay and lower power dissipation due to shorter interconnects and routing via the third dimension [Rah]. As a result of the promising advantages of 3-D integration, much research has been done in this area.

1.2 3-D System-on-Chip (SOC) with Integrated 3-D Heatsink Antenna

System-on-chip (SOC) technologies place each part of the system into a single-chip solution. This reduces the overall size and cost of the system. By combining the 3-D integration and SOC technology, three-dimensional (3-D) SOC may be possible.

A proposed 3-D structure with integrated heatsink antenna is shown in Figure 1-1 for illustration purposes. The 3-D SOC example utilizes different semiconductor layers separating the different functions of the chip. The power amplifier uses a GaN device on a silicon carbide (SiC) substrate. Since the heat generated in the GaN layer is significant, a thermal insulator is shown to protect the silicon devices that lie in the layer beneath. The SiC layer has a higher thermal conductivity than silicon and more efficiently conducts heat away from the chip to the antenna. Vias may be added in the SiC layer to help remove the heat by increasing the thermal conductivity of the package and also help shield the feed line to the antenna.

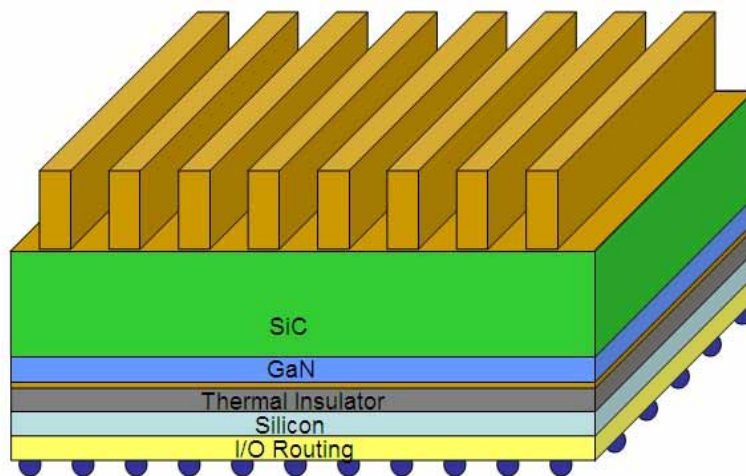


Figure 1-1. Illustration of 3-D SOC structure with integrated heatsink antenna

The heat dissipation can be highly destructive to the devices that generate it (such as the power amplifier in RF transceivers) and to the surrounding electronics (such as the low-noise receiver). Therefore, removal of this heat is requisite and a heatsink structure is required. However, the heatsink structure, which is usually also electrically conductive, can affect the nearby antenna's performance. To solve this electromagnetic compatibility issue, one solution is to use the heatsink structure itself as an antenna, or design the antenna structure as a good heatsink.

1.3 Heatsink Antenna

Heat dissipation in high-power amplifiers and high-speed microprocessors typically requires the use of a heatsink. As chip densities increase and advances in packaging technologies chaperon high-density 3-D SOCs (system-on-a-chip) into the market, the heatsink will be around for some time. In applications such as high-power RF transmitters, the heatsink can be used as an antenna to reduce the number of components and overall size/cost of the system. Until this research the only heatsink studies were focused on reducing electromagnetic emissions for electromagnetic compatibility [Geo, Dol, Das, Rya]. Previous heatsink emission research did not address antenna parameters such as radiation efficiency, bandwidth, directivity/gain, input impedance, etc. In order to design a good antenna it is necessary to understand how the antenna parameters are affected by the heatsink's physical properties and dimensions such as heatsink type, fin height, and fin orientation. As it turns out, paying attention to these parameters can mean the difference between a favorable antenna design and an unacceptable antenna design.

Two common types of heatsinks are the extruded-fin and pin-fin heatsinks (Figure 1-2). While the pin-fin heatsink antenna has only one orientation due to its symmetry, the extruded-fin heatsinks have two orthogonal orientations with respect to a patch antenna's radiating and non-

radiating edges. This orientation plays an important role in the antenna performance. The fin height also has a significant effect on the antenna performance.

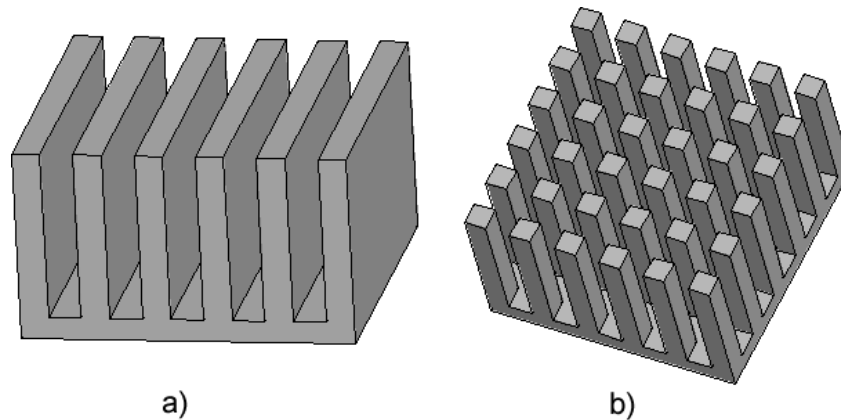


Figure 1-2. Common heatsink types: a) extruded-fin heatsink and b) pin-fin heatsink

The concept of heatsink antennas may also be applied to the possible integration of a wireless data links in high-speed microprocessors. The heatsink structure needed for the high speed microprocessor can be used as the antenna for a wireless data link, thus, solving the problem of limited space in high density integration and exploiting the heatsink to improve the antenna performance.

Furthermore, the heatsink antenna may be applied to parallel computer architecture or parallel computing (supercomputing). Supercomputers are built to achieve the highest performance possible since they are not bound and cost-restrained by the consumer market. Consequently, these systems commonly contain up to thousands of processors (each with a heatsink) and highly complex interconnection topologies (grid, torus, cube, binary trees, butterflies, benes, hypercubes, etc.). By using the heatsink as an antenna, a wireless network could be used to form the interconnection topology. Certainly, this would reduce the physical size of the overall system and eliminate the physical interconnect complexity (protocol and

communication complexities still exist) [Cul]. A study has already been published on creating a wireless hypercube interconnect topology for parallel computing and communication environment using Bluetooth technology [Cha].

Active phased array radars may benefit from the use of the heatsink antenna for military and space applications as well. These systems can contain thousands of high-power active RF radiating elements. Finally, the heatsink antenna may possibly be applied to wireless power transfer (WPT) applications. These systems need to high-power antennas with very high antenna gain to minimize free-space losses.

CHAPTER 2 BACKGROUND INFORMATION

2.1 Introduction

This chapter discusses the background information relating to the material presented in later chapters. Starting with a general discussion on RF transceivers (specifically, the transmitter) allows the reader to see the relationship between the power amplifier and the antenna from a system's perspective. Next, basic antenna parameters are presented including their importance in RF system design. Microstrip patch antenna design is discussed next since the heatsink antennas are based on this initial design. Next, thermal issues are discussed since the antenna must also be a good heatsink.

2.2 RF Transceivers and the Transmitter

An RF transceiver generally consists of a transmitter, receiver, one or more antennas and a duplexing device (or switch) if only one antenna is present. The transmitter and receiver can each have their own antenna or they can share a single antenna as shown in Figure 2-1. In this case, additional components must be included for arbitrating the use of or sharing the antenna. In half-duplex systems a simple transmit/receive (T/R) switch can be used since transmitting and receiving do not occur simultaneously. In full-duplex systems, however, a T/R switch cannot be used. In this case, a duplexer must be used which provides isolation between the transmit and receive ports [Poz1].

The RF transmitter operates on the baseband (low-frequency) data in a manner that makes it suitable for transmission across a wireless channel. It contains some form of modulator, up-converter(s), power amplifier, various filters, and the transmit antenna (this antenna may be separate or shared with the RF receiver). The modulator transforms the data (1s and 0s in a digital system) into waveforms suitable to pass through the channel and recognizable by the

receiver. For example, the amplitude, frequency and phase of the signal contain information and one of these parameters or a combination of these parameters can be modulated by the data. The up-converter (or up-conversion mixer) converts the low-frequency signal to a higher frequency which is more suitable for transmission across the wireless channel. Depending on the type of transmitter architecture, e.g. direct-conversion or indirect-conversion (superheterodyne), etc., one or more up-converting mixers and filters may be used. Various filters are used to block out the signal power at frequencies outside of a specific spectrum. The filtering eliminates unwanted mixer products and other harmonics due to nonlinearities in the active devices. The up-converted, modulated signal is passed through a bandpass filter to clean up the spectrum. Finally, the output of the filter is then passed to a power amplifier.

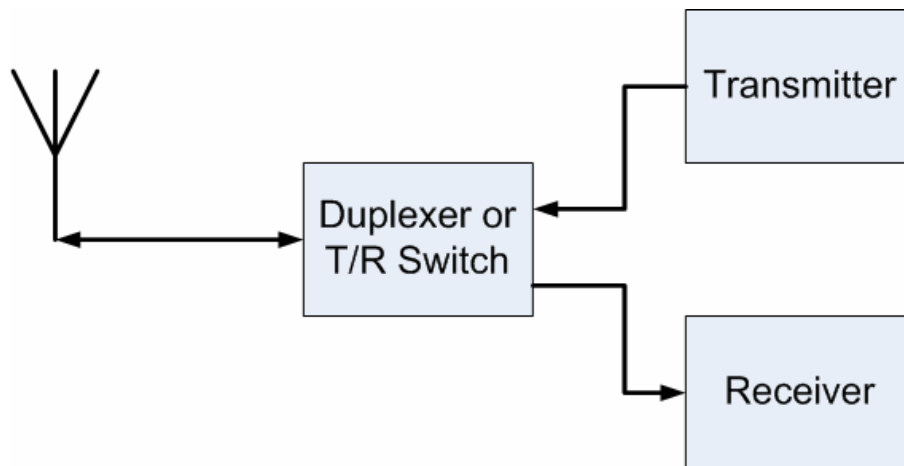


Figure 2-1. RF transceiver block diagram

The power amplifier provides the signal with enough power to propagate over a required distance or through certain mediums in order to exhibit a proper signal-to-noise ratio to the receiver at a certain location. More specifically, the power amplifier takes the modulated high-frequency signal and amplifies the signal such that it may overcome attenuation due to

propagation over long distances or propagation through high-loss mediums. After the power amplifier the signal is often passed through a bandpass filter to limit its spectral content reduce interference and to meet specifications. Next, the signal is passed to an antenna which transforms the signal from an electrical signal to an electromagnetic signal which can easily propagate through the channel.

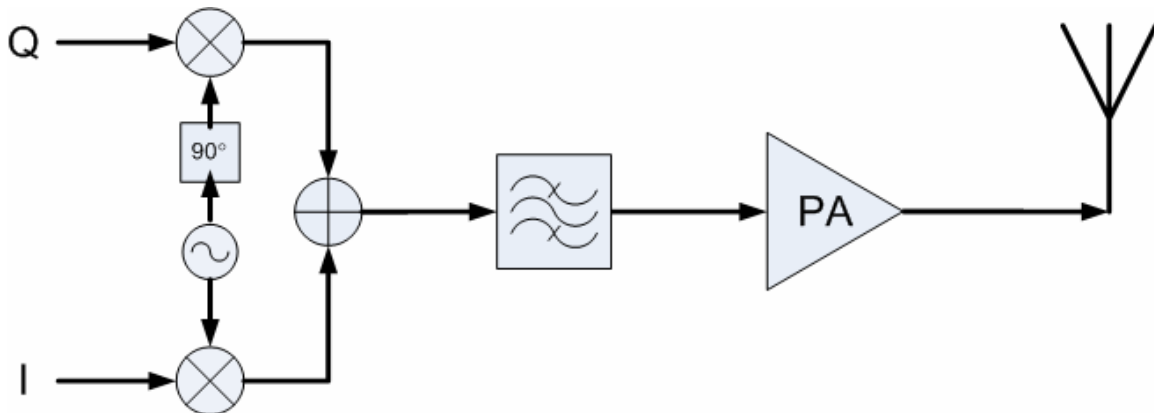


Figure 2-2. Direct-conversion transmitter block diagram

Figure 2-2 shows the simplified block diagram of a direct-conversion transmitter. The transmitter is shown with its own antenna connected directly to the power amplifier. This close proximity of the power amplifier and the antenna in the transmitter chain facilitates the use of the power amplifier's heatsink as the antenna. By combining the functions of the heatsink and the antenna into one structure, the component count in the transmitter, the size, mass and cost can be reduced. Also, the heatsink can give improved antenna performance over alternatives such as patch antennas and flexibility in design. For example, the radiation pattern can be changed significantly depending on the orientation of the heatsink fins and the fin height.

2.3 Antenna-Related Parameters

The research presented introduces a heatsink antenna, and thus, a general discussion on antennas and antenna parameters is needed. The input impedance of antennas and its importance

on reflected power is discussed. Antenna parameters including radiation efficiency, directivity and gain are briefly introduced next. Finally, the Friis equation is introduced to tie the antenna parameters together in relation to an RF system.

2.3.1 Input Impedance and Reflected Power

The input impedance of an antenna is defined as the ratio of voltage to current at the antenna's terminals. Generally, the input impedance consists of both real and imaginary parts.

This is demonstrated by Eq. 2-1:

$$Z_A = R_A + jX_A \quad (2-1)$$

The real part R_A can be broken down into two separate resistances:

$$R_A = R_L + R_r \quad (2-2)$$

where R_r represents the radiation resistance and R_L is the loss resistance. This is shown graphically in Figure 2-3.

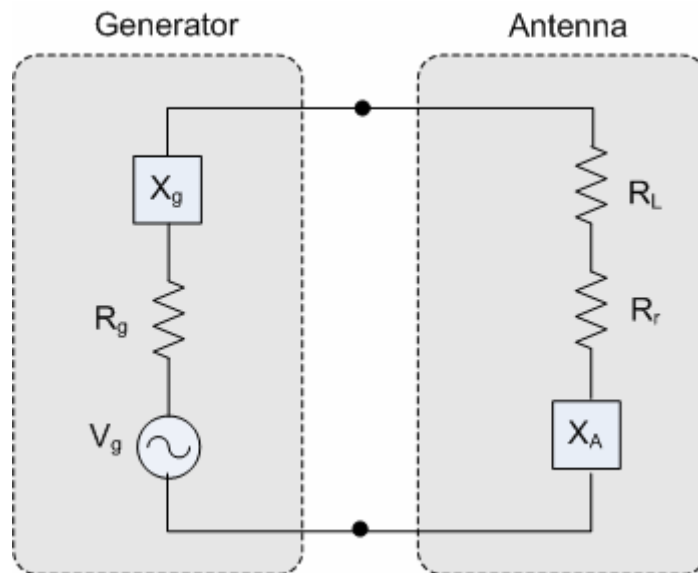


Figure 2-3. Thevenin equivalent circuit of antenna

The generator (or source) has an impedance can be generalized in the form

$$Z_G = R_G + jX_G \quad (2-3)$$

The power supplied by the generator is

$$P_s = \frac{1}{2} \Re(V_G I_G^*) = \frac{1}{2} V_G \Re\left(\frac{V_G^*}{Z_G + Z_A}\right) = \frac{1}{2} |V_G|^2 \left(\frac{1}{R_G + R_L + R_r}\right) \quad (2-4)$$

where V_G is the peak voltage of the generator. Maximum power transfer occurs under conjugate matching where $Z_G = Z_A^*$ or

$$R_G = R_A = R_L + R_r \quad (2-5)$$

$$X_G = -X_A \quad (2-6)$$

In this case, the power supplied by the generator reduces to

$$P_s = \frac{1}{2} |V_G|^2 \left(\frac{1}{R_G + R_L + R_r}\right) = \frac{1}{4} |V_G|^2 \left(\frac{1}{R_L + R_r}\right) \quad (2-7)$$

The power delivered to the radiation resistance, R_r , is given by

$$P_r = \frac{1}{2} |V_G|^2 \left(\frac{R_r}{4(R_L + R_r)^2}\right) = \frac{1}{8} |V_G|^2 \left(\frac{R_r}{(R_L + R_r)^2}\right) \quad (2-8)$$

Similarly, the power delivered to the loss resistance, R_L , is

$$P_L = \frac{1}{2} |V_G|^2 \left(\frac{R_L}{4(R_L + R_r)^2}\right) = \frac{1}{8} |V_G|^2 \left(\frac{R_L}{(R_L + R_r)^2}\right) \quad (2-9)$$

The power dissipated in the internal resistance of the generator, R_G , is given by

$$P_G = \frac{1}{2} |V_G|^2 \left(\frac{R_G}{(R_r + R_L + R_G)^2}\right) = \frac{1}{2} |V_G|^2 \left(\frac{R_r + R_L}{(2(R_r + R_L))^2}\right) = \frac{1}{8} |V_G|^2 \left(\frac{1}{(R_r + R_L)}\right) \quad (2-10)$$

By adding Eqs. 2-8 and 2-9 is can be shown that

$$P_G = P_L + P_r \quad (2-11)$$

From first principles, under conjugate matching half of the power supplied by the source should be dissipated in the internal resistance of the generator while the other half should be delivered to the load. This is clearly the case as the power dissipated in the generator given by

Eq. 2-10 is half of the power supplied by the source in Eq. 2-7; and from Eq. 2-11, the power delivered to the load is equal to the power dissipated in the generator obeying the conservation of energy [Bal].

It is useful to discuss the power relationships in reference to the reflection coefficient. Figure 2-4 shows a source connected to the load (an antenna) via a length of lossless transmission line. The reflection coefficient between the load and the transmission line is given by

$$\Gamma_L = \frac{Z_A - Z_0}{Z_A + Z_0} \quad (2-12)$$

where Z_0 is the characteristic impedance of the transmission line and Z_A represents the input impedance of the antenna. The reflection coefficient is a complex number, however, squaring the magnitude results in the percentage of incident power which is reflected by the load due to the mismatch. Assuming the source is properly impedance-matched to the transmission line ($Z_g = Z_0$) such that multiple reflections do not occur, the accepted power into the antenna can be expressed as

$$P_{acc} = P_{inc} (1 - |\Gamma_L|^2) = P_{inc} - P_{refl} \quad (2-13)$$

where P_{inc} is the power incident at the antenna's port and P_{refl} is the reflected power due to the impedance mismatch [Poz1]. For a one-port network, the reflection coefficient (Γ_L) is equal to the scattering parameter S_{11} which is easily measured on a network analyzer. This facilitates a simple method to observe the delivery of power into the antenna.

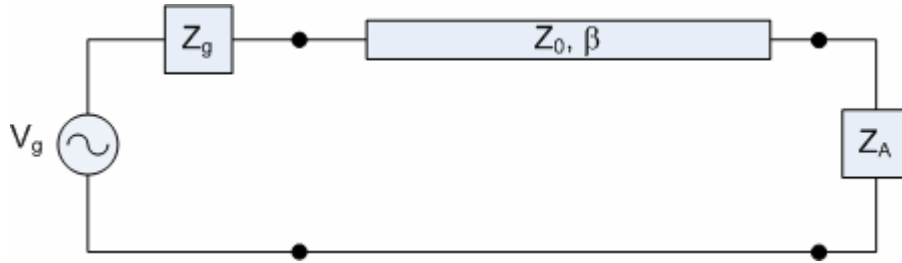


Figure 2-4. Antenna connected to source via a transmission line

2.3.2 Radiation Efficiency

Section 2.3.2 discussed the amount of power accepted into the antenna which was shown to depend on the matching conditions. Unfortunately, the loss of power does not end there. Next, the accepted power into the antenna is subject to other losses in the antenna. The radiation efficiency is defined as the ratio of the radiated power to the accepted power:

$$e_{rad} = \frac{P_{rad}}{P_{acc}} = \frac{P_{acc} - P_{loss}}{P_{acc}} \quad (2-14)$$

where P_{rad} is the radiated power and P_{acc} is the accepted power from Eq. 2-13. Eq. 2-14 is expressed in relation to a transmitting antenna, but since antennas are bidirectional the same principle applies in receiving mode [Poz1].

2.3.3 Directivity

Since an antenna radiates energy into a three-dimensional space, it is useful to describe the antenna's ability to focus the radiation. Directivity is defined as the ratio of the radiation intensity in a given direction to the average radiation intensity over all space:

$$D = \frac{U(\theta, \phi)}{U_{avg}} = \frac{4\pi U(\theta, \phi)}{P_{rad}} = \frac{4\pi U(\theta, \phi)}{\int_{\theta=0}^{\pi} \int_{\phi=0}^{2\pi} U(\theta, \phi) \sin(\theta) d\theta d\phi} \quad (2-15)$$

where $U(\theta, \phi)$ is the radiation intensity in a given direction, U_{avg} is the radiation intensity averaged over all directions, P_{rad} is the total power radiated by the antenna. Peak directivity is

defined as the ratio of the maximum radiation intensity to the average radiation intensity over all space. Therefore, by changing U to U_{max} the peak directivity (D_{peak}) is obtained [Poz1, Bal]:

$$D_{peak} = \frac{U_{max}}{U_{avg}} = \frac{4\pi U_{max}}{P_{rad}} = \frac{4\pi U_{max}}{\int_{\theta=0}^{\pi} \int_{\phi=0}^{2\pi} U(\theta, \phi) \sin(\theta) d\theta d\phi} \quad (2-16)$$

From this point forward, any discussion on directivity will refer to peak directivity as defined by Eq. 2-16. Typically, directivity is specified in decibels by taking $10\log_{10}(D)$.

An *isotropic* antenna is an antenna which radiates equally in all directions, i.e., the radiation pattern is a perfect sphere; however, this type of antenna exists only in theory. Since an isotropic antenna has equal radiation intensity in all directions, the average radiation intensity (U_{avg}) is equal to the radiation intensity in any given direction ($U(\theta, \phi)$); therefore, from Eq. 2-15, the directivity of an isotropic antenna is 1 in dimensionless terms or 0 dB. Often the directivity of an antenna is reported as dBi which implies directivity relative to an isotropic radiator.

2.3.4 Gain

While directivity describes the focusing ability of an antenna, it says nothing about the radiation efficiency. Antenna gain takes into account the losses in the antenna in combination with the directivity which results in a more useful antenna parameter in relation to RF systems.

Eq. 2-17 relates antenna gain to the directivity:

$$G = e_{rad} D \quad (2-17)$$

where G and D are dimensionless quantities. Note: when D_{peak} is used in Eq. 2-17 the peak gain (G_{peak}) is obtained.

Gain is a term which often induces confusion in context with a passive element such as an antenna. The term, however, is used to describe power gain relative to an isotropic antenna.

In this manner, the conservation of energy is not violated. For example, consider two antennas radiating an equal amount of power, however, one antenna is isotropic and the other antenna has the ability to focus its power (non-isotropic). A receiving antenna located in a direction in the maximum radiation intensity of the non-isotropic antenna will receive more power than the receiving antenna of the isotropic radiator. Stated alternately, an antenna with a gain transmits an amount of power which can be related to an *effective isotropic radiated power (EIRP)*:

$$EIRP = P_t G_t \quad (2-18)$$

where P_t is the transmitted power and G_t is the gain of the transmitting antenna as a dimensionless quantity [Poz1].

2.3.5 Friis Transmission Equation

The Friis transmission equation (or Friis equation) takes the parameters discussed previously and relates them to the RF system link. It is fundamental in RF communication system design. The Friis equation is written as

$$P_r = \frac{G_t G_r \lambda^2}{(4\pi R)^2} P_t \quad (2-18)$$

where P_r is the received power, P_t is the transmitted power, R is the range (distance) and λ is the wavelength. G_t and G_r are the peak gains of the transmit and receive antennas, respectively, as discussed in section 2.3.5. The received power in Eq. 2-18 is an absolute maximum due to other effects that cause power loss. The Friis equation can be modified to include these losses. First, by revisiting the impedance matching issue discussed in section 2.3.2, Eq. 2-13 is rearranged

$$\frac{P_{acc}}{P_{inc}} = (1 - |\Gamma_L|^2) \quad (2-19)$$

which results in the ratio of accepted power to incident power. This expression is for a single antenna only (transmit or receive). Since a system contains both transmit and receive antennas, by taking into account the impedance mismatches for both antennas Eq. 2-20 results

$$e_{imp} = (1 - |\Gamma_t|^2)(1 - |\Gamma_r|^2) \quad (2-20)$$

where Γ_t is the reflection coefficient for the transmit antenna and Γ_r is the reflection coefficient for the receive antenna.

Another important loss factor is the polarization loss factor which is a measure of the relative orientations of the two antennas with respect to each other. In order for optimized transmission between two antennas, they must be polarized in the same manner and direction. For example, a horizontally polarized transmitting antenna should be combined with a horizontally polarized receiving antenna in order to receive the maximum amount of power. Similarly, a right-hand circularly polarized transmitting antenna should be combined with a right-hand circularly polarized receiving antenna to minimize polarization mismatch losses. Quantitatively, this is defined as

$$e_{pol} = |\hat{e}_i \cdot \hat{e}_r|^2 \quad (2-21)$$

where \hat{e}_i is the unit vector denoting the polarization of the electric field of the incident plane wave, and \hat{e}_r is the unit vector denoting the polarization of the electric field of the receive antenna (when the receive antenna is acting as a transmitting antenna).

These losses due to impedance and polarization mismatch can be taken into account in the Friis equation by combining Eqs. 2-18, 2-20, and 2-21:

$$P_r = \frac{G_t G_r \lambda^2}{(4\pi R)^2} P_t e_{imp} e_{pol} \quad (2-22)$$

Other losses occur due to multipath effects and attenuation due to the atmosphere (such resonances with molecular oxygen and molecular water) [Poz1].

2.4 Microstrip Patch Antennas

Using the transmission line model, square microstrip patch antenna design starts with the assumption that the length of the patch should be approximately a half-wavelength at the frequency of operation. The wavelength can easily be determined from the well-known relationship:

$$\lambda = \frac{c}{f} \quad (2-23)$$

where c is the free-space speed of light, f is the frequency of the wave and λ is the wavelength.

However, this assumes the electromagnetic wave is in free space (or a vacuum). The effect of the medium on the propagation velocity of the wave should be determined. The phase velocity is written as

$$v_p = \frac{1}{\sqrt{\epsilon_r \epsilon_0 \mu_r \mu_0}} = \frac{c}{\sqrt{\epsilon_r \mu_r}} \quad (2-24)$$

where ϵ_r and μ_r are the relative permittivity and relative permeability of the medium, respectively, and ϵ_0 and μ_0 are the absolute permittivity and absolute permeability of the medium, respectively. Thus, by taking into the phase velocity and assuming the relative permeability of the medium is 1, the half-wavelength (or width of the patch) can be determined by

$$\frac{\lambda}{2} = \frac{v_p}{2f} = \frac{c}{2f\sqrt{\epsilon_r}} \quad (2-25)$$

where c in Eq. 2-23 was replaced with the phase velocity, v_p , of Eq. 2-24. Initially, the width of the patch, W , should be assumed to be a half-wavelength using Eq. 2-25 repeated below as

$$W = \frac{c}{2f\sqrt{\epsilon_r}} \quad (2-26)$$

Next, the length of the patch, L , is calculated using

$$L = \frac{c}{2f\sqrt{\epsilon_{eff}}} - 2\Delta \quad (2-27)$$

where Δ represents the extension of the magnetic wall due to fringing fields. ϵ_{eff} is the effective relative permittivity due to fringing fields and is approximated by

$$\epsilon_{eff} = \frac{\epsilon_r + 1}{2} + \frac{\epsilon_r - 1}{2} \left(1 + \frac{10H}{W} \right)^{-1/2} \quad (2-28)$$

where H in represents the height of the dielectric (or substrate thickness). Δ is calculated from the following expression

$$\Delta = 0.412H \left(\frac{\epsilon_{eff} + 0.300}{\epsilon_{eff} - 0.258} \right) \left(\frac{(W/H) + 0.262}{(W/H) + 0.813} \right) \quad (2-29)$$

By setting $W = L$ where L is given by Eq. 2-27 and performing another iteration of the calculation using Eq. 2-27 through Eq. 2-29 a close approximation for the dimensions of a square patch antenna will be obtained [Mil]. The antenna can be subsequently tuned in an electromagnetic simulation package such as Ansoft Designer for the desired frequency of operation.

2.5 Thermal Issues

Power amplifiers and discrete power transistors generally dissipate considerable amounts of thermal energy in addition to their output power in electrical energy. Similarly, microprocessors with thousands or millions of transistors also generate significant amounts of heat. This thermal dissipation increases the internal device temperature or junction temperature of the devices above the ambient temperature. If the internal temperature becomes too high,

destruction of the devices will occur. Thus, special considerations must be taken in order to alleviate this thermal issue. Generally, this is solved by attaching a heatsink. The heat is removed via conduction from the device to the heatsink and then removed from the heatsink via convection to the air or surrounding medium.

To illustrate the thermal issue quantitatively, a thermal analogy of Ohm's law is used.

The temperature difference across a device is defined as

$$T_2 - T_1 = P\theta \quad (2-30)$$

where θ is the *thermal resistance* in $^{\circ}\text{C}/\text{W}$ and P is the heat flow or thermal power dissipated in the device. The temperature difference, $T_2 - T_1$, in thermal analogy of Ohm's law is representative of a voltage difference. Similarly, the heat flow or thermal power dissipation is representative of current flow. Finally, the thermal resistance is aptly named and akin to resistance in an electrical circuit.

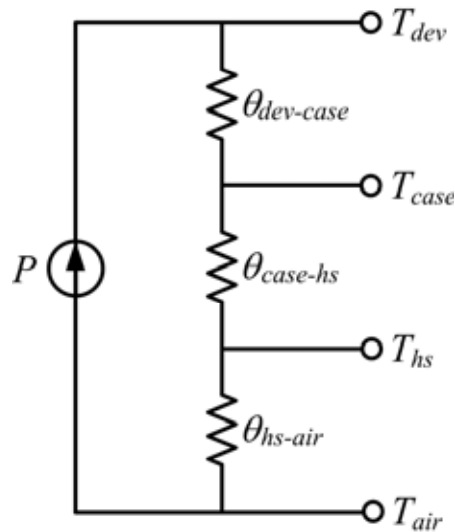


Figure 2-5. Electrical equivalent circuit of heat flow from the device to the air

The heat moves from one point to another through several materials (such as the device, case, heatsink, air); thus, the total thermal resistance can be divided into series resistances as in

an electrical circuit. This is shown in Figure 2-5. In Figure 2-5, $\theta_{dev-case}$ is the thermal resistance between the device and the case, $\theta_{case-hs}$ is the thermal resistance between the case and the heatsink, and θ_{hs-air} is the thermal resistance between the heatsink and the air or medium surrounding the heatsink. By modifying Eq. 2-30 with the new thermal resistances, the following expression can be written when the device has a case and a heatsink attached to the case

$$T_{dev} - T_{air} = P(\theta_{dev-case} + \theta_{case-hs} + \theta_{hs-air}) \quad (2-31)$$

where T_{dev} is the temperature of the device and T_{air} is the temperature of the air or the medium surrounding the heatsink. Assuming that the ambient temperature or temperature of the air will remain relatively constant, Eq. 2-31 shows that the device temperature decreases as the total thermal resistance decreases. Figure 2-5 shows the electrical equivalent circuit of the heat flow from the device to the air.

When no heatsink is used the thermal resistance terms dealing with the heatsink ($\theta_{case-hs}$ and θ_{hs-air}) must be removed from Eq. 2-31. At first glance, it may seem that since removing the heatsink requires removing the two thermal resistance terms that the device temperature would decrease for a constant dissipated power. However, a new term must be added to take into account the thermal resistance between the case and the air or surrounding medium ($\theta_{case-air}$) since no heatsink is used. This new thermal resistance will be much greater than the sum of the two heatsink-related thermal resistance terms since the case does not perform convection as efficiently as the heatsink; and therefore, the device temperature will be much higher. This is demonstrated by the following:

$$T_{dev} - T_{air} = P(\theta_{dev-case} + \theta_{case-air}) \quad (2-32)$$

where $\theta_{case-air} \gg (\theta_{case-hs} + \theta_{hs-air})$.

The maximum allowed power dissipation can be determined from the maximum device temperature, T_{max_dev} . By substituting the maximum device temperature for T_{dev} and solving for P , the maximum power dissipation, P_{max} , is obtained. For example, the maximum power dissipation in the case with the heatsink is [Nea, Geo]

$$P_{\max} = \frac{T_{dev_max} - T_{air}}{(\theta_{dev-case} + \theta_{case-hs} + \theta_{hs-air})}. \quad (2-33)$$

CHAPTER 3 PIN-FIN HEATSINK ANTENNA AT 2.4 GHZ

3.1 Introduction

Chapter 1 introduced the idea of the heatsink antenna: a dual-function structure which simultaneously radiates thermal and electromagnetic energy. The motivation for such an antenna is 3-D RF system integration since heat dissipation is of primary concern. High-density integrated circuits require heatsinks to remove the excessive amounts of generated heat. In an RF transceiver the power amplifier generates a significant amount of heat. The antenna is usually close in proximity to the power amplifier to minimize losses, and the heatsink must also be close to the power amplifier to be effective thermally. The heatsink (typically aluminum or copper) can have significant effects on the antenna. By combining the two into one structure, the effects of the heatsink can be exploited to enhance the antenna performance and provide higher integration by removing an extra component in the system (reducing cost, size, and mass).

A pin-fin type heatsink was used to design a 2.4 GHz heatsink antenna. Patch antennas were used in this study to evaluate the effects of the heatsink structure on the antenna properties. By adding a 3-D heatsink structure over a planar antenna, the performance of the antenna will change. This chapter introduces the heatsink antenna and compares its performance to a corresponding planar antenna. More specifically, a 2.4 GHz pin-fin heatsink antenna [Sha] was designed, simulated and fabricated to evaluate the effects of the heatsink on the antenna properties and to validate the use of such a structure as an antenna. Simulations were performed using Ansoft HFSS (High Frequency Structure Simulator). The antenna parameters are compared for a 2.4 GHz heatsink antenna including radiation efficiency, bandwidth, resonant frequency, and radiation patterns given by simulation and measurement.

3.2 Design Overview

3.2.1 Microstrip Patch Antenna Design and Simulation

Square microstrip patch antennas were used since the base of the heatsink over a substrate forms a patch antenna. By using a patch antenna platform, a heatsink attachment and alignment surface is available. This simplifies the fabrication process and allows the heatsink to be fed easily. The patch antennas were designed using the basic patch antenna equations described in [Mil, Cov] on low-cost FR4 substrates. The parameters needed for the antenna design using these equations are the desired frequency of operation (f), the substrate height (H), and the dielectric constant (ϵ_r). The equations produce the antenna dimensions (width and length). Since square patch antennas were used, the width (W) is equal to the length (L) in all cases.

The antennas are all edge-fed and thus appropriate feed lines were designed. Ansoft Designer was then used to fine-tune the planar design in simulation. This procedure was sufficient to achieve the desired operating frequency and matching for the planar antennas. Ansoft HFSS was used to simulate the antennas in a 3-D format. This allowed the modeling and simulation of the heatsink structures and finite ground plane effect.

The FR4 substrates used in this study have a thickness (H) of 1.6 mm and a dielectric constant of approximately 4.2. Using the procedures discussed above the basic patch antennas and the 2.4 GHz heatsink antennas were designed. Figure 3-1 shows the planar layout for the basic patch antennas. The layout includes a square patch, quarter-wave transformer (section 1) and a 50- Ω line (section 2) in an edge-fed design. An inset-fed design cannot be used for this type of antenna, since the heatsink base would effectively remove the inset. The tuning stub (section 3) is used only with the heatsink antennas for matching.

The 2.4 GHz antenna has a patch size of 29.1 mm x 29.1 mm. The 2.4 GHz antenna quarter-wave transformer has a width of 0.8 mm and a length of 18.2 mm. The 50-Ω line of the 2.4 GHz antenna has a width of 3.05 mm and a length of 15.2 mm.

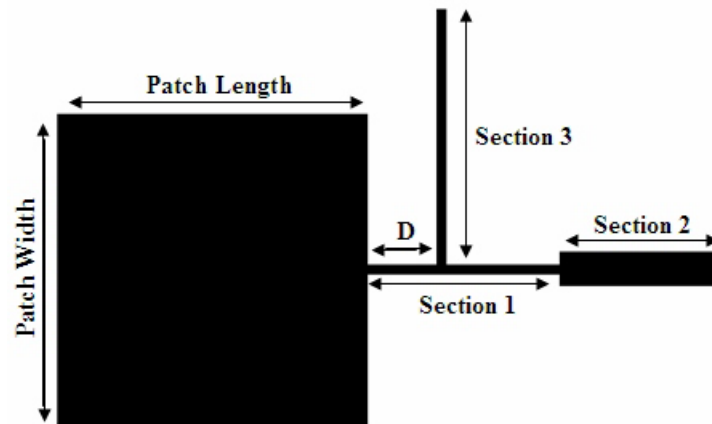


Figure 3-1. Planar dimensions of the patch antennas

3.2.2 Fabricated Patch and Heatsink Antenna

After performing simulations in Ansoft Designer, the patch antennas were fabricated on low-cost FR4 substrates which were presensitized with photoresist. This allows for simple pattern application via photolithography and subsequent copper etching with ferric chloride. Figure 3-2 shows the fabricated 2.4 GHz patch antenna. Also shown in the figure is the edge-mounted, standard polarity SMA connector.

Figure 3-3 shows the fabricated heatsink antenna designed to operate at 2.4 GHz. The heatsink was cut from a larger heatsink in order to match the dimensions of the square patch. The 2.4 GHz heatsink antenna has a pin-fin heatsink structure with 30 irregularly shaped vertical fins each having a height of 21.5 mm. The fin height does not including the heatsink base which has a thickness of approximately 3.5 mm.

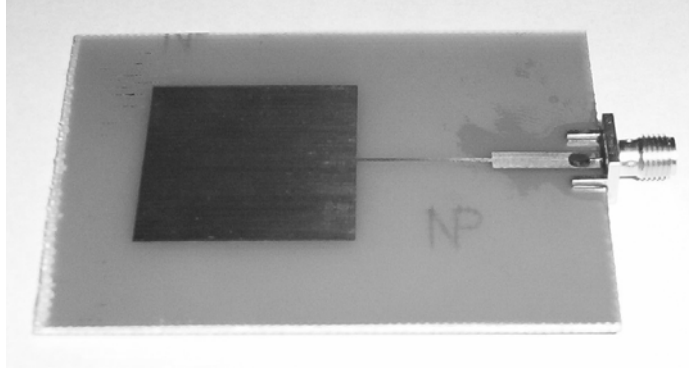


Figure 3-2. FR4 square patch antenna designed at 2.4 GHz

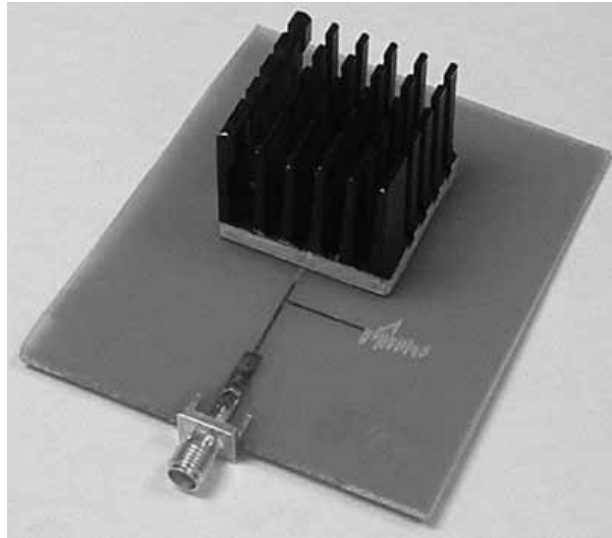


Figure 3-3. Fabricated 2.4 GHz FR4 heatsink antenna

The heatsink was attached to the copper patch with silver, conductive epoxy (Duralco 126) produced by Cotronics Corporation. The epoxy is a one-part paste and was cured for approximately 30 minutes at 275°F.

For the heatsink antenna, the length of the tuning stub is 14.0 mm with a separation (D in Figure 3-1) of 6.6 mm from the load. The width of the shunt transmission line in the heatsink antennas is equal to the width of the corresponding quarter-wave transformer.

3.2.3 HFSS Model Description

Ansoft HFSS was used for its 3-D modeling capabilities to simulate the heatsink antennas and the basic patch antennas with a finite ground plane. Figure 3-4 shows the 3-D HFSS model of the 2.4 GHz heatsink antenna. The HFSS model of the basic patch antenna is not shown here for conciseness, but differs only by the lack of the heatsink structure and tuning stub.

The heatsink dimensions and shape were estimated and simplified in the HFSS 3-D modeling. This was due to the complex structure of each heatsink. For instance, each fin of the 2.4 GHz heatsink was modeled by a rectangular structure while the actual heatsink fins have asymmetries, are rounded off, and have an undulating surface to increase surface area.

Aluminum was used as the heatsink material in the HFSS models.

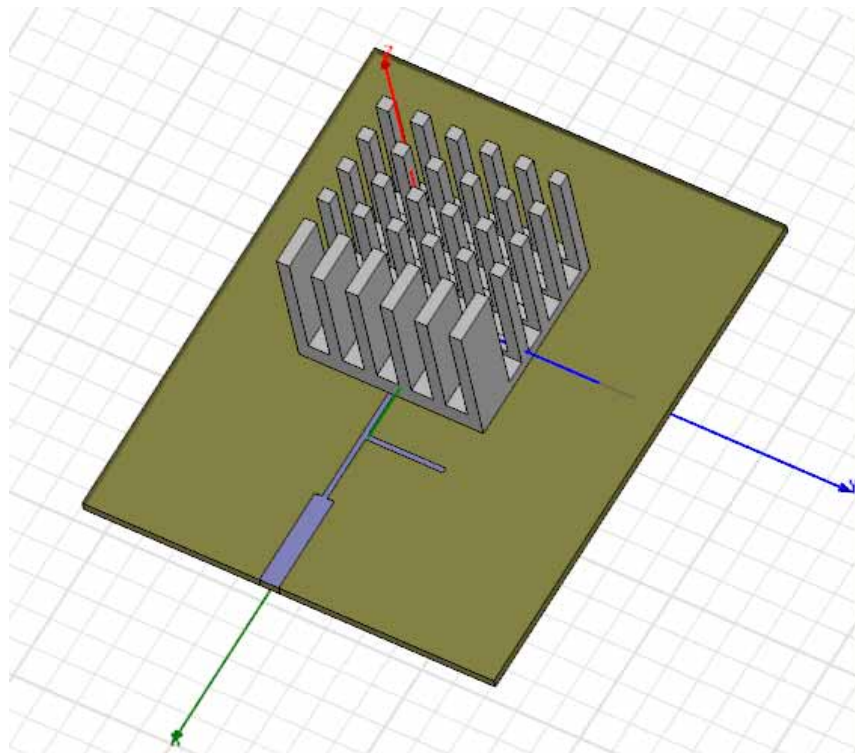


Figure 3-4. HFSS model of 2.4 GHz FR4 heatsink antenna

The ground plane and metal traces were modeled as 2-D surfaces to reduce simulation time, and a finite conductivity (copper) boundary was applied to these layers. The SMA edge-connectors were not modeled.

3.3 Results and Measurements

3.3.1 Radiation Efficiency

As discussed in Chapter 2, radiation efficiency is the ratio of the radiated power to the accepted power. More specifically, the power accepted into the antenna is accounted for in several ways: power dissipated in the dielectric (P_{diel}), power dissipated in the conductor (P_c), power in the surface waves (P_{surf}), and finally, the radiated power (P_{rad}) [Gar2]. This relationship is shown in Eq. 3-1 where R_{rad} is the equivalent radiation resistance and R_{loss} is the equivalent loss resistance. The definition does not take into account mismatch losses.

$$e_{rad} = \frac{P_{rad}}{P_{in}} = \frac{P_{rad}}{P_{rad} + P_c + P_{surf} + P_{diel}} = \frac{R_{rad}}{R_{rad} + R_{loss}} \quad (3-1)$$

where P_{in} is the power accepted into the antenna.

High loss tangents generally result in significant dielectric losses in microstrip applications [Gar1]. In high index materials loss due to the excitation of surface waves can also be a significant contributor [Pap]. All of the loss mechanisms stated above can occur in the feed line as well [Poz2]. Previous studies show that the radiation efficiency can be improved by applying special techniques such as making a cavity, synthesizing a substrate, creating trenches along the radiating edges or by elevating the radiating edges of the patch [Kim2].

Table 3-1. Comparison of antenna parameters (simulated)

Parameter	2.4 GHz patch antenna	2.4 GHz heatsink antenna
e_{rad} (total)	0.33	0.79
$e_{sw} e_{Joule}$ (lossless dielectric)	0.98	0.99
Peak directivity (dBi)	7.28	5.84
Peak gain (dBi)	2.46	4.83
Peak realized gain (dB)	2.46	4.61
Accepted power (Watts)	0.999	0.951
Radiated power (Watts)	0.330	0.751
1 st resonant freq. (GHz)	2.43	2.42
$ S_{11} $ @ 1 st res. freq.	-41.5	-13.1

HFSS simulation results for several antenna parameters are presented in Table 3-1, which compares the two antennas (basic patch and heatsink antenna with tuning stub). Note: the incident power is 1 Watt for both cases shown in Table 3-1. Though FR4 offers a low-cost option for patch antenna fabrication, its high dielectric loss tangent ($\tan(\delta) = 0.02$) significantly reduces the radiation efficiency due to high dielectric losses [Gar1]. Losses due to power dissipation in the conductor and excitation of surface waves are negligible since efficiencies of nearly 100% were obtained using copper conductors and lossless dielectrics in simulation. These efficiencies are reported as $e_{sw} e_{Joule}$ in Table 3-1.

In contrast, the dielectric losses significantly degrade the radiation efficiency in all four antennas using copper conductors and lossy (FR4) dielectrics in simulation and therefore, dominate the loss mechanisms. This efficiency is reported as e_{rad} (total) in Table 3-1. These efficiencies are repeated in Table 3-2 for measurement and simulation comparison.

The Wheeler Cap Method can be used to measure the peak radiation efficiency at resonance [Rog] and is reported as being the simplest and most accurate method for electrically small antennas [Mck]. The Wheeler Cap Method assumes the antenna can be modeled as a series or parallel RLC circuit. A metallic hemisphere is used to short out the radiation resistance

(R_{rad}) at resonance. Therefore, by measuring the free space (R_1) and Wheeler Cap (R_2) input resistance at resonance, the radiation efficiency can be determined from Eq. 3-2 for constant resistance case and from Eq. 3-3 for the constant conductance case [Mck].

$$e_{rad} = \frac{R_1 - R_2}{R_1} \quad (3-2)$$

$$e_{rad} = 1 - \frac{R_1}{R_2} \quad (3-3)$$

In this study, the modified Wheeler Cap Method was used to measure the radiation efficiency of the antennas. The modified method rotates the S_{11} data until the trace is tangent to either a constant resistance or constant conductance circle on the Smith chart so that it may be accurately modeled by either a series RLC or parallel RLC circuit [Mck]. A Wheeler cap testing apparatus very similar to that described in [Poz2] was built for the Wheeler cap measurement. A sheet metal ground plane was used underneath a metal hemispherical cap with a diameter of approximately 35 cm.

Table 3-2 lists the measured radiation efficiencies obtained from the modified Wheeler Cap Method. Each measurement was taken by shifting the data tangent to a constant conductance circle in order to be modeled by a parallel RLC circuit. The simulated radiation efficiencies of each antenna are also shown in Table 3-2. Both simulations and measurements show that the heatsink structure increases the radiation efficiency in each case. The 2.4 GHz antenna experienced a significant increase in radiation efficiency from 34% to 69% in measurements.

Table 3-2: Comparison of radiation efficiencies

Radiation efficiency	2.4 GHz patch antenna	2.4 GHz heatsink antenna
Simulated (%)	33	79
Measured (%)	34	69

This increase in radiation efficiency is due to fringing fields at the heatsink-air boundaries. This creates an effective dielectric constant more dominated by the surrounding medium (air) instead of the lossy substrate and the fields are less confined inside the substrate, reducing dielectric losses. The basic patch antennas have a much tighter confinement of the electric fields directly underneath the patch.

Table 3-1 also reports higher peak gains and peak realized gains in the heatsink antenna case. The peak realized gains include mismatch losses in addition to radiation efficiency.

3.3.2 Input Reflection Coefficient (S_{11}) and Bandwidth

The 1-port scattering parameters (input reflection coefficients) of each antenna were measured using an Agilent E8361A 10 MHz to 67 GHz PNA series network analyzer. To accompany the measurements, each antenna was simulated using HFSS.

The heatsink alter the input impedance of the antennas and therefore, the impedance matching network requires modification. The shunt transmission lines shown in Figure 3-3 and Figure 3-4 are tuning stubs for this purpose and correspond to section 3 in Figure 3-1. The basic patch antenna was matched without section 3 as shown in Figure 3-2. The placement and length of the stub for each antenna was experimentally determined for proper matching. For future implementation in chips, tuning varactors and other tunable elements can be used in the impedance matching network for electronic tuning.

Figure 3-5 demonstrates the changes in the antenna input impedance on the Smith chart due to the heatsink showing the input impedance of the basic patch antenna, basic patch with heatsink added (but no tuning stub) and finally, the heatsink antenna with the tuning stub. In Figure 3-5, the heatsink added an inductive component to the antenna. A tuning stub was also used in this case to counteract the effect. Also, note the reduced size of the locus on the Smith chart for the heatsink antenna cases, which indicates an improvement in bandwidth.

Table 3-3: Measured 10-dB bandwidth

Measured bandwidth	Patch antenna	Heatsink antenna
%	2.6	6.0
MHz	62	145

Figure 3-6 and Figure 3-7 displays both measured and simulated return loss (S_{11}) data for the 2.4 GHz patch and heatsink antennas. Figure 3-6 shows the return loss of the heatsink antenna without a tuning stub and Figure 3-7 shows the return loss of the heatsink antenna with a tuning stub. As shown in Figure 3-7, the bandwidth increases in the heatsink antenna case. The measured 10-dB return loss bandwidth increases from 2.6% (62 MHz) in the patch case to 6.0% (145 MHz) for the heatsink antenna case.

As discussed earlier, S_{11} data for the heatsink antenna show a tighter locus near the center of the Smith chart as displayed in Figure 3-5. This follows from a lower parallel resistance due to the heatsink structure and the fringing fields associated with it. The patch and heatsink antennas can be modeled by a parallel RLC circuit at resonance. Reducing the parallel resistance decreases the diameter of the S_{11} locus. As a result, the heatsink antennas show bandwidth enhancement.

The operating frequencies of each antenna can be resolved from the return loss figures. For the heatsink antenna case without the tuning stub, the resonant frequency decreased by 165

MHz (measured) and 235 MHz (simulated) [Cov]. This decrease in resonant frequency by the pin-fin heatsink will be discussed later in Chapter 5. The heatsink antenna was later re-designed with the tuning stub for impedance matching. For the case with the tuning stub, the resonant frequency is dependent upon the matching network, so it is not a good indicator of how the heatsink affects the resonant frequency. However, with the tuning stub the heatsink shifts the resonant frequency down by approximately 15 MHz (measured) and 102 MHz (simulated). The discrepancy may be in consequence to the estimated 3-D modeling of the heatsink in HFSS as discussed in previously in addition to differences in actual dielectric constant of FR4 as it varies from board to board.

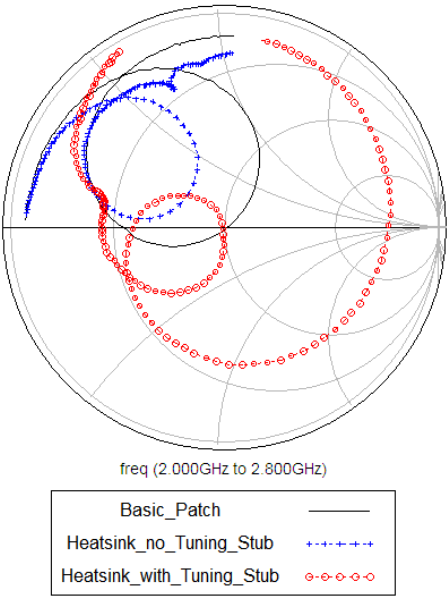


Figure 3-5. Measured S_{11} for 2.4 GHz antennas

This decrease in resonant frequency is caused by the effective increase in electrical length of the antenna due to the heatsink fins and the presence of fringing fields between the heatsink and the ground. This is similar to the reduction in required patch size for a given operating frequency due to the fringing fields of a basic microstrip patch antenna as discussed in [Mil].

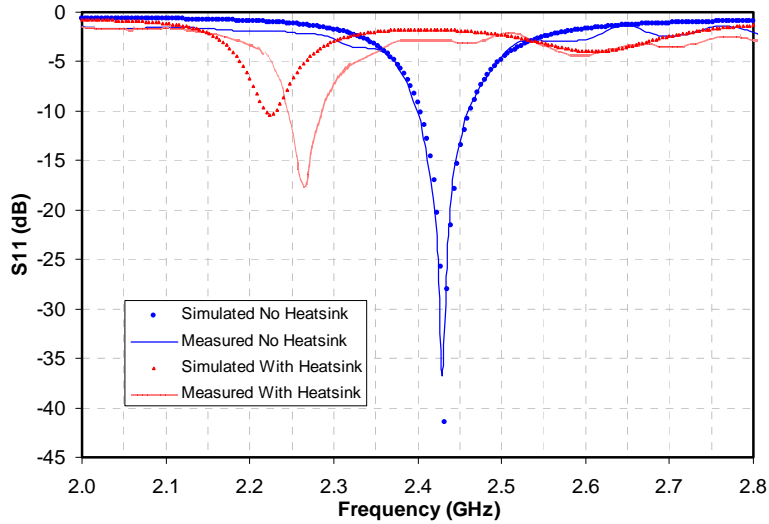


Figure 3-6. Return loss ($|S_{11}|$ (dB)) of the 2.4 GHz patch antenna and heatsink antenna without tuning stub

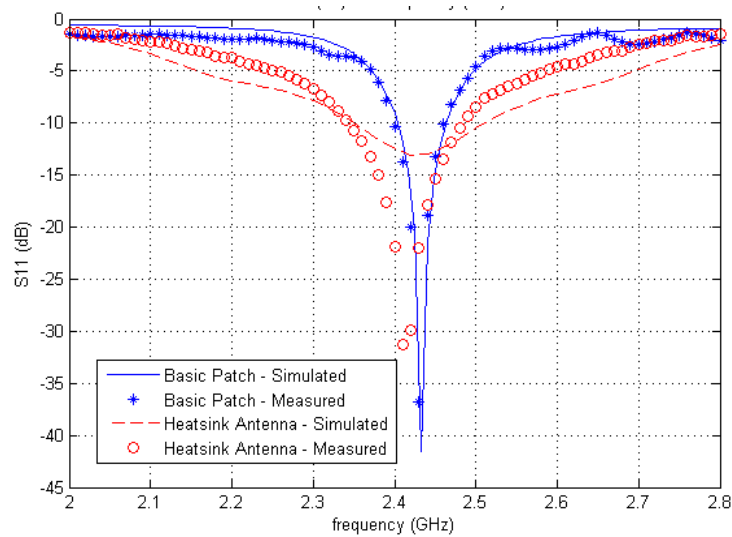


Figure 3-7. Return loss ($|S_{11}|$ (dB)) of the 2.4 GHz patch antenna and heatsink antenna with tuning stub

3.3.3 Far-Field Radiation Patterns

The radiation patterns were measured in an anechoic chamber at the Air Force Research Laboratory (AFRL), and also simulated using HFSS. Figure 3-8 and Figure 3-9 show the gain patterns for the 2.4 GHz patch antenna and heatsink antenna in the E-plane, respectively. The

measured and simulated co-polarization and measured cross-polarization are reported in these figures. The gain patterns were measured across 180 degrees in the hemisphere above the ground plane for both antennas. In the E-plane case, 180 degrees corresponds to the feed point.

The heatsink antenna shows increased gain over the basic patch antenna. Although the radiation efficiency is increased significantly, the increase in gain is less than would be expected with such a large increase in efficiency. This is due to the reduced directivity (Table 3-1). The reduced directivity is due to the change in the radiation pattern which has end-fire sidelobes instead of the single, focused broadside lobe that is typical of a patch antenna. This will be discussed further in Chapter 5.

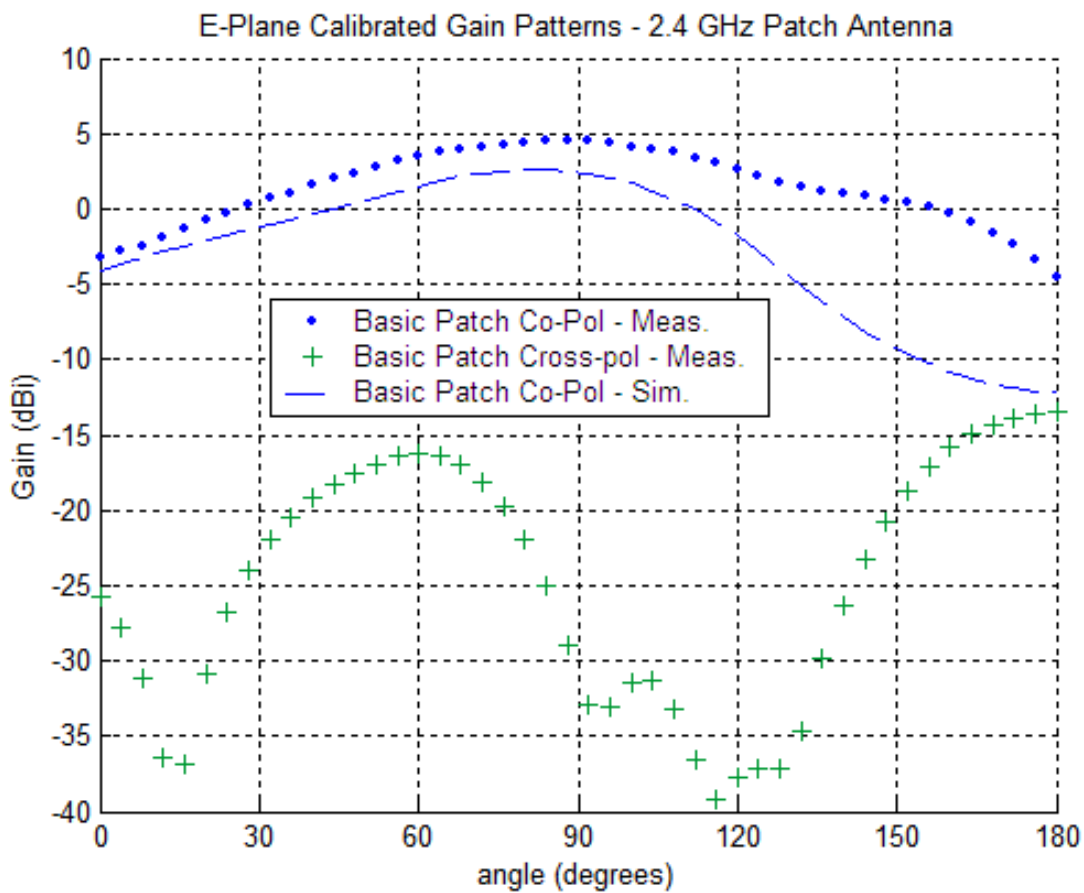


Figure 3-8. E-plane gain patterns of 2.4 GHz patch antenna

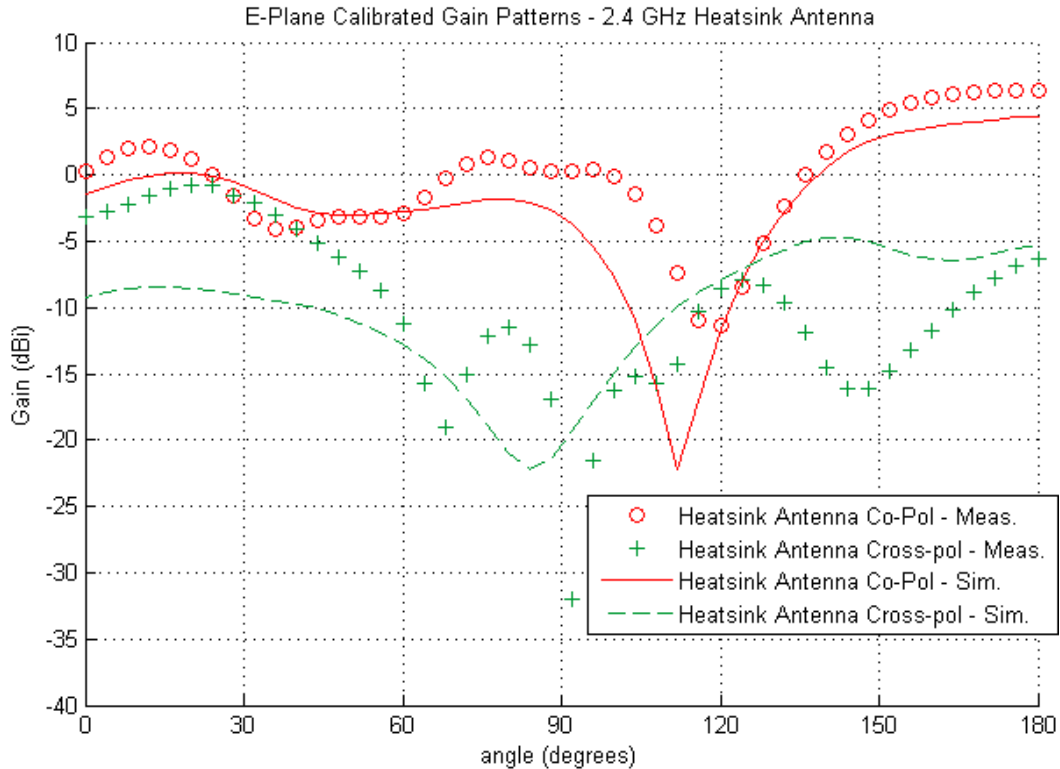


Figure 3-9. E-plane gain patterns of 2.4 GHz heatsink antenna

3.3.4 E-Field Magnitude Plots

The magnitude of the E-field for each antenna was plotted on a logarithmic scale in an E-plane cross-section. This cross-section was offset from center in order to plot between the metal fins in the heatsink case. The basic patch cross-section is also offset for consistency. The offset is 5 mm for both cases. Also, the cross-section does not intersect the tuning stub.

Figure 3-10 shows tight confinement of the electric field beneath the patch and fringing fields near the radiating edges in the basic patch case. In contrast, the fields are less confined in the heatsink case in Figure 3-11 and show the presence of fringing fields near the heatsink-air boundaries as well.

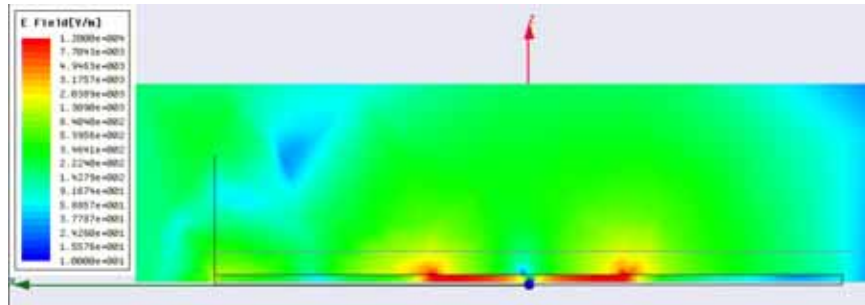


Figure 3-10. E-field magnitude plot in E-plane for 2.4 GHz basic patch

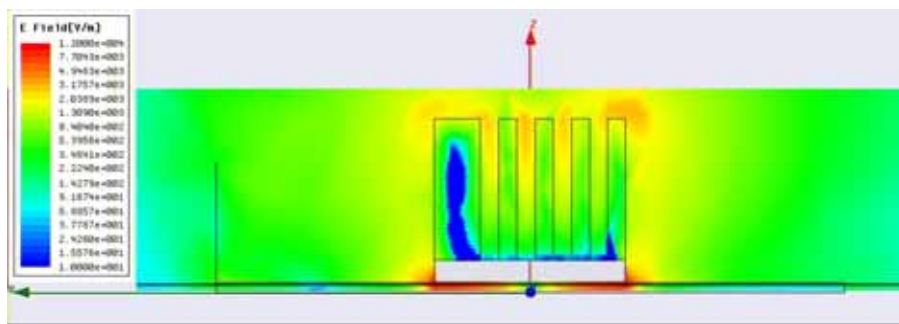


Figure 3-11. E-field magnitude plot in E-plane for 2.4 GHz HS antenna

3.3.5 Summary of Results

These results show that the heatsink structure can improve the radiation efficiency of the basic microstrip patch antenna in addition to providing a mechanism for removing harmful thermal energy away from the electronics. Although the directivity was reduced due to a change in the radiation pattern, the peak gain was increased. These performance improvements allow the use of low-cost FR4 substrates with relatively high dielectric losses to realize integrated antennas with acceptable specifications.

The heatsink structure alters the input impedance of the antenna and therefore, a modified matching network is required. A tuning stub was added to counteract the effect of the heatsink.

The bandwidth of the heatsink antenna with tuning stub increases. The bandwidth of the heatsink antenna increases more than three-fold (from 2.6% to 6%) compared with that of the patch antenna. The heatsink antenna without the tuning stub demonstrated a reduction in resonant frequency, thus reducing the required planar size of the antenna for a given operating frequency. Thus, the effective length of the antenna is increased. This may be a combination of the increase in the physical length due to the fins in addition to an effect similar to the extension of the effective open circuit due to fringing fields as in the transmission line model of a patch antenna [Mil]. The improvement of radiation efficiency and bandwidth is due to the presence of fringing fields from the heatsink to the ground plane. With the heatsink antenna, the fields are no longer confined to the lossy substrate. Instead, it increases the fields outside of the resonant cavity, and the efficiency increases. This lowers the parallel resistance by increasing the radiation conductance and reduces the size of the S_{11} locus enhancing the bandwidth.

3.4 Conclusion

This chapter evaluates the effects of using a heatsink as the antenna in order to combine the functions of two separate structures. This work was motivated by its use in 3-D SoC applications; however, the concept may be extended to any system utilizing a heatsink as the antenna, e.g., a microprocessor with built-in wireless transceiver for transmitting data). Though the heatsink antennas discussed in this chapter are relatively large compared to an integrated SoC, the goal was to address the question of whether it is possible to use a heatsink structure as an antenna. The results show that not only is this possible, but that the heatsink antenna demonstrates several performance improvements on the antenna parameters over the basic microstrip patch. The relative size of the actual heatsink antenna will depend on the operating frequency, substrate, and the specific application of the 3-D SoC system.

The heatsink antennas discussed in this chapter demonstrate higher radiation efficiencies, higher peak gain, increased bandwidth and a reduction in resonant frequency.

This study opens a new domain for interesting research on the trade-offs and characteristics of heatsink antennas in terms of heatsink structure vs. antenna parameters as well as thermal properties (such as thermal resistance [Nea, And]). This combined heatsink design and antenna design may lead to many unique and interesting radiating structures.

CHAPTER 4 EXTRUDED-FIN HEATSINK ANTENNAS AT 5.8 GHZ

4.1 Introduction

The previous chapter showed that a 2.4 GHz pin-fin heatsink antenna can be used to increase the radiation efficiency. The effect of orientation was not evaluated because a symmetrical pin-fin heatsink antenna does not have different orthogonal orientations. In contrast, an extruded-fin heatsink has two different orthogonal orientations. This orientation of the fin extrusions plays a significant role in the antenna performance, and this must be considered in heatsink antenna design with extruded fins. Therefore, two heatsink antennas were designed in the 5.8 GHz band: 1) with extruded fins parallel to the non-radiating edges (FPNRE) and 2) with extruded fins parallel to the radiating edges (FPRE). The effects of the heatsink and orientation on the radiation efficiency, peak directivity and peak gain are evaluated. The radiation patterns are also included. A discussion on bandwidth is given including a comparison of various antenna parameters versus frequency.

4.2 Design Overview

4.2.1 Antenna Design

The 5.8 GHz heatsink antennas are based on the same type of modified patch antenna structure as the 2.4 GHz heatsink antenna introduced in the previous chapter. The planar antenna provides a suitable alignment and attachment surface for the heatsink and requires only simple tuning due to the resulting change in input impedance. The patch antenna was designed using the same square patch antenna design procedures discussed in Chapter 3 [Mil]. The antennas also use the same layout as shown in Figure 3-1 which includes a square patch, quarter-wave transformer (section 1) and a 50- Ω line (section 2) in an edge-fed design. An inset-fed design cannot be used for this type of antenna, since the heatsink base would effectively remove the

inset. However, a coaxial feed from the ground layer beneath can be used for potential 3-D integration.

The patch size is 11.79 mm x 11.79 mm. Section 1 is 0.63 mm in width and 7.27 mm in length. Section 2 is 3.24 mm in width and 7.27 mm in length. These dimensions are for all three antennas (basic patch antenna, heatsink antenna with FPNRE, and heatsink antenna with FPPE). Section 3 is used only in the heatsink antenna cases for tuning the impedance matching.

The antennas were fabricated on a low-cost FR4 substrate. Figure 4-1 shows the fabricated patch antenna. The heatsinks were attached to the copper patches with silver, conductive epoxy.

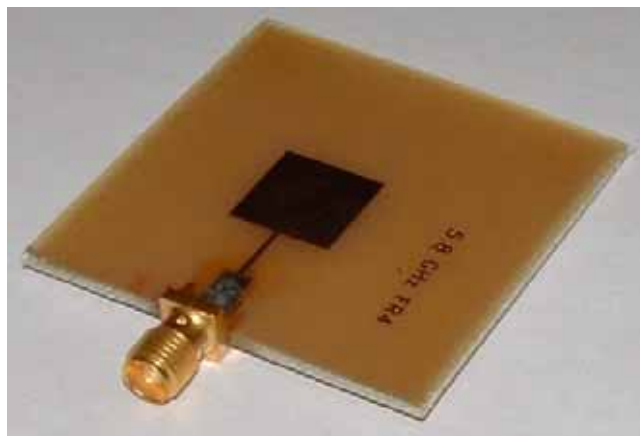


Figure 4-1. Fabricated 5.8 GHz FR4 square patch antenna

Figure 4-2 and Figure 4-3 show the fabricated heatsink antennas with fins oriented parallel to the non-radiating and radiating edges, respectively. In each of the cases, the heatsink was cut out from larger a commercially-available heatsink in order to match the dimensions of the square patch. The heatsink antennas have 3 vertical, extruded fins each having a height of 12.5 mm (not including the heatsink base which has a thickness of approximately 2.4 mm).

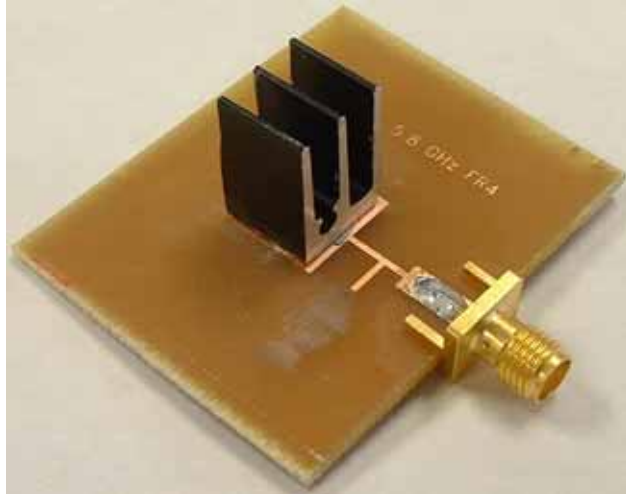


Figure 4-2. Fabricated heatsink antenna with fins parallel to the non-radiating edges (FPNRE) of the patch

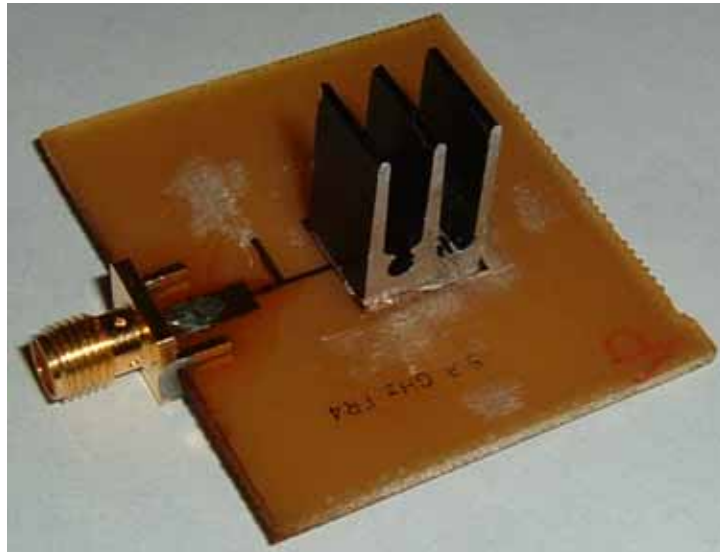


Figure 4-3. Fabricated heatsink antenna with fins parallel to the non-radiating edges (FPNRE) of the patch

For the heatsink antenna with fins parallel to the non-radiating edges, the length of the tuning stub is 3.6 mm. For the case of fins parallel to the radiating edges, the length of the tuning stub is 5.2 mm. The tuning stubs have a separation from the load (D in Figure 3-1) of 4.21 mm. The width of the shunt transmission line is equal to the width of the corresponding quarter-wave transformer.

4.2.2 HFSS Model Description

Ansoft HFSS was used for its 3-D electromagnetic modeling capabilities to simulate the heatsink antennas as well as the patch antennas with a finite ground plane. Figure 4-4 and Figure 4-5 show the 3-D HFSS model of the heatsink antenna with fins parallel to the non-radiating edges and the heatsink antenna with fins parallel to the radiating edges, respectively. The HFSS model of the basic patch antenna is not shown here for brevity, but differs only by the lack of the heatsink structure and tuning stub.

The heatsink extruded fins are rounded in the HFSS model but do not account for the fin tapering of the actual heatsink. Aluminum was used as the heatsink material in the HFSS models.

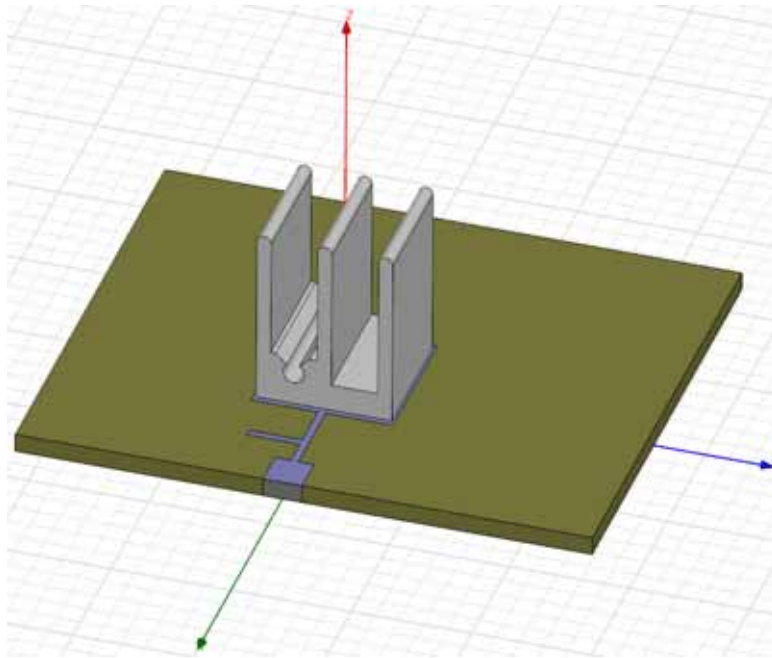


Figure 4-4. HFSS model of heatsink antenna with fins parallel to the non-radiating edges (FPNRE) of the patch

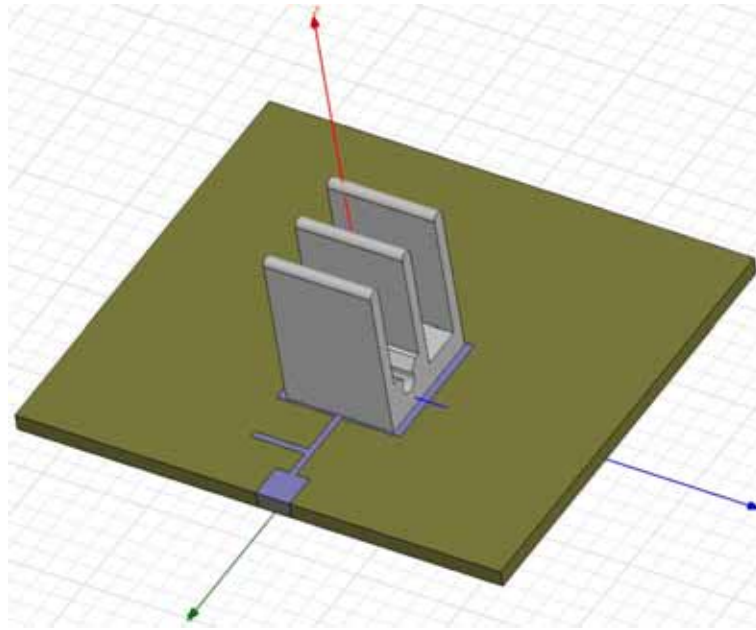


Figure 4-5. HFSS model of heatsink antenna with fins parallel to the radiating edges (FPRE) of the patch

4.3 Results and Measurements

4.3.1 Radiation Efficiency

The measured and simulated radiation efficiencies of the three antennas taken at 5.8 GHz are shown in Table 4-1 for comparison. The efficiency was measured by the Air Force Research Laboratory (AFRL) at Wright-Patterson Air Force Base. Both simulation and measurement show significant increases in efficiency due to the heatsink. The heatsink antenna with fins parallel to the non-radiating edges (FPNRE) shows radiation efficiency enhancement from 62% to 87%. Therefore, even with low-cost FR4 substrates, the antennas achieve good efficiencies. The FPRE heatsink antenna efficiency is similar (86%) at 5.8 GHz. Radiation efficiency versus frequency is discussed with bandwidth in section 4.3.2 where differences in efficiency emerge between the two orientations.

Table 4-1: Comparison of radiation efficiencies

Radiation efficiency (%)	5.8 GHz patch antenna	Heatsink antenna – FPNRE	Heatsink antenna – FPRE
Simulated	62	87	86
Measured	64	83	83

The radiation efficiency enhancement of the heatsink antenna is especially important for 3-D integration. Thermal simulations for a 3-D integrated multi-chip module show the optimum SiC substrate thickness for maximum heat transfer is 100 to 200 μm [And]. A patch antenna realized on such a thin substrate would result in poor efficiency and narrow bandwidth.

4.3.2 Bandwidth and Return Loss

The input reflection coefficient of each antenna was measured using an Agilent E8361A 10 MHz to 67 GHz PNA series network analyzer. As with the 2.4 GHz heatsink antenna, the heatsink alters the input impedance of the antennas, and therefore, the impedance matching networks require modification. The shunt transmission lines shown in Figure 4-2 through Figure 4-5 are the tuning stubs for this purpose. The basic patch antenna was designed and matched without the need of the tuning stub as shown in Figure 4-1.

Figure 4-6 shows the effect of the heatsink on the antenna S_{11} on the Smith chart due to the heatsink for the case with fins parallel to the non-radiating edges of the patch. The figure shows the S_{11} measurements of the basic patch antenna and the heatsink antenna with fins parallel to the non-radiating edges with and without the tuning stub. The size of the locus on the Smith chart is reduced which indicates an improvement in bandwidth given a proper positioning of the locus by impedance matching as discussed in Chapter 3.

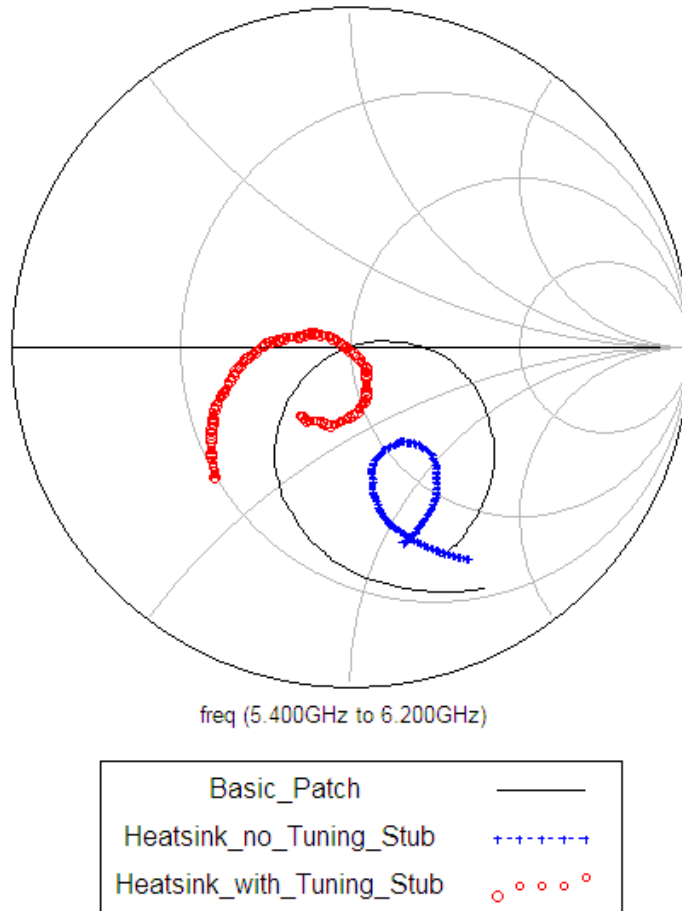


Figure 4-6. Measured input impedance for the basic patch antenna, the heatsink antenna (FPNRE) without a tuning stub, and the heatsink antenna (FPNRE) with a tuning stub

Figure 4-7 displays the measured return loss dB(|S₁₁|) data for the three antennas. The figure includes the return loss for the patch antenna and the heatsink antennas of each fin orientation.

As shown in Figure 4-7 and Table 4-2, the S₁₁ bandwidth increases significantly in both heatsink antenna cases. The measured 10-dB S₁₁ bandwidth increases from 3.1% (179 MHz) in the basic patch case to 17.6% (1.02 GHz) for the heatsink antenna with fins parallel to the non-radiating edges case. For the case of the fins parallel to the radiating edges, the bandwidth increases to 11.9% (750 MHz).

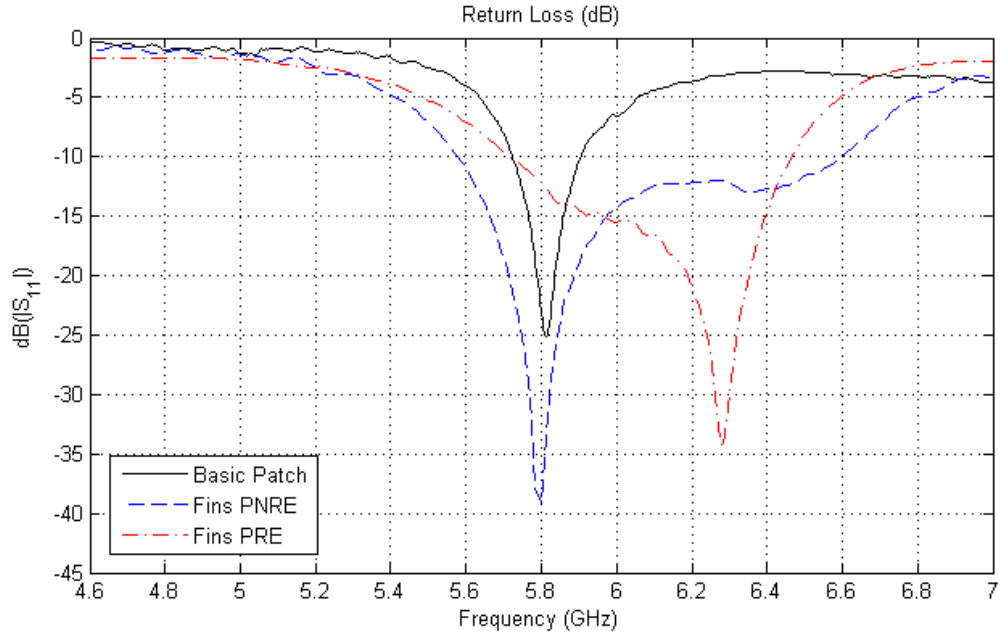


Figure 4-7. Measured return loss of the patch and heatsink antennas

Table 4-2: Measured impedance bandwidth

Bandwidth	5.8 GHz patch antenna	Heatsink antenna – FPNRE	Heatsink antenna – FPRE
MHz	179	1020	750
%	3.1	17.6	11.9

The S_{11} data for both heatsink antennas show a tighter locus near the center of the Smith chart (as displayed in Figure 4-6 for the heatsink antenna FPNRE case). This follows from a lower parallel resistance due to the heatsink structure and the fringing fields associated with it. The patch and heatsink antennas can be modeled by a parallel RLC circuit near resonance. Reducing the parallel resistance decreases the diameter of the S_{11} locus. As a result, the heatsink antennas show bandwidth enhancement when properly impedance-matched.

However, the heatsink antennas require a modified matching network, and the matching network also affects the bandwidth of the antenna. Thus, simply comparing the bandwidths of the heatsink antennas to that of the basic patch antenna does not present a fair comparison.

Therefore, a better comparison can be drawn by measuring the antenna Q. This was done by using the same matching network for all three antennas as used in the basic patch case.

Thereafter, the input impedance of the antennas was measured, and the matching networks were de-embedded using Agilent Advanced Design System (ADS). Finally, the antenna Q's were calculated. The results are reported in Table 4-3 which shows the highest Q given by the basic patch antenna. The lowest Q is achieved by the heatsink antenna with fins parallel to the non-radiating edges.

Table 4-3: Measured antenna Q

5.8 GHz patch antenna	Heatsink antenna – FPNRE	Heatsink antenna – FPPE
22.2	13.2	14.7

As with fractal antennas, this bandwidth improvement with the 3-D heatsink antenna cases is in agreement with a discussion in [Bal] which indicates that the bandwidth of an antenna enclosed by a sphere can be improved if the antenna uses the available volume within the sphere more efficiently with its geometrical configuration. Further bandwidth improvement may be achieved with a 3-D fractal geometry serving as both antenna and heatsink.

Figure 4-8 through Figure 4-10 show how the radiation efficiency, peak directivity, and peak gain vary across a frequency range in simulation and are thus included in the bandwidth discussion. It is clear from Figure 4-8 that the heatsink antenna with fins parallel to the non-radiating edges has a wider efficiency bandwidth compared to the heatsink antenna of the opposite orientation (FPPE). The FPNRE case has an efficiency greater than the patch antenna across the entire frequency range. In the FPPE case, the efficiency is similar to that of the FPNRE case up to 6.2 GHz but falls sharply at higher frequencies.

Figure 4-9 and Figure 4-10 show the peak directivity and peak gain versus frequency for the three antennas. The directivity for the FPNRE case is higher than the patch antenna directivity across the entire frequency range shown. The heatsink antenna in this case has a more focused broadside lobe than the patch antenna. The fins are parallel with the current flow on the patch. In contrast, the heatsink antenna FPRE case has fins perpendicular to the current flow on the patch. In this case, the directivity is significantly lower than that of the patch antenna for most of the frequency range due to two end-fire sidelobes in the E-plane (this is shown later in Figure 4-11) in addition to the normal broadside lobe of a patch.

The peak gain of the FPNRE case is greater than that of the basic patch across the entire frequency range. Due to the decreasing radiation efficiency versus frequency and the increasing directivity versus frequency, the peak gain in the FPNRE case is relatively flat across the frequency range above 5.4 GHz as shown in Figure 4-10 and is higher than the basic patch peak gain across the entire band. The FPRE case shows a reduced peak gain versus frequency and is lower than that of the patch antenna for most of the range due to the reduced directivity. This demonstrates the significant difference in antenna performance depending on the orientation of the extruded fins.

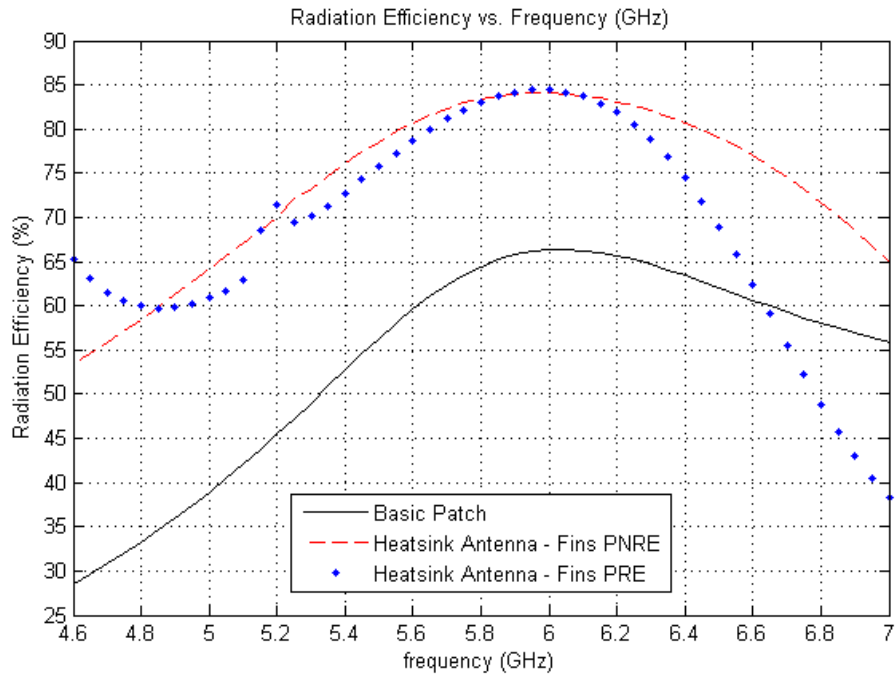


Figure 4-8. Radiation efficiency vs. frequency

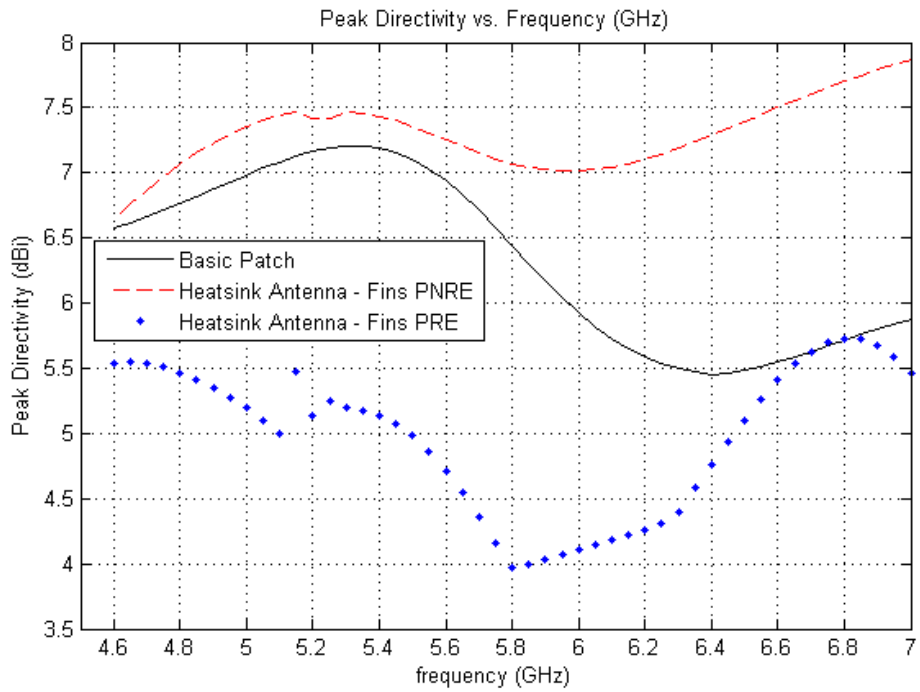


Figure 4-9. Peak directivity (dBi) vs. frequency

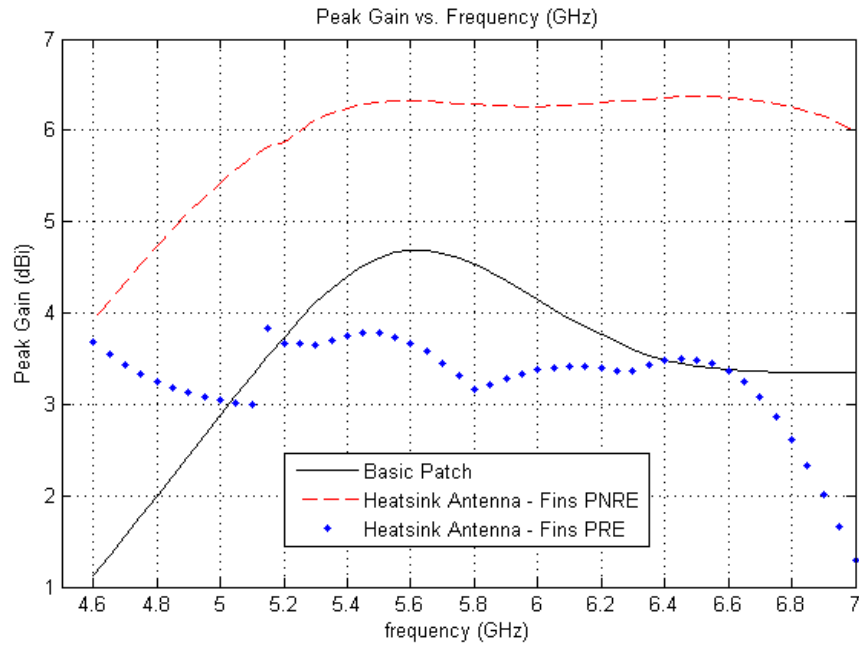


Figure 4-10. Peak gain (dBi) vs. frequency

4.3.3 Far-Field Radiation Patterns

The radiation patterns were measured in a compact far-field antenna range at the Air Force Research Laboratory (AFRL), and also simulated using HFSS. The gain patterns are shown in Figure 4-11 and Figure 4-12 for the basic patch and heatsink antennas in the E- and H-planes, respectively. The measured and simulated co-polarization and measured cross-polarization are reported in these figures. The gain patterns were measured across 180 degrees in the hemisphere above the ground plane where 90 degrees is broadside to the patch. In the E-plane case, 180 degrees corresponds to the feed point. The antenna patterns are shown at the frequency corresponding to the lowest return loss for each antenna in Figure 4-7.

For the FPNRE heatsink antenna case, the peak gain increased in both simulation and measurement due to the heatsink structure. The broadside lobe is more focused than that of the patch. The peak gain increased from 4.5 dBi to 6.3 dBi in simulation and from 4.9 dBi to 7.3 dBi in measurement. However, in the FPRE heatsink antenna case, the peak gain is reduced to

3.3 dBi in simulation and 4.1 dB in measurement. This is approximately 3-4 dB lower than the FPNRE case even though the respective radiation efficiencies are comparable. This follows from the reduced directivity in the FPRE case due to two end-fire sidelobes (shown in Figure 4-11 for the FPRE case) in addition to the typical broadside lobe. The fins lie perpendicular to the current flow on the patch such that vertical surface currents are generated on the fins. These vertical currents on the fins act like an array of monopoles radiating end-fire in the E-plane. Thus, the orientation of the extruded fins with respect to the radiation pattern is extremely important, and the optimal choice depends on the application. Applications may exist where the end-fire radiation is desired.

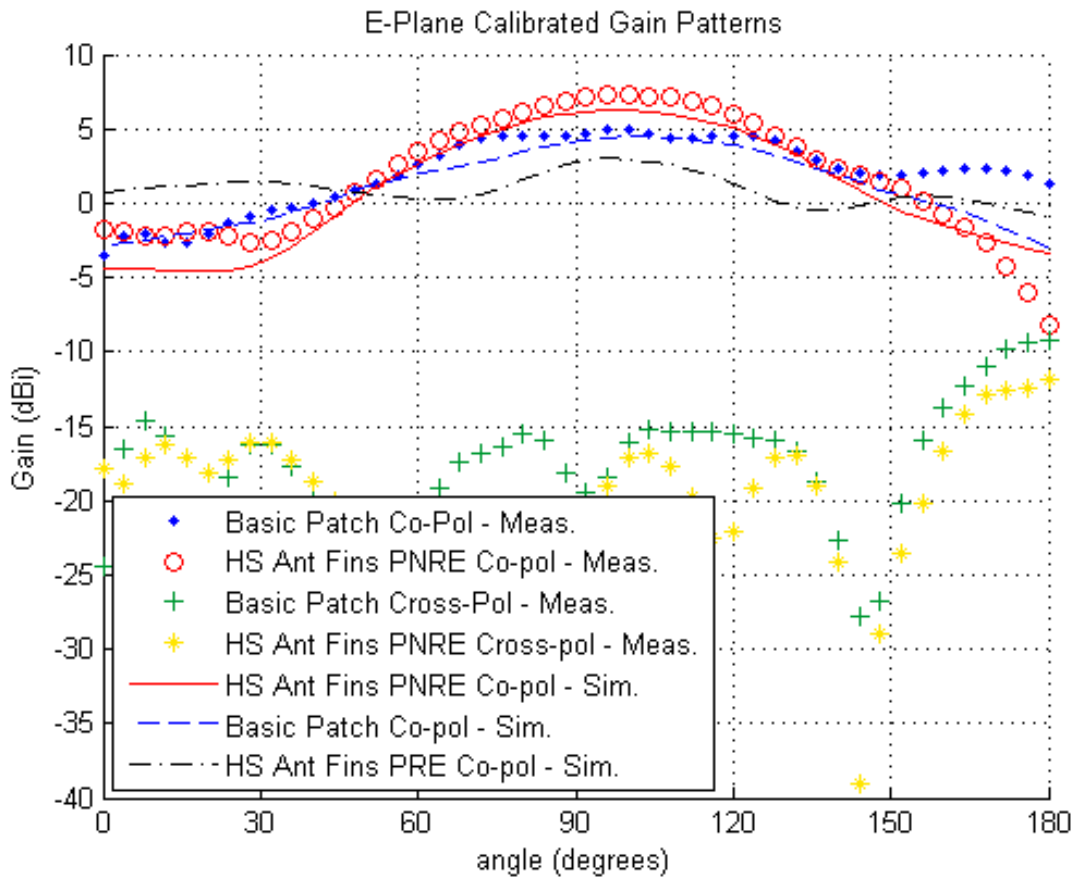


Figure 4-11. E-plane gain patterns

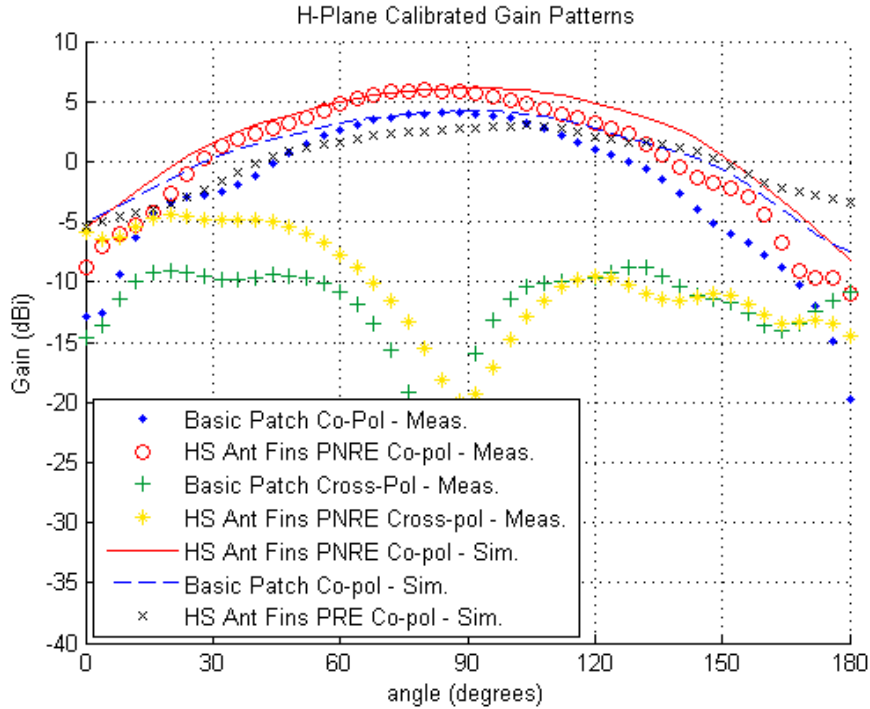


Figure 4-12. H-plane gain patterns

4.3.4 E-Field Plots

The E-field vector plots for the three antennas were plotted in a log scale on an E-plane cross-section. This cross-section was offset from center in order to plot between the metal fins in the heatsink cases. The basic patch cross-section is also offset for consistency. The offsets are 3 mm for all three cases. The cross-sections do not intersect the tuning stubs.

Figure 4-13 shows tight confinement of the electric field beneath the patch and fringing fields near the radiating edges in the patch antenna case. In contrast, the fields are less confined in the heatsink antennas cases (shown by color) in Figure 4-14 and Figure 4-15.

The two orientations of heatsink fins result in dramatically different E-field distributions. Since the height of the fin is comparable to the length of the patch, there is a significant phase retardation from the bottom of the heatsink to the top of the fins when the fins are parallel to the radiating edges, and the direction of the fringing E-field vectors at the bottom of the heatsink and

the direction at the top of the heatsink fins are opposite. It is clear from Figure 4-15 that in the case with fins parallel to the radiating edges (FPRE), the E-field distribution is significantly perturbed compared to that of the traditional patch antenna. Thus, the radiation pattern is less focused and the directivity is reduced. As shown in Figure 4-9, the peak directivity of this case is less than 4 dBi at 5.80 GHz (compared with more than 7 dBi in the FPNRE case).

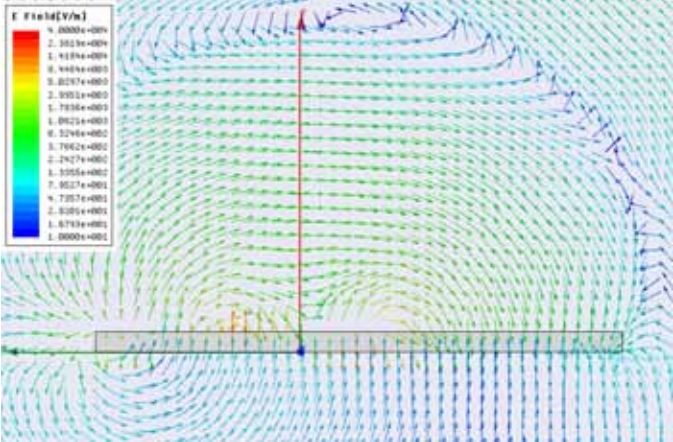


Figure 4-13. E-field vector plot in E-plane for basic patch antenna at 5.80 GHz

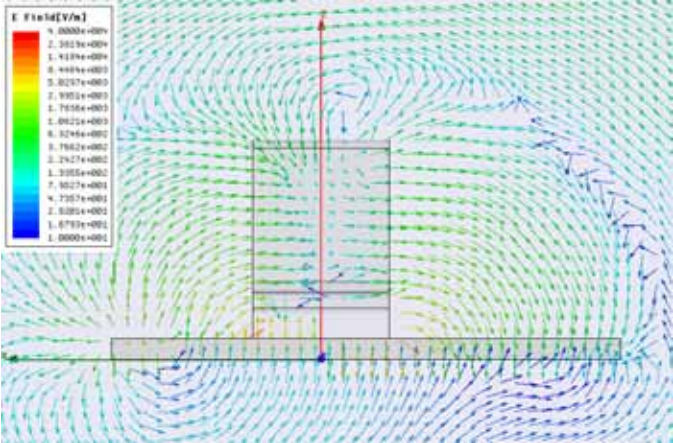


Figure 4-14. E-field vector plot in E-plane for heatsink antenna with Fins PNRE at 5.80 GHz

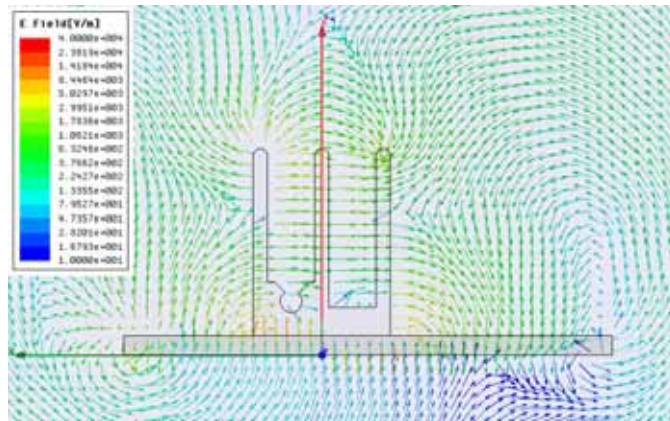


Figure 4-15. E-field vector plot in E-plane for heatsink antenna with Fins PRE at 5.80 GHz

The magnitude of the E-field for each antenna was also plotted in log scale on an E-plane cross-section in Figure 4-16, Figure 4-17, and Figure 4-18 for the patch antenna, the FPNRE case and the FPRE case, respectively. As with the vector plots, this cross-section was offset from center in order to plot between the metal fins in the heatsink cases. The basic patch cross-sections are also offset for consistency. The offset is 3.0 mm for the three antennas. Also, the cross-sections do not intersect the tuning stubs. It can be observed in the figures that the basic patch case has much tighter confinement of the E-field in the lossy substrate directly below the patch.

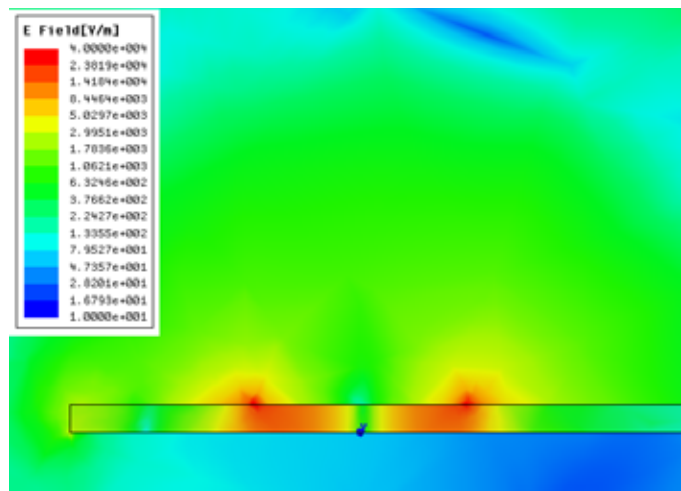


Figure 4-16. E-field magnitude plot in E-plane for 5.8 GHz basic patch

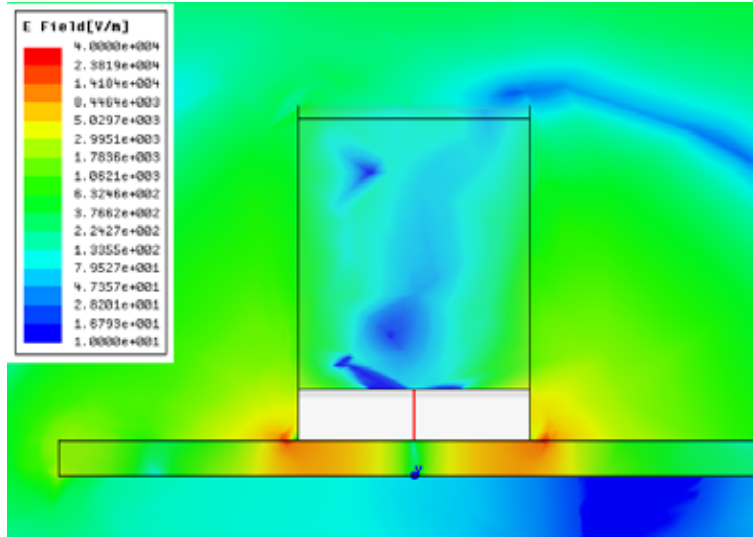


Figure 4-17. E-field magnitude plot in E-plane for the FPNRE case at 5.8 GHz

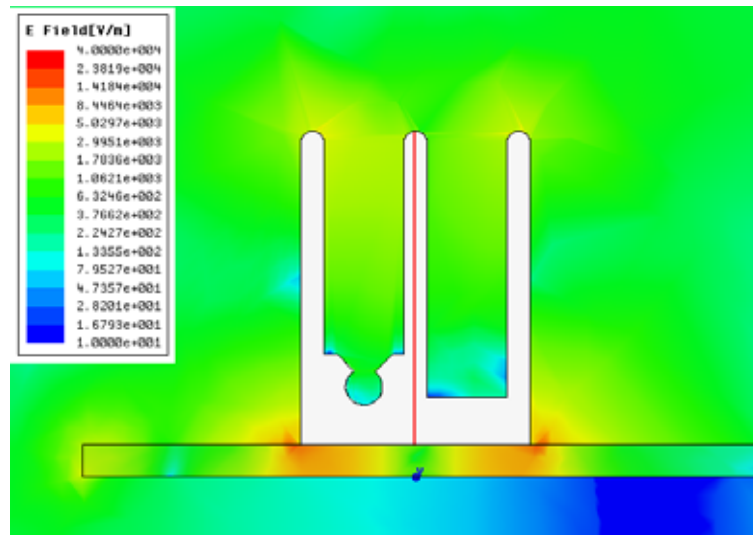


Figure 4-18. E-field magnitude plot in E-plane for the FPRE case at 5.8 GHz

4.3.5 Summary of Results

The results show that significant performance improvements are obtained with the heatsink antenna over the patch antenna on a low-cost substrate. The fin orientation has a

significant impact. Increased radiation efficiency over the patch antenna for both fin orientations was achieved. The efficiency increases from 62% for the patch antenna to approximately 87% for the heatsink antennas. Furthermore, the efficiency bandwidth is wider in the case of the non-radiating edges compared to the radiating edge case.

The S_{11} bandwidth also increases in both heatsink antenna cases and almost six-fold for the case with fins parallel to the non-radiating edges (from 3.1% to 17.6%). The heatsink structure alters the input impedance of the antenna, and therefore, a modified matching network is required. A tuning stub was added to counteract the effect of the heatsink, and thus, the antenna Q was also measured by removing the effect of the modified matching network. The results show lower Q with both heatsink antenna cases. The geometric configuration of the heatsink antenna utilizes the antenna volume more efficiently.

The improvement of radiation efficiency and gain is due to the presence of fringing fields from the heatsink to the ground plane. It increases the fields outside the resonant cavity reducing dielectric losses and improving the radiation efficiency. A more complex 3-D heatsink structure may further increase the efficiency and bandwidth.

The orientation of the fins also plays a significant role in the peak directivity and peak gain of the antenna. The gain increases from 4.5 dBi with the patch antenna to 6.3 dBi in the case of the fins parallel to the non-radiating edge. The opposite is true for the radiating edge case where the gain is reduced to approximately 3.3 dBi. As shown in Figure 4-10, the non-radiating edge case has a flat peak gain response across a broad frequency range. Thus, the radiation pattern of the antenna can be significantly altered simply by the orientation of the extruded fins with respect to the radiating and non-radiating edges of the patch.

4.4 Conclusion

An impedance-matched, 5.8 GHz extruded-fin heatsink antenna was introduced having two orthogonal fin orientations. The orientation was shown to have a significant effect on the antenna directivity and gain performance across a frequency range. Thus, the extruded-fin heatsink provides the flexibility of either a high- or low-directivity antenna simply by the orientation of the fins. The best choice will be determined by the specific application.

Furthermore, the results demonstrated that the extruded-fin heatsink can improve the radiation efficiency and bandwidth of a basic microstrip patch antenna while reducing component count and providing a mechanism for removing thermal energy from high-power electronics such as an RF power amplifier. These performance improvements allow the use of low-cost, lossy FR4 substrates (which would typically be considered a poor substrate choice) with high dielectric losses to realize integrated antennas with favorable efficiency and bandwidth.

The heatsink antennas discussed in this chapter had a fixed fin height. The next chapter will examine not only the effect of orientation but also the effect of the fin height on the antenna performance. Another common type of heatsink, the pin-fin heatsink, is evaluated for its use as a heatsink antenna and is compared with the extruded-fin type.

CHAPTER 5 FIN HEIGHT AND ORIENTATION EFFECTS OF EXTRUDED-FIN AND PIN-FIN HEATSINK ANTENNAS

5.1 Introduction

The previous chapter introduced the extruded-fin heatsink antenna and how the heatsink affected the antenna performance. While the orientation of the heatsink was studied, the heatsink's fin height was fixed. It is important to evaluate the effects of the fin height and orientation on the antenna characteristics, since other effects may be revealed, and the antennas may behave very differently depending on these parameters. These effects may be exploited to improve the antenna performance.

An extruded-fin heatsink with three fins was used in this study based on a patch antenna designed for 5.8 GHz. The fin height was varied along two orientations: fins parallel to the non-radiating edges (FPNRE) of the patch and fins parallel to the radiating edges (FPRE) of the patch. Also, a 2-finned heatsink antenna was simulated in such a manner to isolate the effect of the center fin. Next, the effects of fin height were evaluated for a pin-fin heatsink antenna.

5.2 Simulation and Measurement Setup

5.2.1 Simulation Setup

Simulations were performed using Ansoft HFSS to determine the effects of the fin height and orientation on the antenna properties. The Ansoft HFSS simulation setup was identical to that of the edge-fed 5.8 GHz basic patch antenna model discussed previously in Chapter 4. However, a simple heatsink structure was used instead of the complex heatsink structure of the 5.8 GHz heatsink antenna discussed in the previous chapter. The new heatsink structure has three vertical fins which are purely rectangular. The dimensions of the antennas and their heatsink structures are listed in Table 5-1.

Table 5-1. Antenna and heatsink dimensions for HFSS setup

Parameter (mm)	5.8 GHz antenna
Planar patch dimensions	11.79 x 11.79
Quarterwave transformer width	0.63
Quarterwave transformer length	7.27
Fifty-ohm line width	3.24
Fifty-Ohm line length	7.27
Heatsink base thickness	0.80
Heatsink base dimensions	11.79 x 11.79
Fin thickness	1.00

The HFSS models of the 3-finned extruded-fin heatsink antennas are shown in Figure 5-1 and Figure 5-2. The heatsink of Figure 5-1 has its fins oriented parallel to the non-radiating edges (FPNRE) of the patch (parallel to the x-axis in the figure), while the heatsink fins in Figure 5-2 lie parallel to the radiating edges (FPRE) of the patch (or parallel to the y-axis) [Bal].

The patch antenna is represented by two radiating slots and two non-radiating slots. The radiating slots (or edges) are along the width of the patch while the non-radiating slots (or edges) are along the length of the patch. Figure 5-3 shows a cross-section of the patch antenna along the length. As shown in the figure the electric field varies $\lambda/2$ cycle along the length for the fundamental TM_{10} mode. However, the field strength and direction is relatively constant along the patch width. The fringing fields in Figure 5-3 occur at the radiating edges of the patch. The vertical components are equal and opposite and cancel each other out; however the horizontal components are in the same direction and interfere constructively. Thus, these two edges are referred to as the radiating edges. Along the non-radiating edges, the electric field strength and direction varies along the length. Therefore, both the horizontal and vertical components interfere destructively and very little radiation occurs from these edges [Kum, Bal].

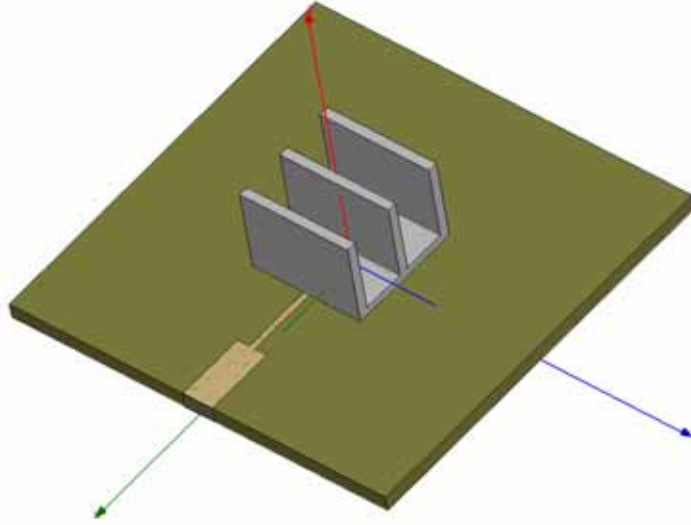


Figure 5-1. HFSS model of 3-finned 5.8 GHz heatsink antenna with fins parallel to non-radiating edges

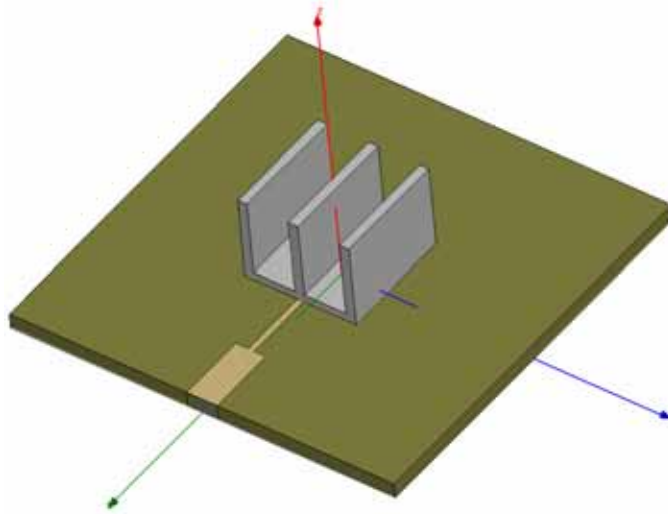


Figure 5-2. HFSS model of 5.8 GHz heatsink antenna with fins parallel to radiating edges

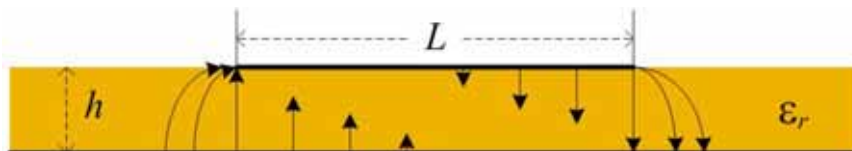


Figure 5-3. Cross-section of patch antenna along the length showing electric field lines

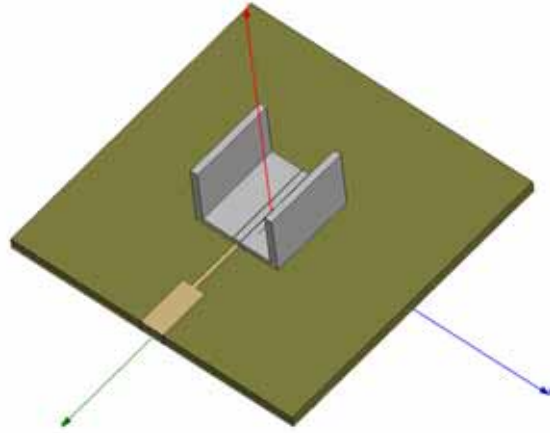


Figure 5-4. HFSS model of 2-finned 5.8 GHz heatsink antenna with fins parallel to non-radiating edges

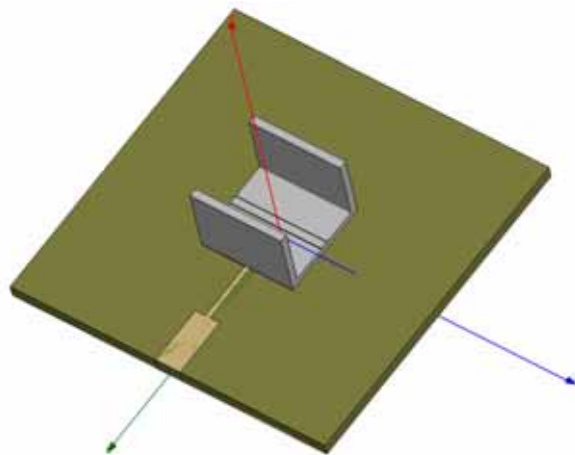


Figure 5-5. HFSS model of 2-finned 5.8 GHz heatsink antenna with fins parallel to non-radiating edges

A two-finned heatsink structure was also simulated by removing the center fin. Figure 5-4 and Figure 5-5 show the HFSS model for the 5.8 GHz 2-finned heatsink antennas with fins parallel to the non-radiating and radiating edges, respectively. In this manner, the degree to which the center fin affects the antenna parameters can be evaluated. The center fin is actually still present, but the height was reduced to 0.001 mm.

5.2.2 Measurement Setup

In order to verify the simulations, heatsink antennas needed to be fabricated and measured. Ten 3-finned extruded-fin heatsink antennas were constructed using FR4 board with a thickness of 1.6 mm. To reduce the number of antennas that must be fabricated, five different fin heights at each of the two orientations were selected (2 mm, 6 mm, 12 mm, 16 mm, and 20 mm) giving a total of ten antennas. In this manner, the measurement results should validate the simulations across the fin height range. The ten heatsinks were custom-machined out of aluminum by a commercial machining company to the author's specifications. The heatsink dimensions are specified in Table 5-1. The ten antennas are shown in Figure 5-6 with ascending fin heights from left to right. The antennas on the top row have the FPNRE orientation while the antennas on the bottom row have the FPPE orientation.

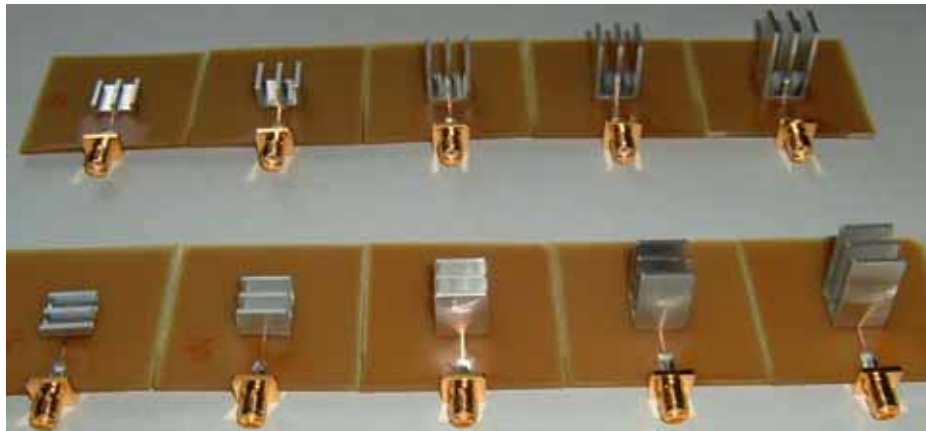


Figure 5-6. Fabricated 5.8 GHz heatsink antennas for fin height sweep

5.3 Three-Finned Heatsink Antenna Results

Simulations were performed by sweeping the fin height starting at 0.001 mm by a 1 mm step-size up to 22.001 mm at each of the two orientations. The 0.001 offset prevents the HFSS simulation errors which would arise from a 3-D structure (fin) having a dimension (fin height) of 0 mm. This offset, however, is negligible. The antenna parameters for the basic microstrip

patches at 5.8 GHz are shown in Table 5-2 for comparison to the heatsink antenna results reported later.

Table 5-2. Antenna parameters for the basic patch antenna (simulated)

Parameter	5.8 GHz patch antenna
Resonant Frequency (GHz)	5.77
Radiation Efficiency (%)	62.7
Peak Directivity (dBi)	7.33
Peak Gain (dBi)	5.36

5.3.1 Input Reflection Coefficient and Resonant Frequency Analysis

First, the effect of the fin height on the resonant frequency is evaluated. As the fin height increases, a second locus appears in addition to the single locus of a traditional patch antenna, for both fin orientations and the antenna has two resonant frequencies. This is demonstrated by the input reflection coefficient (S_{11}) in Figure 5-8 on the Smith chart for the 5.8 GHz 3-finned heatsink antenna with a fin height of 12 mm and fins parallel to the radiating edges and Figure 5-9 for the heatsink antenna with 16 mm fins parallel to the non-radiating edges. The single-locus behavior of basic patch antennas is demonstrated by the S_{11} data in Figure 5-7 for comparison to the dual-loci behavior of the 3-finned heatsinks.

The measured versus simulated return loss data were compared. The return loss data for the FPNRE orientation are shown in Figure 5-10 through Figure 5-14 while the data for the FPRE orientation are shown in Figure 5-15 through Figure 5-19. Both simulated and measured data are shown in the figures for fin heights of 2 mm, 6 mm, 12 mm, 16 mm, and 20 mm over a frequency range of 1 GHz to 10 GHz. The simulations match well with the measured results. Variations occur mainly at high frequency due to the changes in loss tangent and dielectric constant of FR4 over frequency.

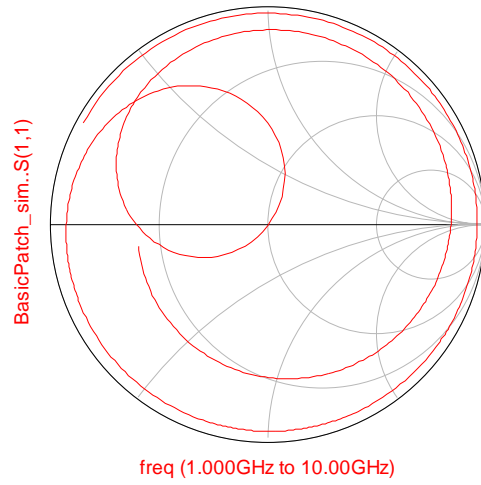


Figure 5-7. S_{11} of 5.8 GHz basic patch antenna

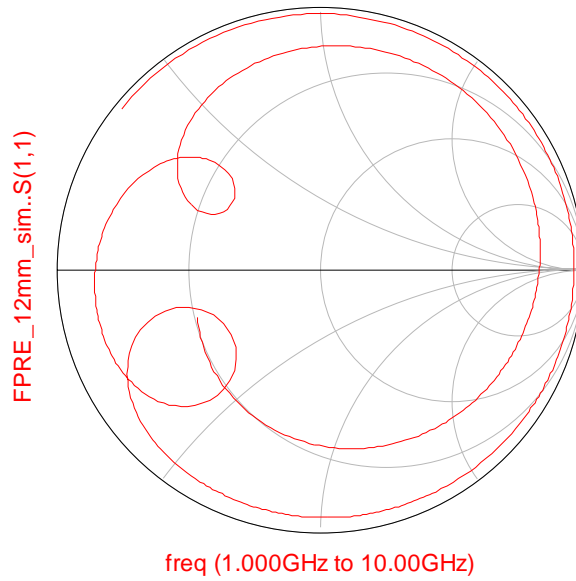


Figure 5-8. S_{11} of 5.8 GHz heatsink antenna with fin height = 12 mm along the radiating edges (FPRE)

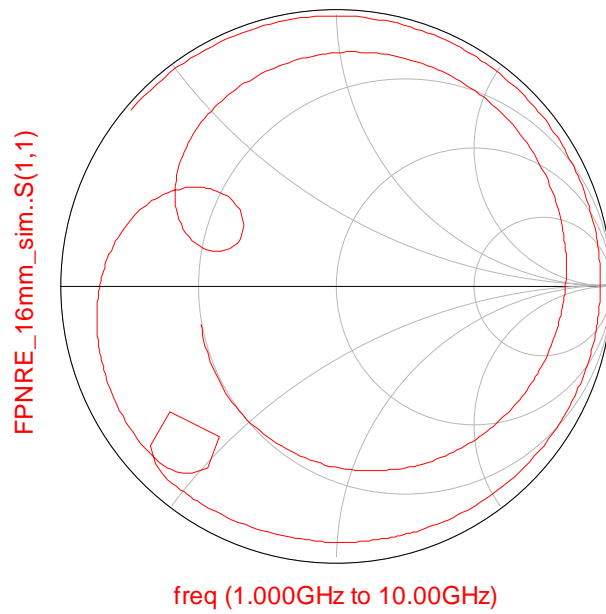


Figure 5-9. S_{11} of 5.8 GHz heatsink antenna with fin height = 16 mm along the non-radiating edges (FPNRE)

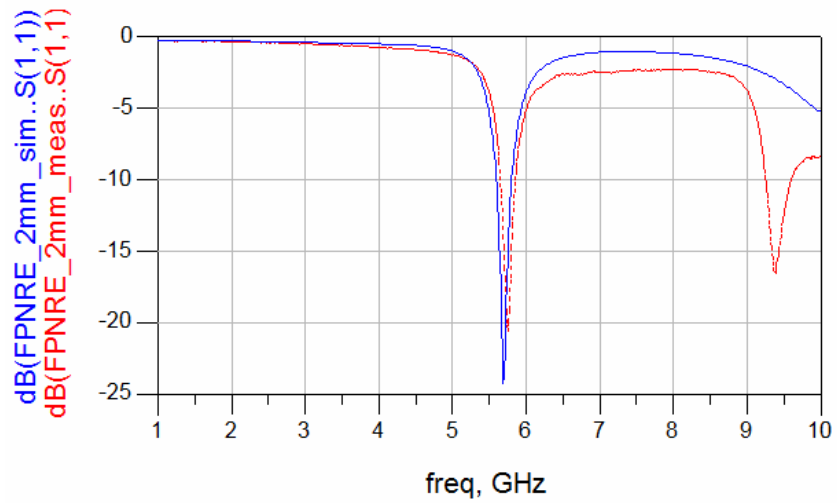


Figure 5-10. S_{11} of FPNRE with fin height = 2 mm

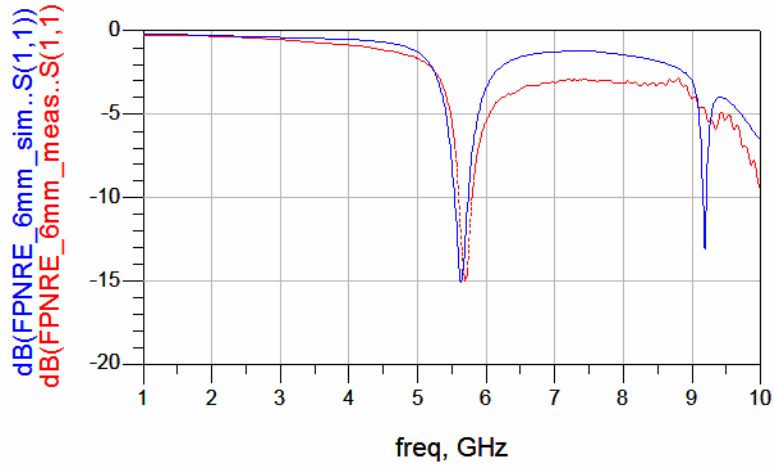


Figure 5-11. S_{11} of FPNRE with fin height = 6 mm

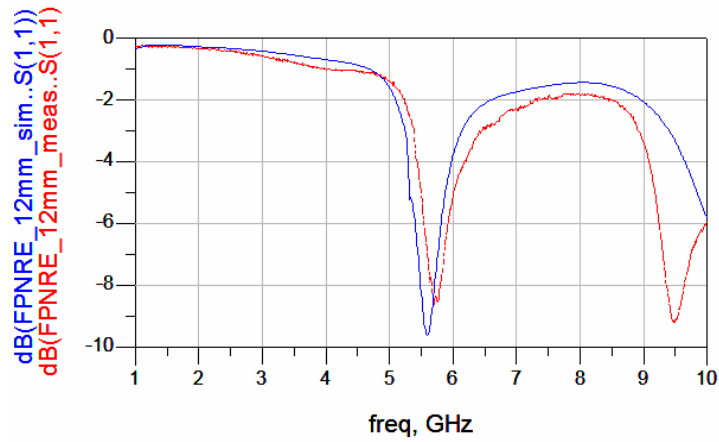


Figure 5-12. S_{11} of FPNRE with fin height = 12 mm

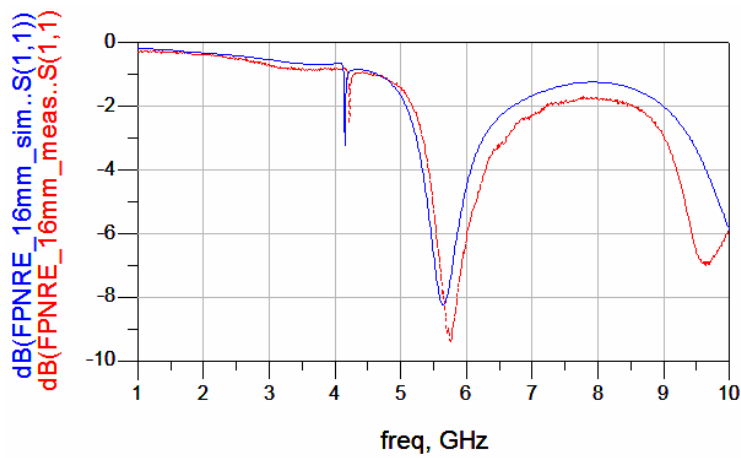


Figure 5-13. S_{11} of FPNRE with fin height = 16 mm

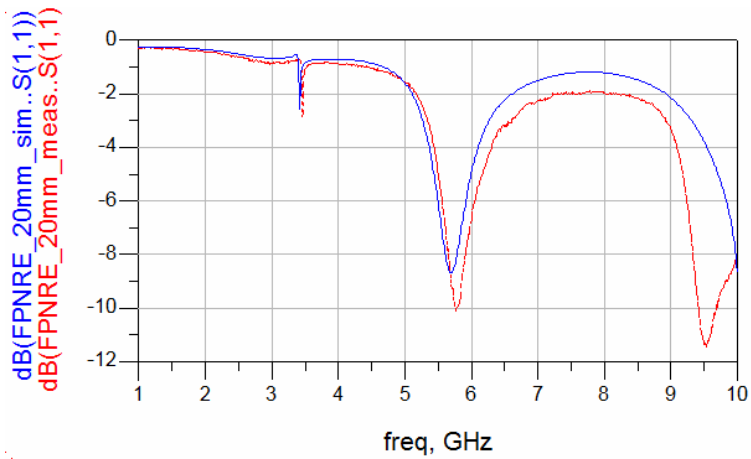


Figure 5-14. S_{11} of FPNRE with fin height = 20 mm

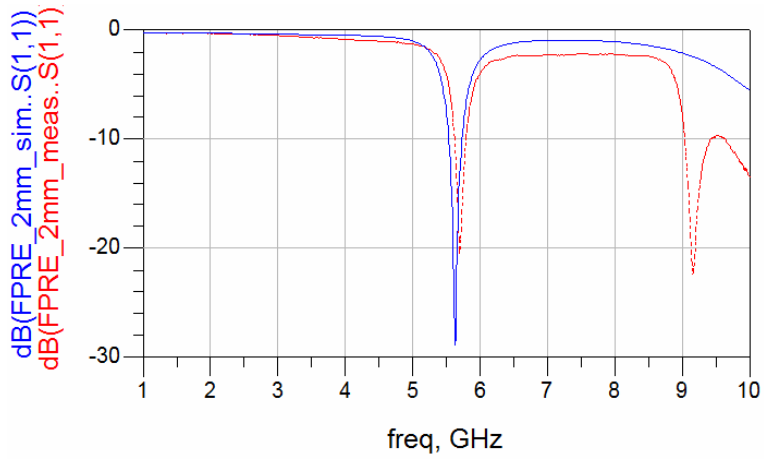


Figure 5-15. S_{11} of FPPE with fin height = 2 mm

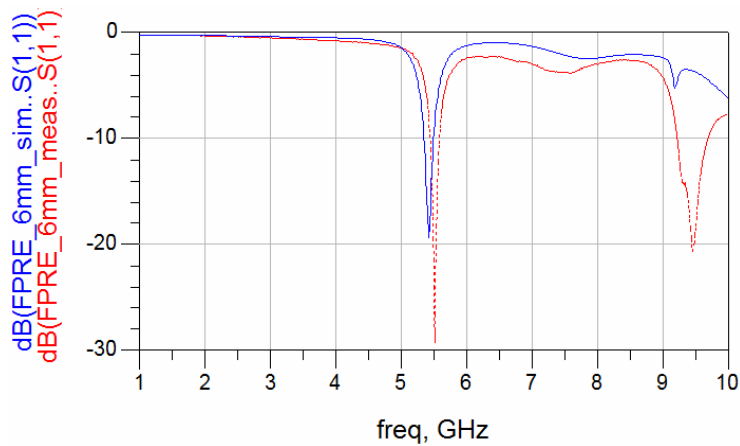


Figure 5-16. S_{11} of FPPE with fin height = 6 mm

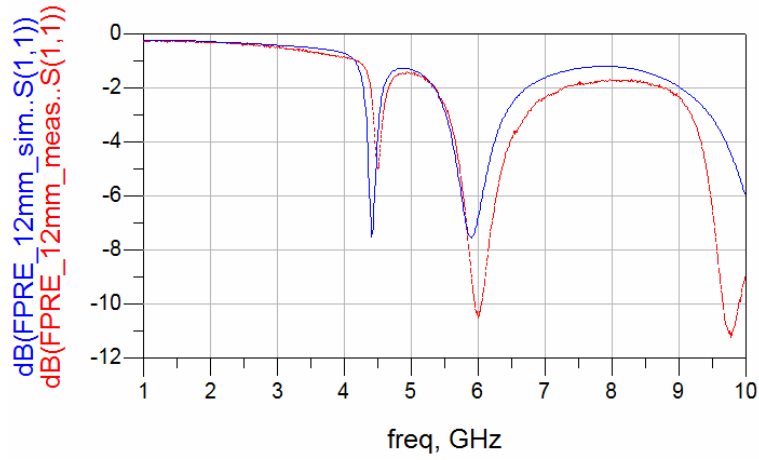


Figure 5-17. S_{11} of FPRE with fin height = 12 mm

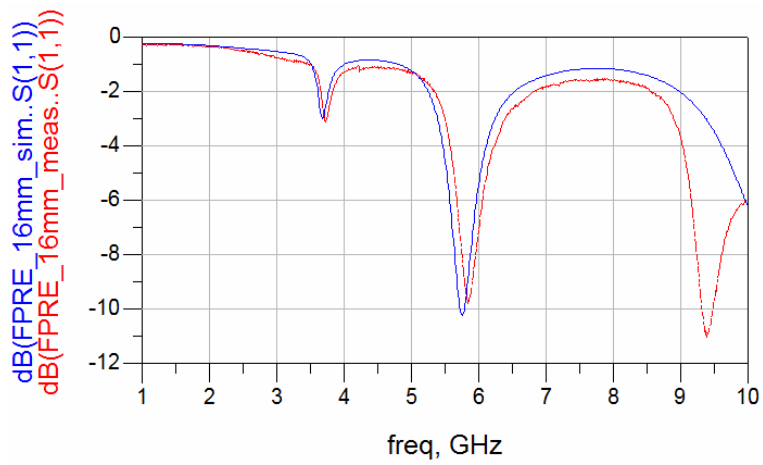


Figure 5-18. S_{11} of FPRE with fin height = 16 mm

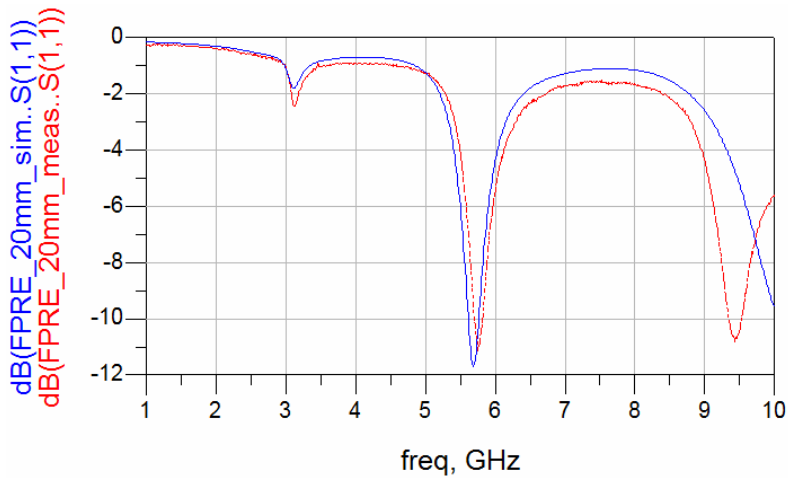


Figure 5-19. S_{11} of FPRE with fin height = 20 mm

The measured and simulated resonant frequencies for the non-radiating and radiating edge cases are plotted in Figure 5-20 and Figure 5-21, respectively. The measured data match well with simulation. The heatsink type, fin height, and orientation significantly affect the resonant frequencies of the antenna. Both orientations give rise to primary and alternate resonances. The primary resonance is labeled such due to its origination from the fundamental TM_{10} mode of the patch. As the fin height increases, a second resonance appears. This resonance is labeled “alternate resonance” instead of “secondary resonance” since the frequency can be higher or lower than the primary depending on the fin height.

The resonant frequencies versus fin height for the fins parallel to the non-radiating edges (FPNRE) orientation are shown in Figure 5-20. For this orientation, the primary resonant frequency is relatively constant across the fin height range; and thus, the fundamental mode of the patch is practically unaltered by the heatsink fins in this orientation. The small variation of the primary frequency that occurs is possibly due to the fins slightly changing the effective slot capacitance. The alternate frequency decreases monotonically with fin height and is due to the resonance between the center fin and the two outer fins. Removing the center fin eliminates this alternate resonance but has almost no effect on the primary resonance. This will be discussed further later.

The resonant frequencies for the FPPE case behave in a substantially different manner. While the primary resonant frequency of the non-radiating edge case was relatively constant across the fin height range (maximum deviation = 146 MHz in simulation), the opposite is true for the primary resonant frequency of the radiating edge case (maximum deviation = 2.846 GHz in simulation). In this case, the increasing fin height significantly lowers the primary resonant frequency. The fins being parallel to the radiating edges of the patch effectively increase the

length of the patch which lowers the resonant frequency. An alternate resonance also occurs with this fin orientation (FPRE), however, it is not caused by the center fin. Removing the center fin has almost no effect on either the primary or alternate resonant frequencies with the FPRE orientation. The results of the pin-fin heatsink antenna are given in later in the chapter, and they will show that the results are very similar to this FPRE orientation. Both the pin-fin antenna and the FPRE extruded-fin antenna have discontinuities in heatsink material along the direction of the patch current flow which prohibits longitudinal fin currents. The other orientation (FPNRE) has fins longitudinal with the patch current flow, and thus, the longitudinal fin currents can exist.

The resonant frequency results show that the fin height and orientation have a substantial effect. Both orientations have dual-frequency behavior over the frequency range shown. This is important since it may eliminate the need for two separate antennas for two operating bands. Dual-frequency microstrip antennas have been published extensively [Mac1, Mac2, Lu, Het, She]. In the FPNRE case, the primary resonance is less dependent on fin height which can simplify the heatsink antenna design. In the FPRE case, the primary resonant frequency can be reduced significantly by increasing the fin height. This can be used to reduce the planar size of the antenna. Reducing the planar size of patch antennas has been the focus of several studies [Pio, Kim1, Lee2, Raj].

The E-field plots for the primary and alternate resonances of the 3-fin extruded-fin heatsink antenna are shown in Figure 5-22 and Figure 5-24 for the FPNRE and FPRE cases, respectively. Figure 5-23 shows how removing the center fin eliminates the alternate frequency in the FPNRE case. In the FPRE case, however, removing the center fin has almost no effect as demonstrated by comparing Figure 5-25 to Figure 5-24.

Equivalent circuits can model the behavior of the input reflection coefficient antennas with frequency. This allows simulation and prediction of the antenna's S_{11} without using rigorous electromagnetic solvers. Equivalent circuit models were developed for the heatsink antennas of both orientations (FPNRE and FPPE). To make the models, the fins were replaced with lumped inductance and resistance. Lumped capacitors were used to model the capacitance between the heatsink fins. The circuit models are shown in Figure 5-26 and Figure 5-29 for the FPNRE and FPPE orientations, respectively. In both cases, the patch was modeled by a microstrip transmission line in addition to the 50- Ω transmission line and the quarter-wave transformer. However, two shunt capacitances and resistances (C_{slot} and R_{slot}) account for the radiation from the two slots of the patch which are included in the models of both orientations.

For the FPNRE orientation, the heatsink can be modeled by two capacitances (C_{fin1} and C_{fin3}) which are shunted to the center of the patch by a fin inductance, L_{fin2} , and a fin resistance, R_{fin2} . The center of the patch is a virtual ground, so a similar behavior is obtained by shunting the fin inductance and resistance to ground. The S_{11} and return loss of this model compared with those obtained by HFSS electromagnetic simulations at a fin height of 14 mm are shown in Figure 5-27 and Figure 5-28, respectively. By increasing the fin inductance, L_{fin} , which corresponds to an increase in fin height, the alternate resonant frequency is reduced; however, this has no effect on the primary resonance. This is the same behavior as shown in Figure 5-20 for the simulated and measured resonant frequencies of the FPNRE heatsink antenna versus fin height. The fin resistance is related to the diameter of the alternate resonant locus on the Smith chart. Increasing the fin resistance reduces the diameter of the alternate resonant locus and lowers the magnitude of the return loss at that frequency (closer to 0 dB) but has no effect on the primary resonant locus. Increasing the fin capacitance, however, reduces both the primary and

alternate resonant frequencies. Thus for this model to be accurate, an increase in fin height cannot lead to a significant increase in fin capacitance. It must also be noted that the capacitances are connected between the radiating slots even though the fins lie along the non-radiating slots. Along these non-radiating edges the current distribution goes through a phase change (Figure 5-22, left), and thus, a distributed model may be more appropriate. However, the same figure shows that the majority of the fields due to the alternate resonance (coming out of page) are located near the center of the patch along the length which is a virtual ground. This may explain how this simple lumped-element model is able to behave closely with the heatsink antenna.

For the FPPE orientation, the model is shown in Figure 5-29. In this case, the center fin has almost no effect on the antenna's S_{11} . Therefore, only lumped components due to the outer fins are included in the model which consists of the fin inductance, resistance and capacitance, L_{fin} , R_{fin} , and C_{fin} . Increasing the fin inductance (to represent an increase in fin height) with this model lowers both the alternate and primary resonant frequencies. With increasing inductance the alternate resonance decreases significantly at first and finally stops decreasing and remains constant with further increases in fin inductance. The primary resonant frequency continues to decrease with increasing fin inductance. This behavior is very similar to that shown in Figure 5-21 showing the simulated and measured primary and alternate resonant frequencies versus fin height. Unlike the FPNRE case, increasing the fin resistance, R_{fin} , reduces the diameter of *both* the alternate and primary resonant loci and lowers the magnitude of the return loss at those frequencies (closer to 0 dB).

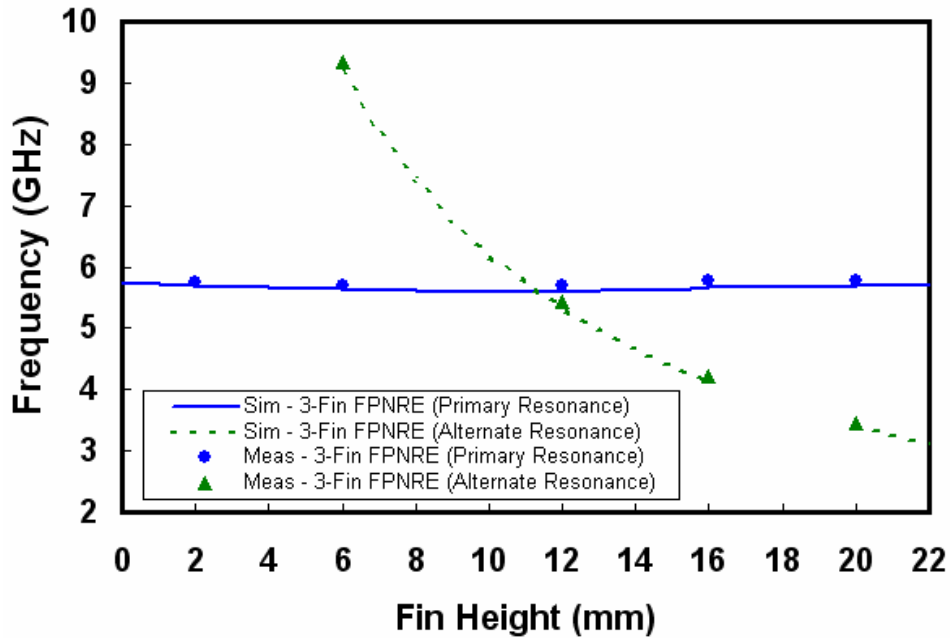


Figure 5-20. Measured and simulated resonant frequencies of the 3-finned heatsink antenna with fins parallel to the non-radiating edges (FPNRE)

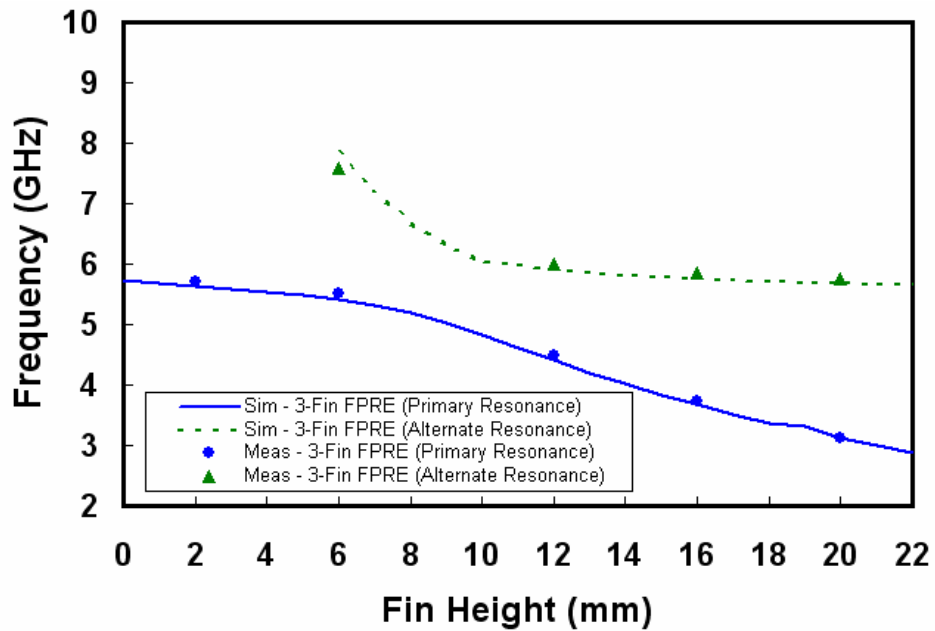


Figure 5-21. Measured and simulated resonant frequencies of the 3-finned heatsink antenna with fins parallel to the radiating edges (FPRE)

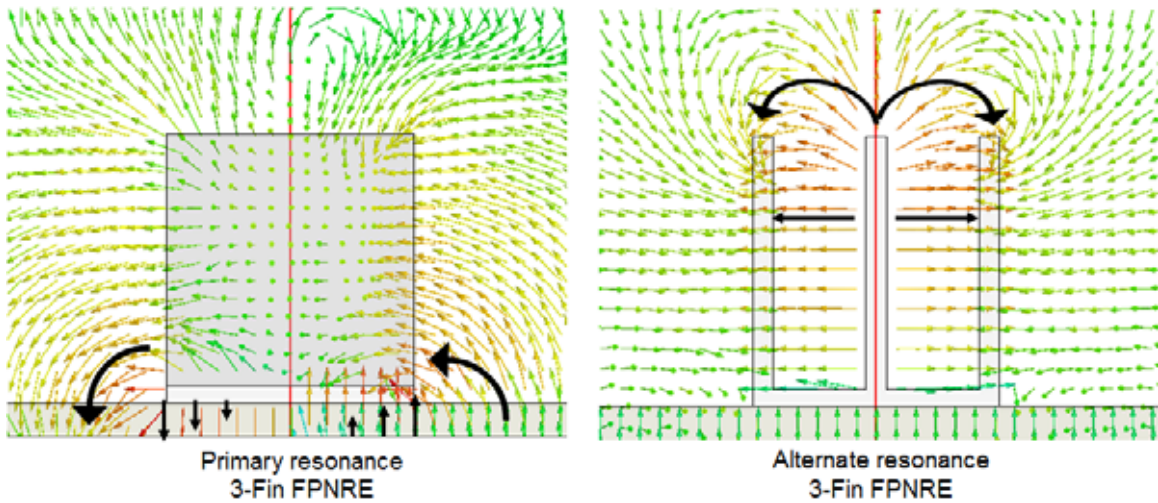


Figure 5-22. E-field vector plots showing primary (left, E-plane) and alternate resonances (right, H-plane) of 3-fin extruded-fin heatsink antenna with 12 mm fins parallel to the non-radiating edges (FPNRE)

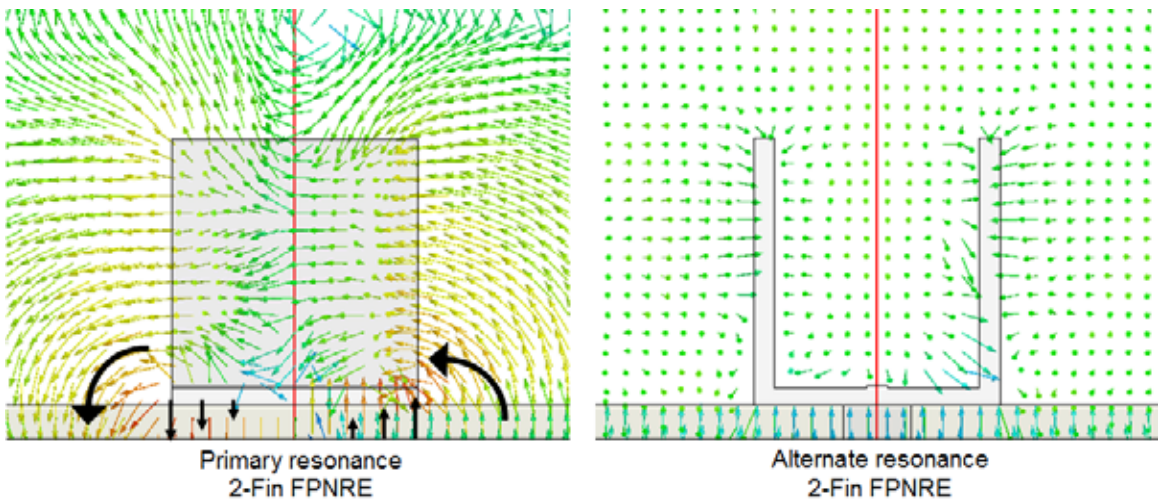


Figure 5-23. E-field vector plots showing primary (left, E-plane) and alternate resonances (right, H-plane) of 2-fin extruded-fin heatsink antenna with 12 mm fins parallel to the non-radiating edges (FPNRE)

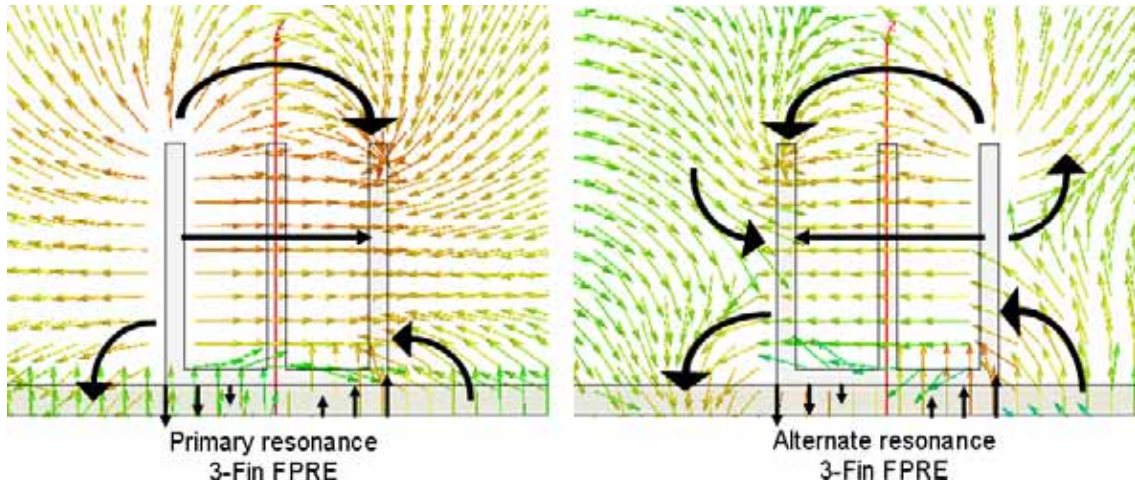


Figure 5-24. E-field vector plots showing primary (left, E-plane) and alternate resonances (right, E-plane) of 3-fin extruded-fin heatsink antenna with 12 mm fins parallel to the radiating edges (FPRE)

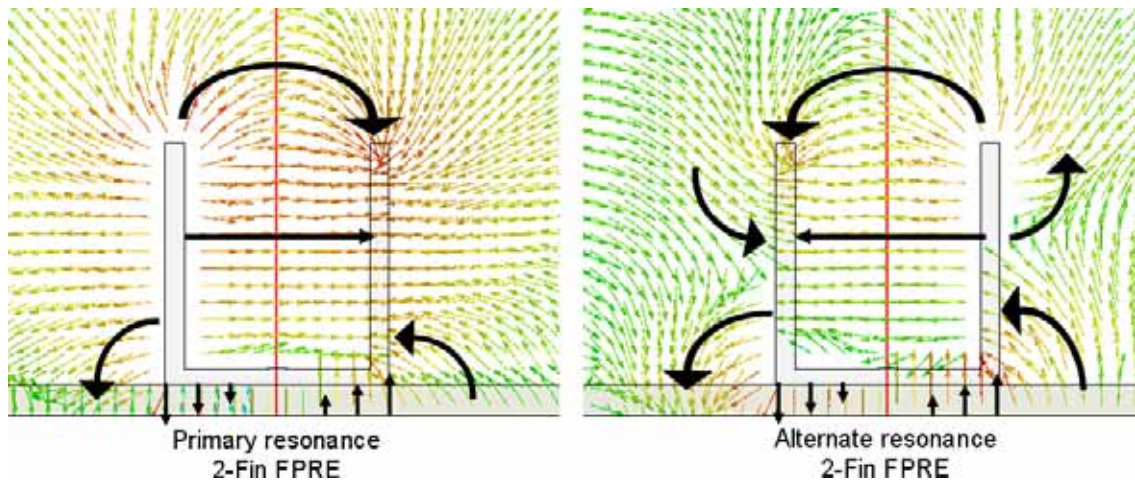


Figure 5-25. E-field vector plots showing primary (left, E-plane) and alternate resonances (right, E-plane) of 2-fin extruded-fin heatsink antenna with 12 mm fins parallel to the radiating edges (FPRE)

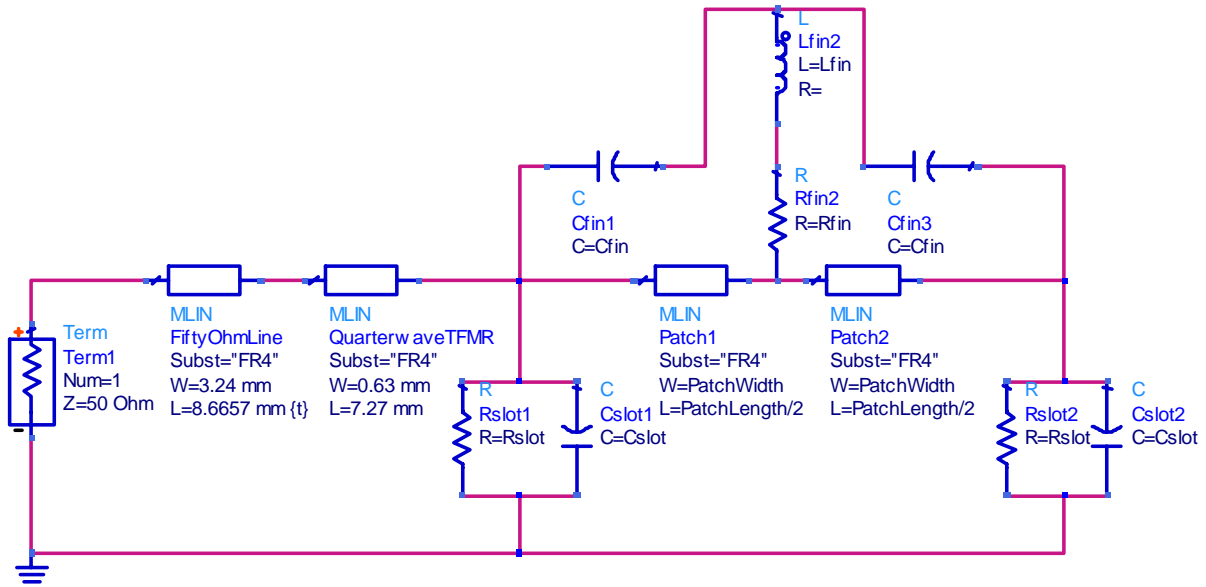


Figure 5-26. Equivalent circuit model of 3-fin extruded-fin heatsink antenna with fins parallel to the non-radiating edges (FPNRE)

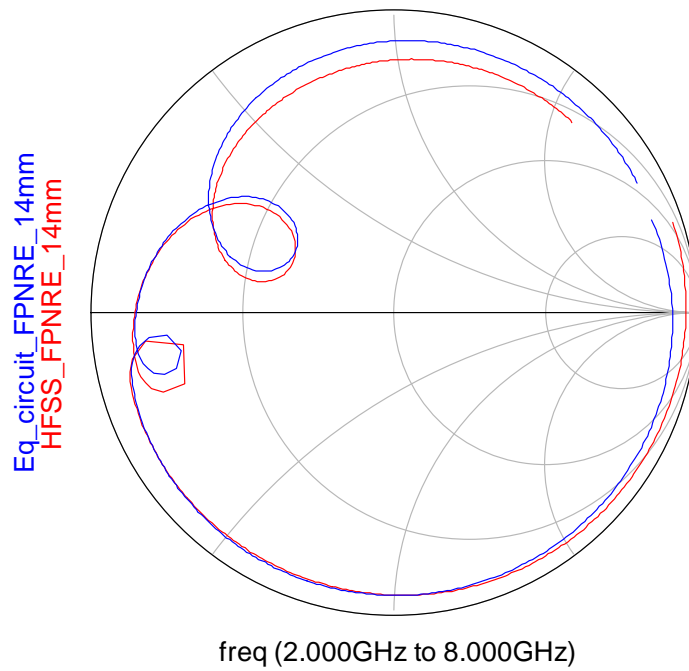


Figure 5-27. Comparison of S_{11} given by equivalent circuit model and HFSS electromagnetic solver of 3-fin extruded-fin heatsink antenna (FPNRE) with 14-mm fins

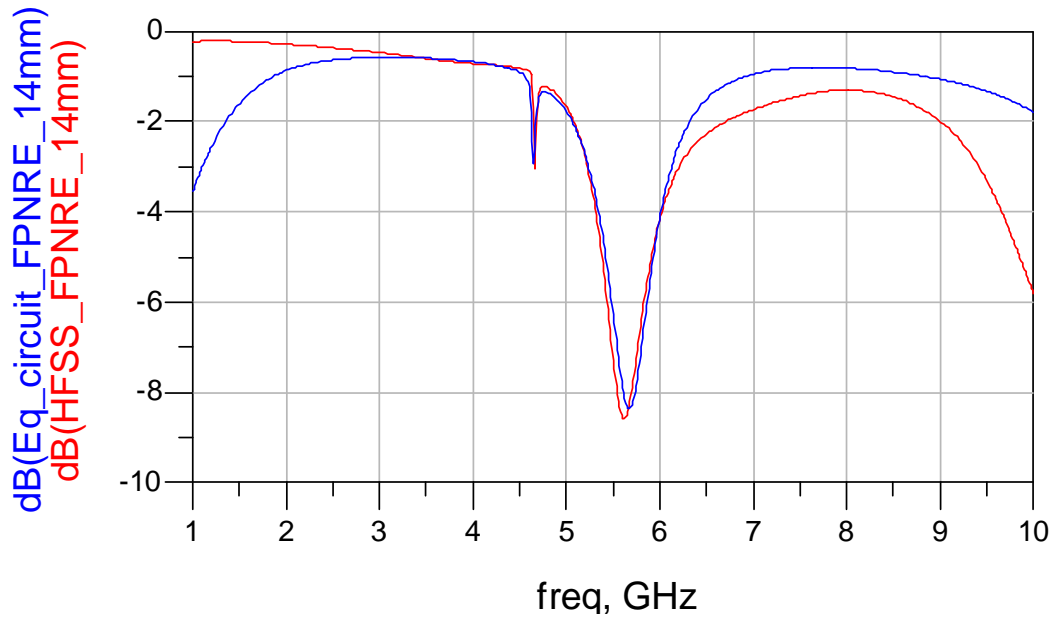


Figure 5-28. Comparison of return loss given by equivalent circuit model and HFSS electromagnetic solver of 3-fin extruded-fin heatsink antenna (FPNRE) with 14-mm fins

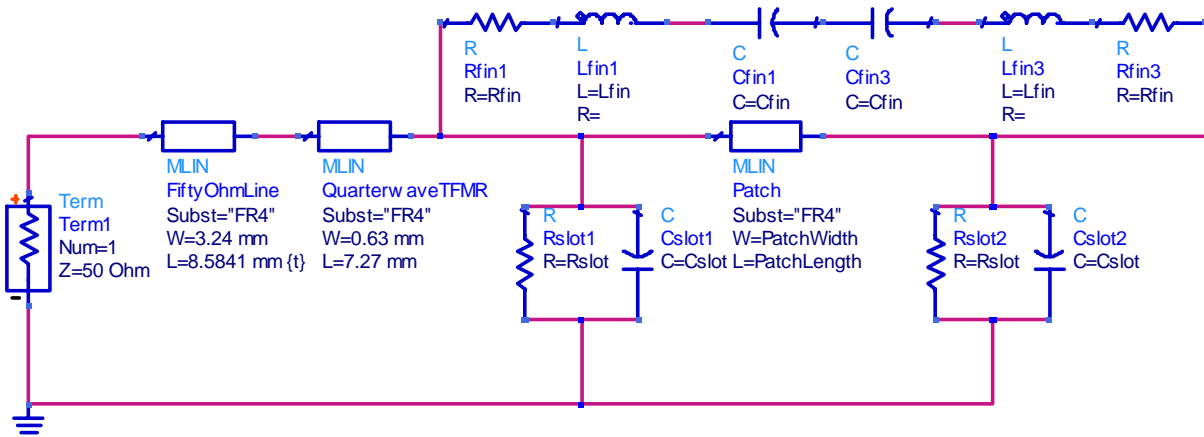


Figure 5-29. Equivalent circuit model of 3-fin extruded-fin heatsink antenna with fins parallel to the radiating edges (FPRE)

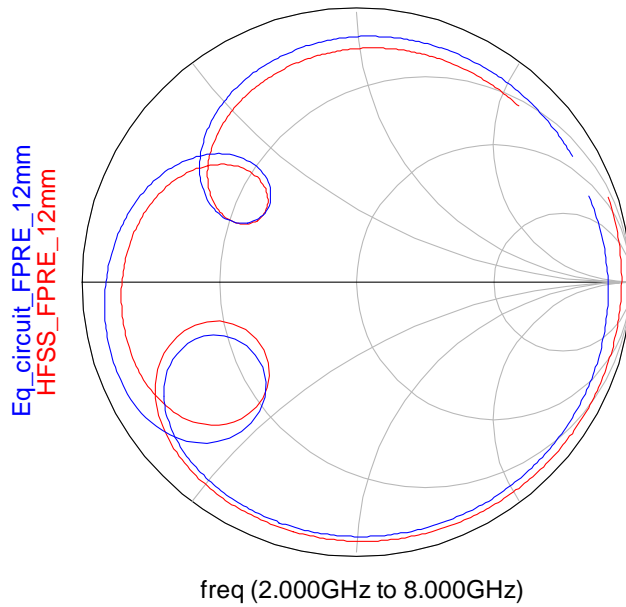


Figure 5-30. Comparison of S_{11} given by equivalent circuit model and HFSS electromagnetic solver of 3-fin extruded-fin heatsink antenna (FPRE) with 12-mm fins

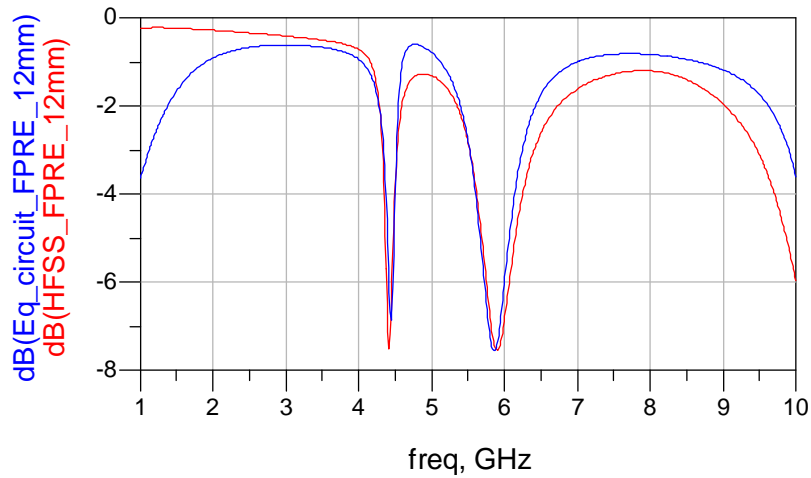


Figure 5-31. Comparison of return loss given by equivalent circuit model and HFSS electromagnetic solver of 3-fin extruded-fin heatsink antenna (FPRE) with-12 mm fins

5.3.2 Antenna Parameters and Radiation Patterns

Since the heatsink structure changes the resonant frequency of the antenna, and the antenna parameters (such as radiation efficiency, peak directivity, and peak gain) are dependent

upon frequency, this complicates the simulation and measurement plan and interpretation of the results. Namely, if the heatsink changes the resonant frequency, then the antenna parameters could be reported at the new resonant frequency since this would be the new operating frequency of the antenna. However, these results would not present a fair comparison since the results would be reported at two different operating frequencies (one for the non-radiating edges case and the second for the radiating edge case). In this case, not only is the fin height changing but also the frequency and other parameters such as the thickness of the substrate normalized to the wavelength. If the frequency is held constant and the antenna parameters are reported at this constant frequency, then the only variable is the fin height. This method yields a fairer comparison for the antenna parameters. Thus, the antenna parameters are reported first at a constant frequency of 5.80 GHz which is the approximate operating frequency of the basic patch antenna without the heatsink. Later the frequency-tracking results are reported for both the primary and alternate resonances.

The radiation efficiency versus fin height given at 5.8 GHz for the extruded-fin heatsink antennas is shown in Figure 5-32. The heatsink fin orientation has a significant effect on the radiation efficiency of the antenna. The efficiency increase for the non-radiating edge case is almost entirely monotonic with fin height. The heatsink having fins parallel to the non-radiating edge (or longitudinal to the patch current flow) allows the antenna to behave similar to a patch antenna while reducing dielectric losses. The result is that efficiency enhancement can be achieved even with a compact, low-profile heatsink. In contrast, the radiating edge case shows a decrease in efficiency up to a fin height of ~ 7 mm where it then abruptly increases at ~ 10 mm). At this fin height and above, the alternate resonance becomes the operating mode as its frequency has shifted near 5.8 GHz as shown in Figure 5-21. Thus, for a compact (low fin

height) heatsink design, the fins should be oriented along the non-radiating edges in order to achieve an improvement in radiation efficiency.

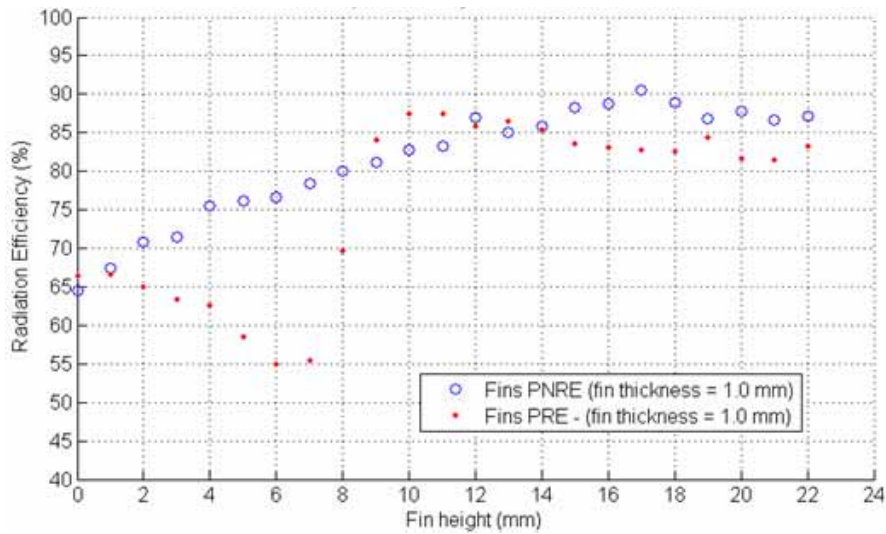


Figure 5-32. Simulated radiation efficiency vs. fin height for 3-finned antennas at 5.80 GHz

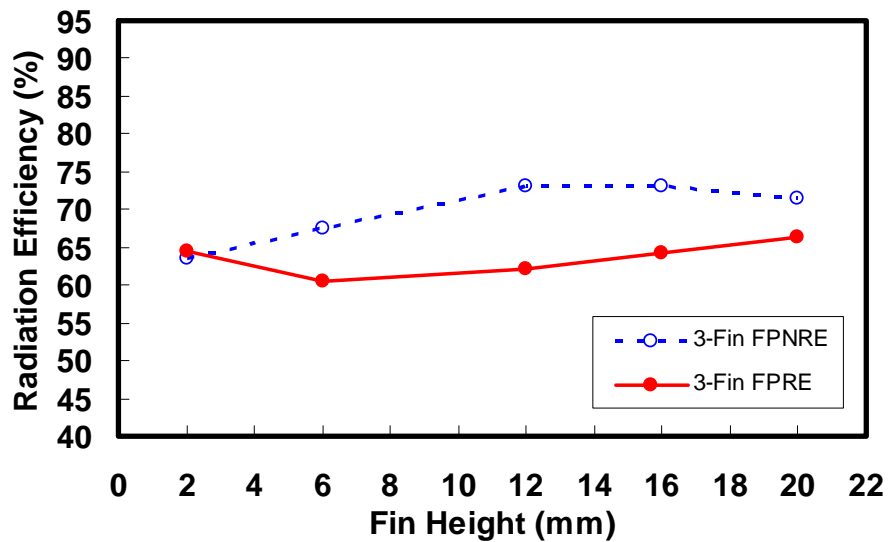


Figure 5-33. Measured radiation efficiency vs. fin height for 3-finned antennas at 5.80 GHz

The radiation efficiency was measured in a spherical near-field scanner at the Air Force Research Laboratory (AFRL). The results are shown in Figure 5-33. The results for the FPNRE case do show a monotonic increase in efficiency with increasing fin height though the efficiency

enhancement is greater in simulation. For the FPRE case, the measurements do show the initial decrease in efficiency from 2 to 6 mm fins. Above 6 mm, the measurements also show an increase in efficiency, however, the increase is not a discontinuous jump in efficiency as in simulation. The discrepancies may be due to differences in measured return loss since the measured efficiency calculation requires the removal of mismatch losses. Also, at the larger fin heights in the FPRE case, there is significant end-fire and backside radiation (Figure 5-38), thus the measurements dependent on the mounting of the antenna.

The peak directivity of the 3-finned heatsink antennas versus fin height and orientation are shown in Figure 5-34 and Figure 5-35 in simulation and measurement, respectively. The trend of the measured data versus fin height matches well with the simulation. Again, the heatsink fin orientation becomes an important factor. Notice for the radiating edge (FPRE) case, the peak directivity shows a significant dependence on the fin height both increasing and decreasing dramatically. While the directivity in the non-radiating edge (FPNRE) case also changes with fin height, this change is relatively small compared with that of the radiating edge case. For the non-radiating edge case, the fins are parallel to the direction of current on the patch antenna (Figure 5-36). Therefore, the radiation pattern is very similar to that of the patch antenna for all fin heights shown having a single broadside lobe. The 3-D far-field radiation patterns for the non-radiating edge case at various fin heights are shown in Figure 5-37. However, for the radiating edge case, the fins are transverse to the current flow on the patch which prohibits longitudinal fin currents. As the fin height increases in this case, significant vertical currents begin to appear on the outer fins (Figure 5-36). This changes the radiation pattern significantly (as shown in Figure 5-38) and thus also changes the directivity.

The vertical currents on the fins in the radiating edge case act like an array of monopoles spaced $\lambda/2$ apart and phase excitation difference of 180 degrees. For an antenna array, the antenna pattern is obtained by pattern multiplication which is the product of the pattern of a single element (single antenna) and the array factor. The 3-D far-zone array factor (AF) can be determined from [Bal]

$$AF = \sum_{n=1}^N a_n e^{j(n-1)\psi} \quad (5-1)$$

where

$$\psi = kd \cos(\gamma) + \beta, \quad (5-2)$$

N is the total number of elements in the array, k is the propagation constant ($k = 2\pi/\lambda$), d is the physical separation between the elements, a_n is the amplitude excitation of each element, β is the difference in phase excitation between the elements, and γ is the angle between the axis containing the linear array of elements and the radial vector from the origin to the observation point. The expression for γ depends on the coordinate system and the axis which contains the linear array of elements. For the coordinate system shown in Figure 5-45 with the array elements along the x-axis,

$$\gamma = \cos^{-1}(\sin(\theta)\cos(\phi)) \quad (5-3)$$

where θ is the elevation angle and ϕ is the azimuth angle [Bal].

The resulting 3-D array factor for two elements spaced $\lambda/2$ apart with a phase excitation difference of 180 degrees and each element having equal excitation amplitude is shown in Figure 5-46. The 3-D single-element pattern of a dipole antenna is shown in Figure 5-47. A dipole is used here instead of a monopole antenna pattern due to the finite and small ground plane. By multiplying the array factor in Figure 5-46 by the single-element pattern in Figure 5-47, the total

antenna array pattern is obtained (Figure 5-48). The resulting radiation pattern is consistent with Figure 5-38. The antenna radiation patterns for the 3-finned heatsink have sidelobes similar to those in Figure 5-48 and along the same axis (the axis containing the array of elements).

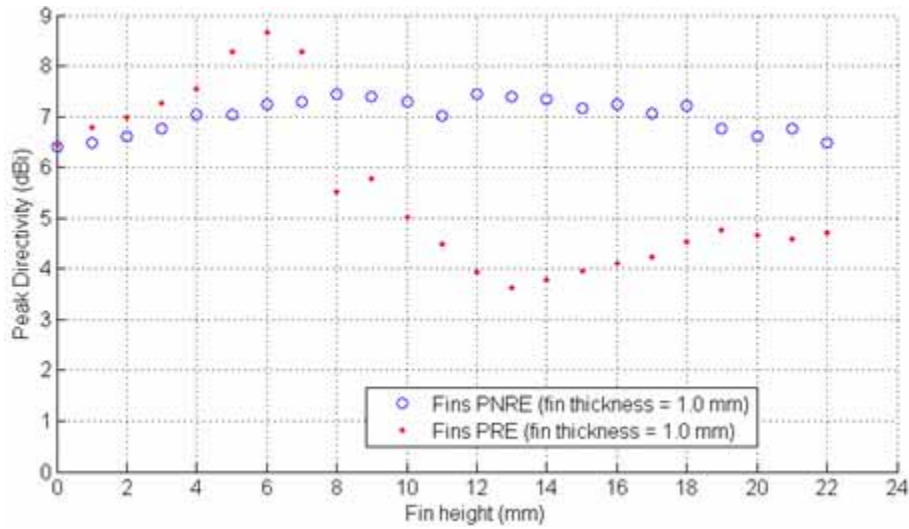


Figure 5-34. Simulated peak directivity vs. fin height for 3-finned antennas at 5.80 GHz

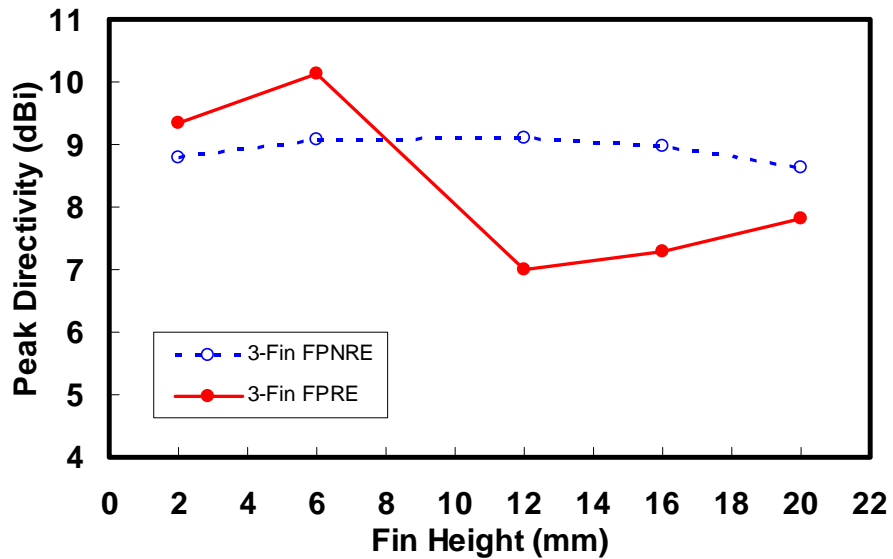


Figure 5-35. Measured peak directivity vs. fin height for 3-finned antennas at 5.80 GHz

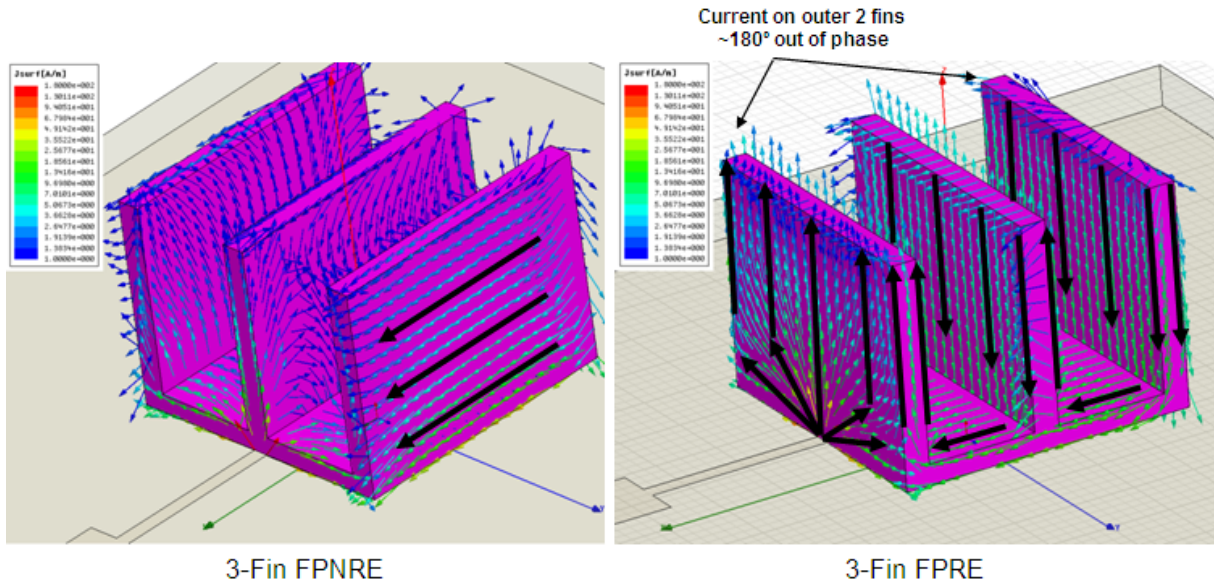


Figure 5-36. Surface currents on the heatsink fins for the 3-fin FPNRE case (left) and the 3-fin FPRE case (right)

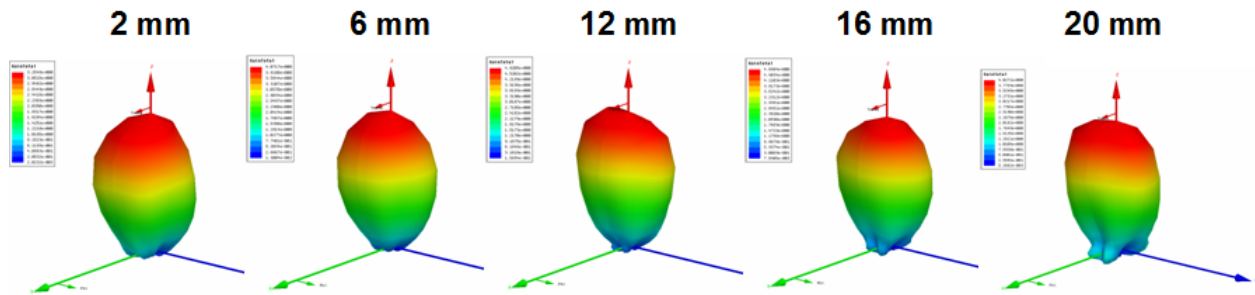


Figure 5-37. Simulated 3-D radiation patterns for fin height sweep of 3-finned antenna with fins parallel to the non-radiating edges (FPNRE) at 5.80 GHz

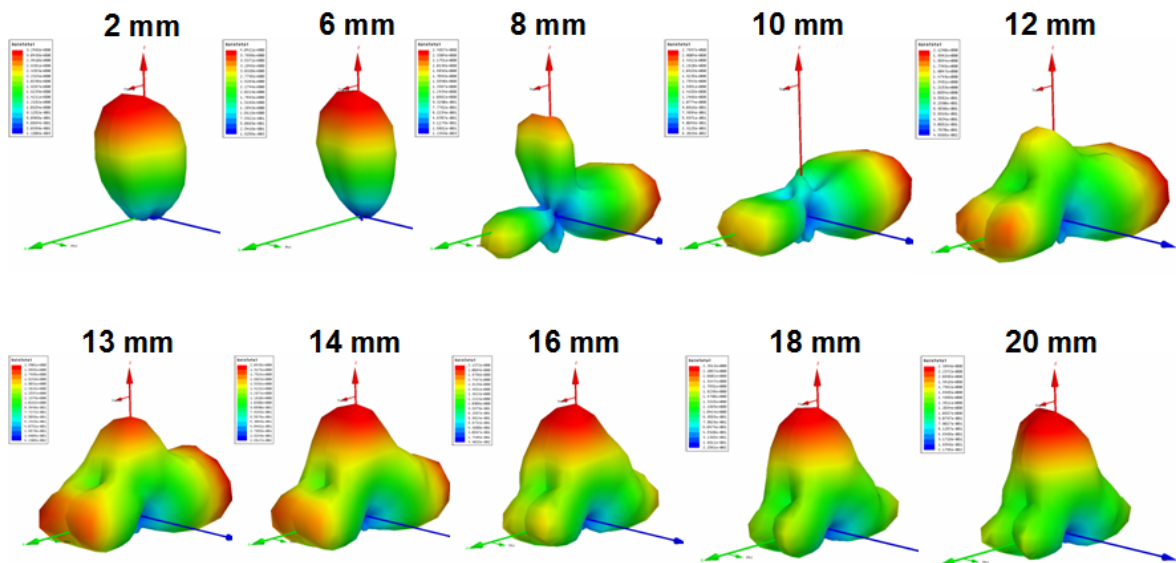


Figure 5-38. Simulated 3-D radiation patterns for fin height sweep of 3-finned antenna with fins parallel to the radiating edges (FPRE) at 5.80 GHz

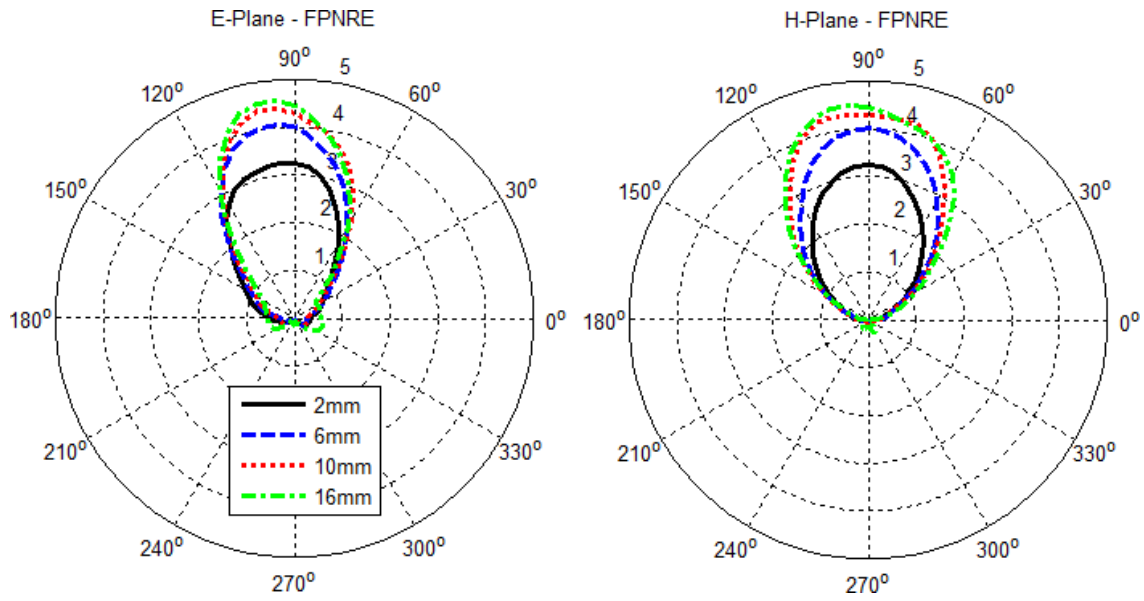


Figure 5-39. Simulated 2-D gain patterns (linear scale) of extruded-fin heatsink antenna with fins parallel to the non-radiating edges (FPNRE) at various fin heights at 5.80 GHz

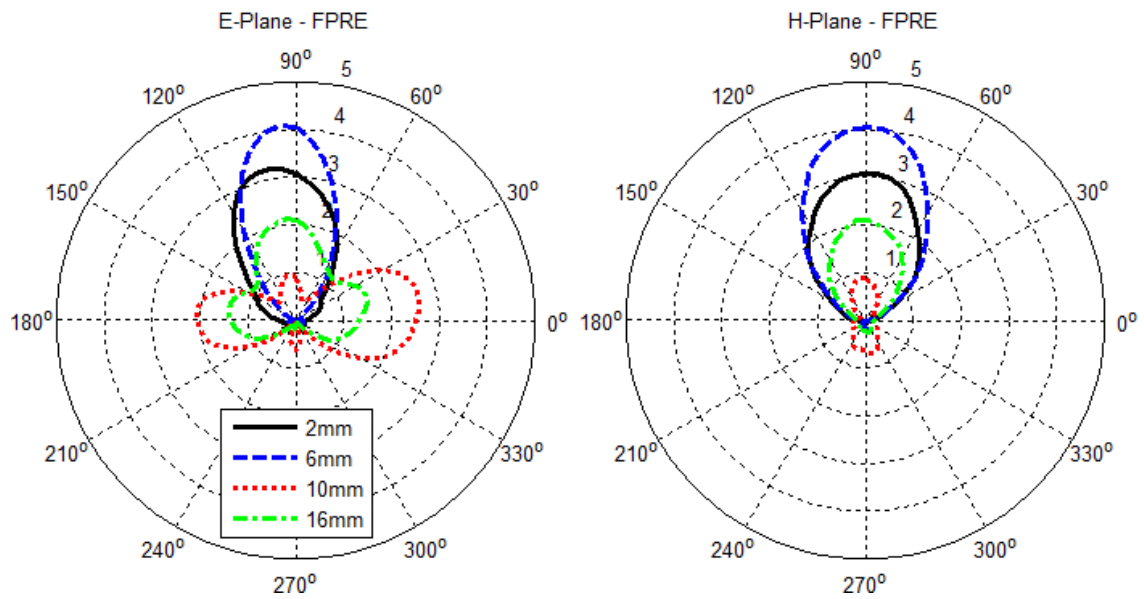


Figure 5-40. Simulated 2-D gain patterns (linear scale) of extruded-fin heatsink antenna with fins parallel to the radiating edges (FPRE) at various fin heights at 5.80 GHz

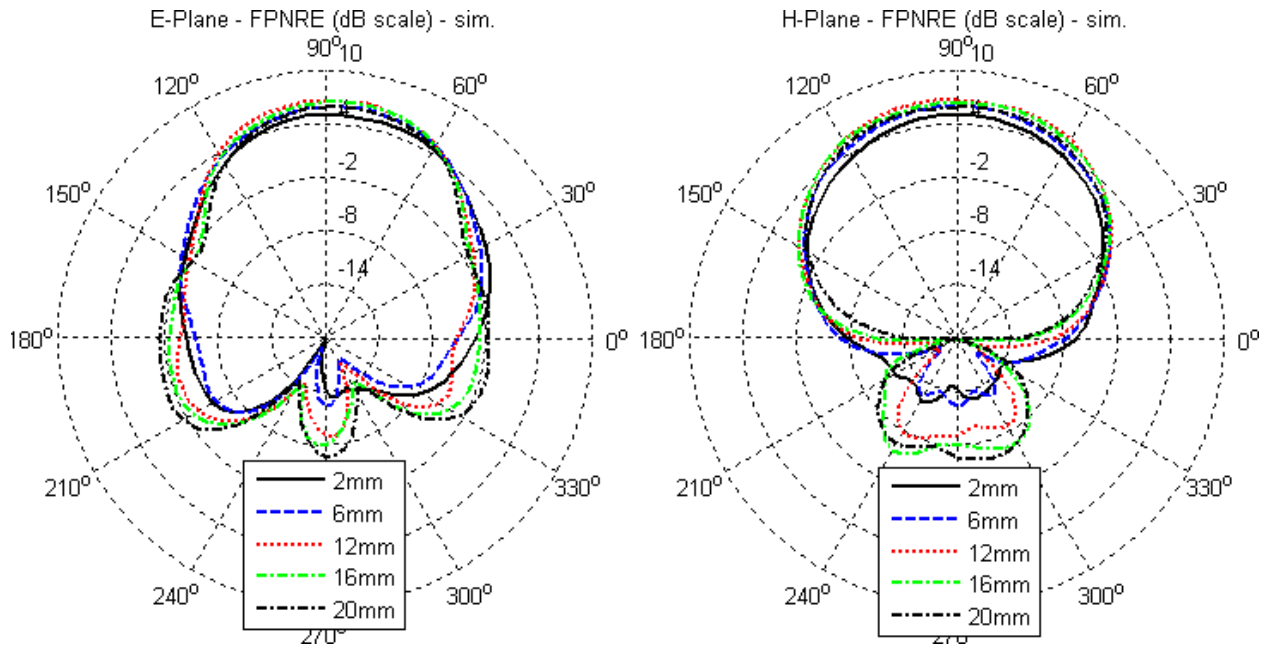


Figure 5-41. Simulated 2-D gain patterns (dB scale) of extruded-fin heatsink antenna with fins parallel to the non-radiating edges (FPNRE) at various fin heights at 5.80 GHz

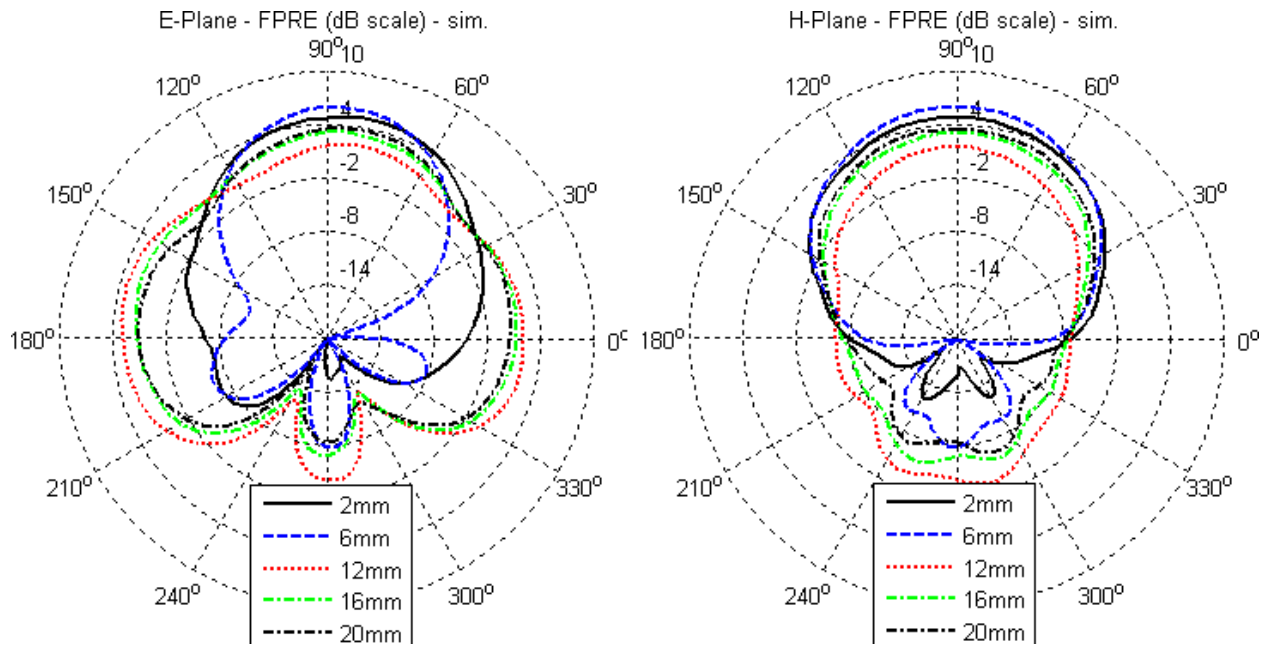


Figure 5-42. Simulated 2-D gain patterns (dB scale) of extruded-fin heatsink antenna with fins parallel to the radiating edges (FPRE) at various fin heights at 5.80 GHz

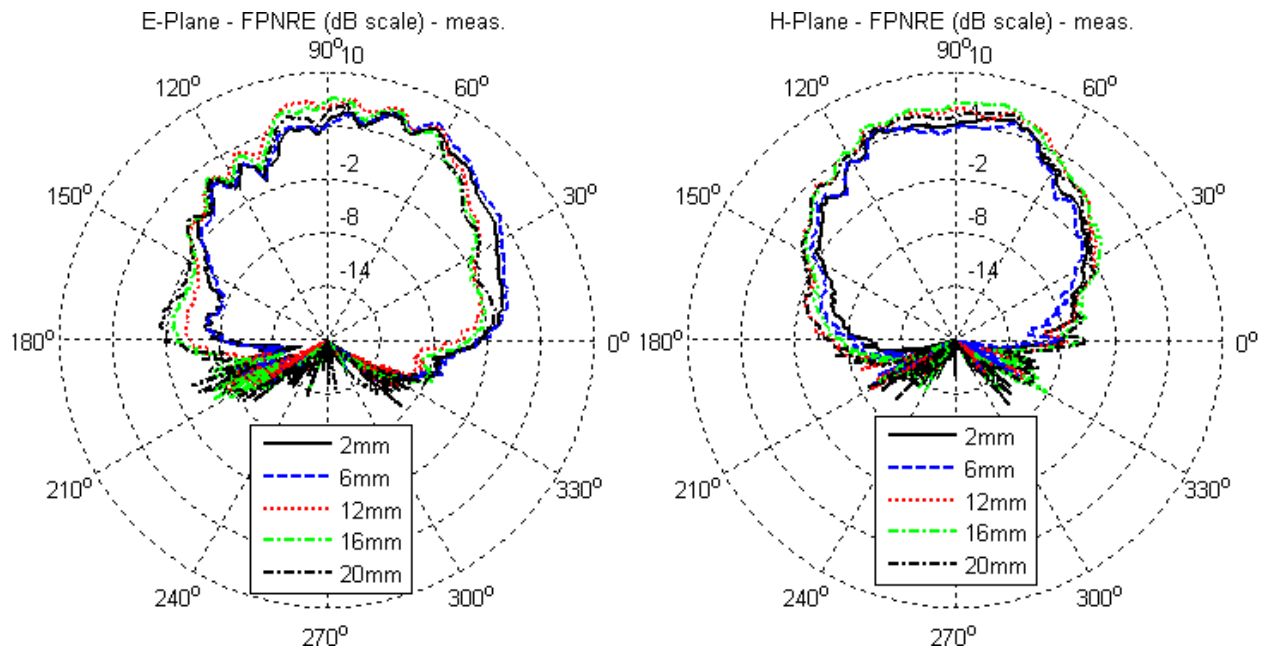


Figure 5-43. Measured 2-D gain patterns (dB scale) of extruded-fin heatsink antenna with fins parallel to the non-radiating edges (FPNRE) at various fin heights at 5.80 GHz

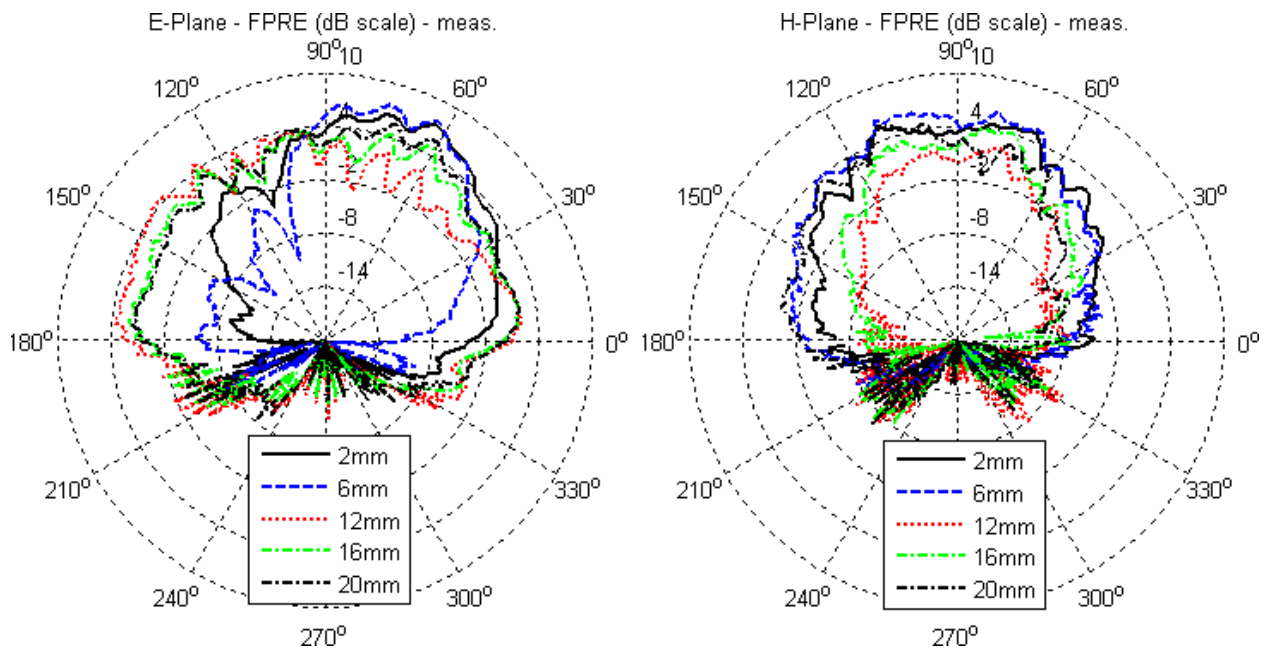


Figure 5-44. Measured 2-D gain patterns (dB scale) of extruded-fin heatsink antenna with fins parallel to the radiating edges (FPRE) at various fin heights at 5.80 GHz

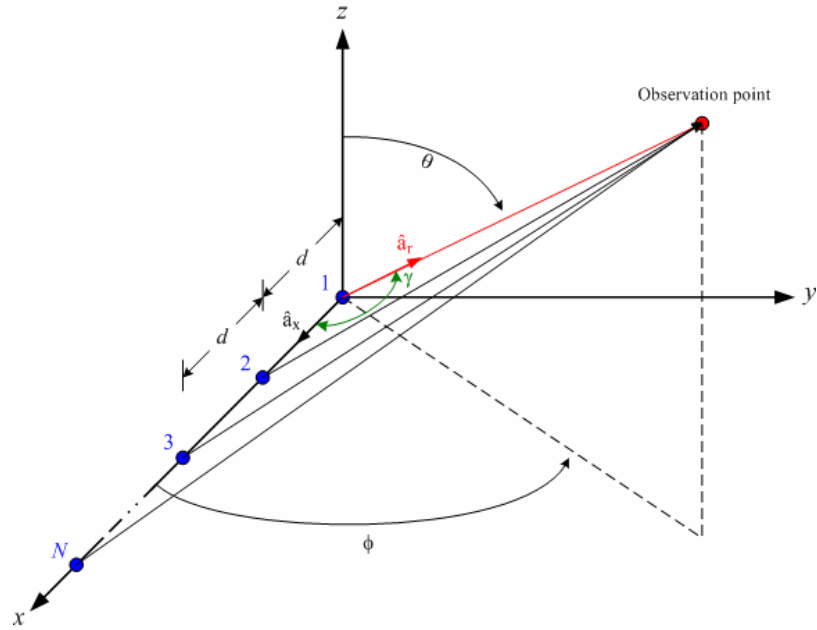


Figure 5-45. Coordinate system for 3-D far-zone antenna array factor [Bal]

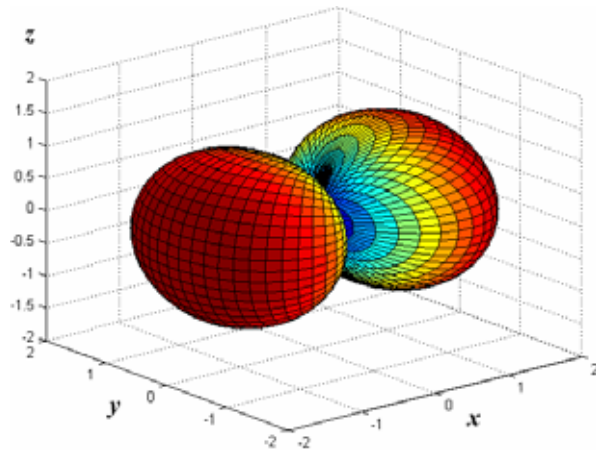


Figure 5-46. 3-D far-zone array factor for 2 elements spaced $\lambda/2$ apart along the x-axis with an excitation phase difference of 180 degrees

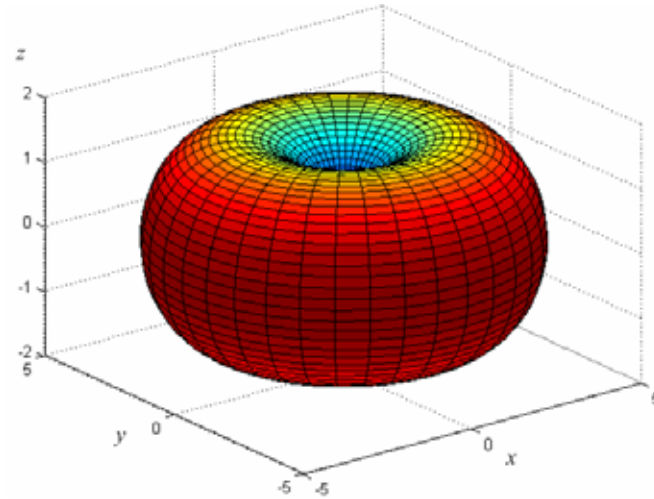


Figure 5-47. 3-D far-field dipole pattern

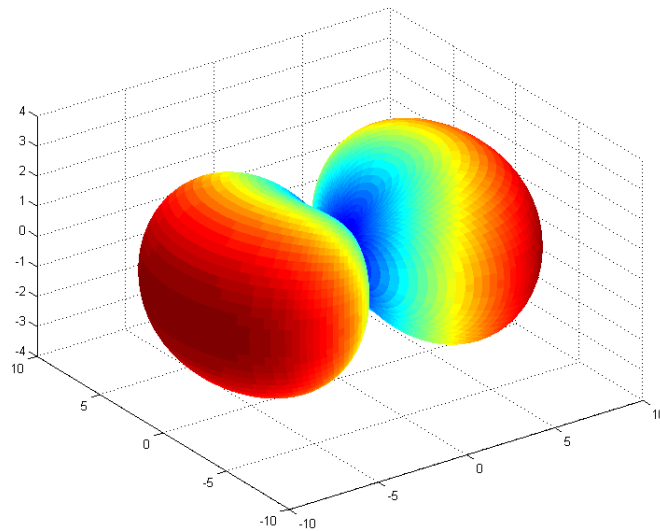


Figure 5-48. Radiation pattern of two-element dipole array resulting from pattern multiplication of array factor and single element patterns

Referring back at the FPRE case in Figure 5-34, the directivity varies significantly with fin height. From 2 mm to 6 mm, the radiation pattern has a broadside lobe only and this broadside lobe becomes more focused with increasing with fin height up to 6 mm. As the fin height increases further, the fins begin acting like an array of monopole antennas. This generates the two end-fire sidelobes discussed previously reducing the directivity. Only the two sidelobes are present (no broadside lobe) at fin heights of 9 mm and 10 mm. The broadside lobe starts to

return at about 11 or 12 mm. The directivity decreases until it reaches a minimum of at a fin height of 13 mm. At this point the broadside lobe and the two end-fire lobes have relatively the same magnitude making the radiating pattern less focused. For fin heights of 14 mm or greater, the broadside lobe becomes more focused while the two end-fire lobes recede, thus, increasing the directivity.

From the directivity results, the heatsink antenna designer has control of the antenna's directivity by using a specific fin height and orientation. If high directivity is desired, then the fins should be oriented parallel the radiating edges of the patch. Alternately, if the heatsink antenna designer is more concerned with the thermal performance of the heatsink, then the fins should be oriented parallel to the non-radiating edges. In this manner the thermal performance of the heatsink can be optimized while having a minimal effect on the antenna's peak directivity. This relative independence between fin height and directivity can simplify the heatsink antenna design considerably.

The simulated and measured peak gain versus fin height for the 5.8 GHz 3-finned heatsink antennas are shown in Figure 5-49 and Figure 5-50, respectively. Similar results for the peak gain are obtained as with the peak directivity since the gain is the product of the directivity and the radiation efficiency. However, the gain for both orientations in simulation is nearly equivalent up to a fin height of 6 mm. The directivity of the FPPE case is greater than that of the FPNRE case up to 6 mm but the radiation efficiency of the radiating edge case is reduced compared with the opposite orientation. Therefore, the peak gains of the two orientations up to 6 mm are nearly equivalent. Thus, the importance of the fin orientation is substantiated again by the gain. The trend of the peak gain versus fin height in measurement matches well with simulation.

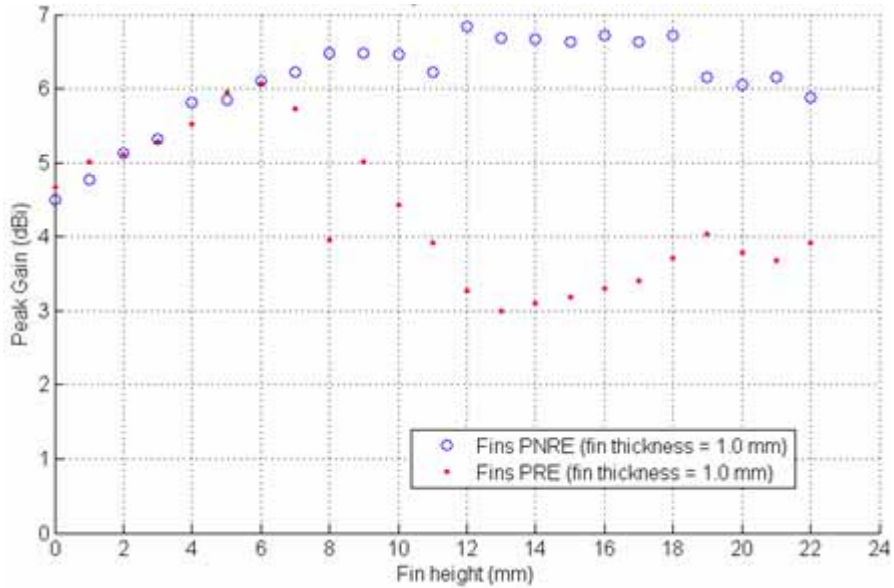


Figure 5-49. Simulated peak gain vs. fin height for 3-finned antennas at 5.80 GHz

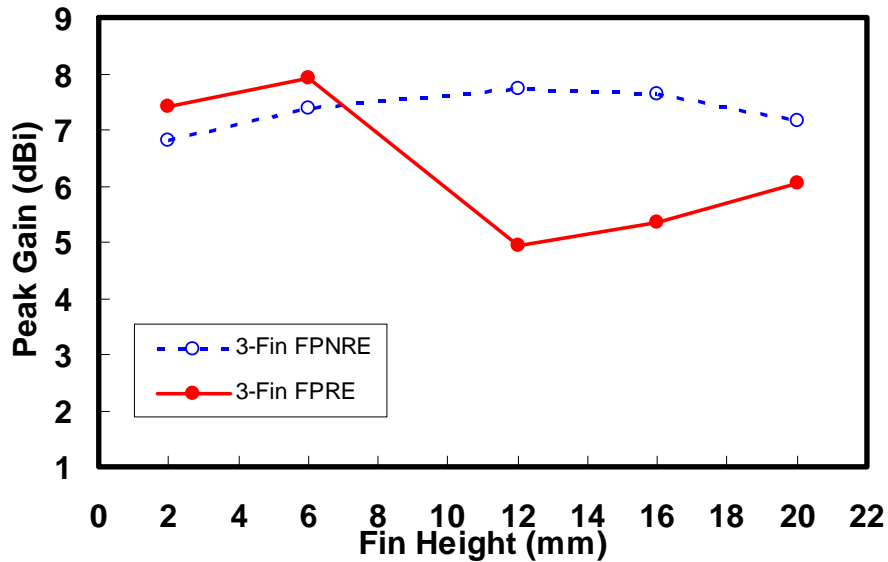


Figure 5-50. Measured peak gain vs. fin height for 3-finned antennas at 5.80 GHz

The antenna parameters given thus far were reported at a constant frequency of 5.80 GHz. Since the resonant frequency changes with fin height, it is also important to understand how the trend of the antenna parameters versus fin height for the primary and alternate resonances. Therefore, Figure 5-51 through Figure 5-56 compare the antenna parameters at both

the primary and alternate resonances as well as at 5.80 GHz. The frequencies associated with the primary and alternate resonances are given in Table 5-3 and also shown in Figure 5-20 and Figure 5-21.

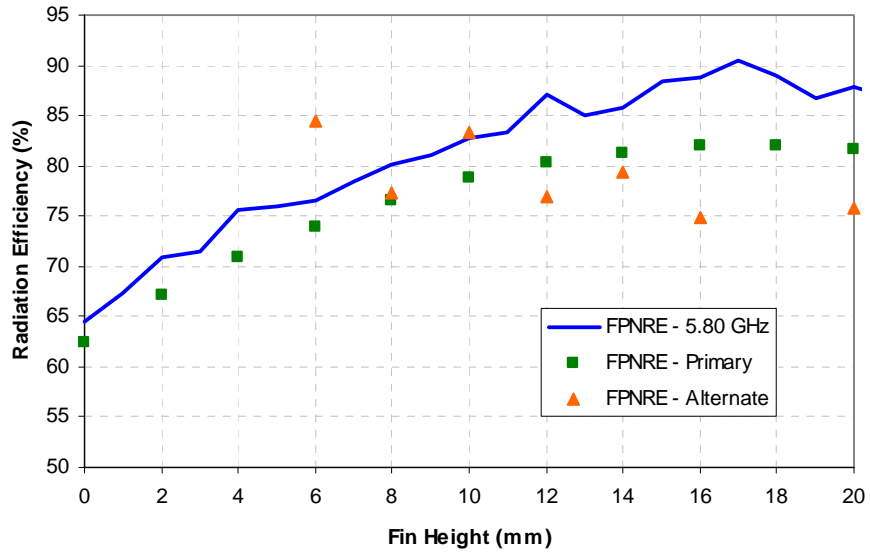


Figure 5-51. Frequency-tracking comparison of simulated radiation efficiency vs. fin height for 3-fin FPNRE heatsink antenna

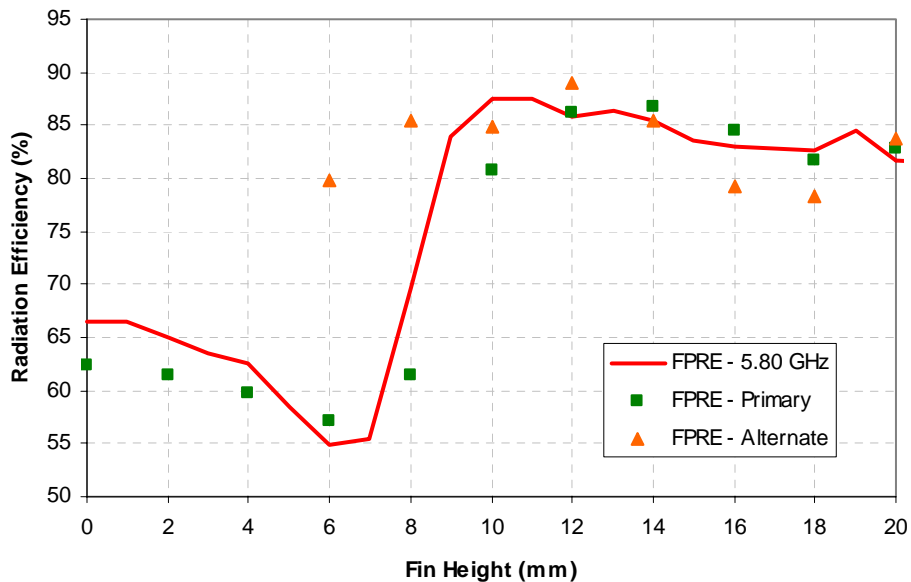


Figure 5-52. Frequency-tracking comparison of simulated radiation efficiency vs. fin height for 3-fin FPRE heatsink antenna

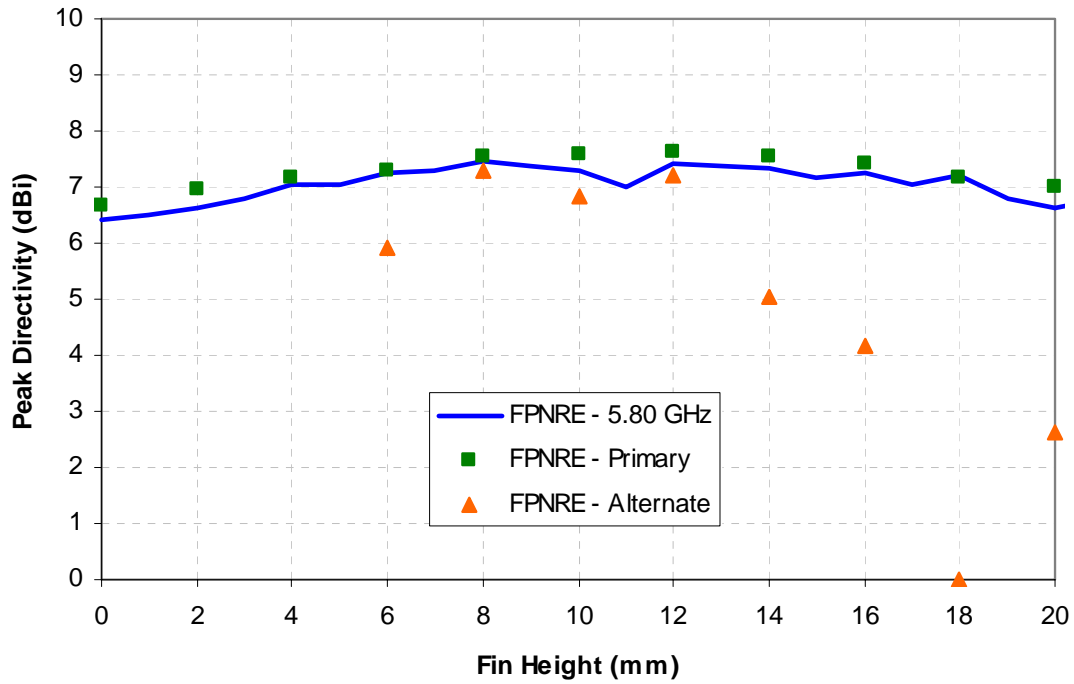


Figure 5-53. Frequency-tracking comparison of simulated peak directivity vs. fin height for 3-fin FPNRE heatsink antenna

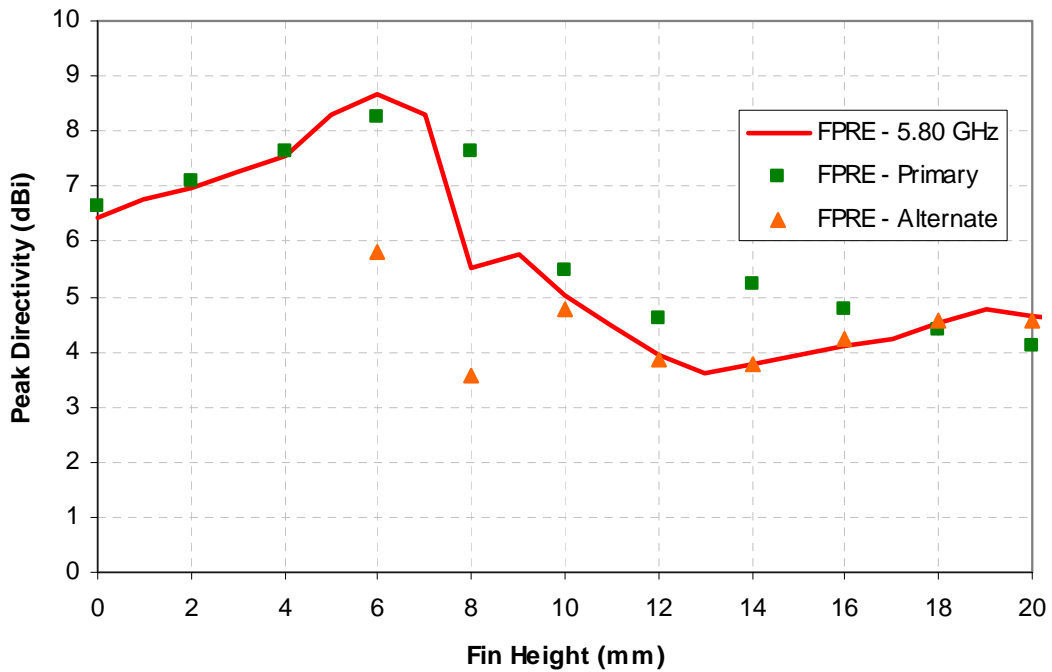


Figure 5-54. Frequency-tracking comparison of simulated peak directivity vs. fin height for 3-fin FPRE heatsink antenna

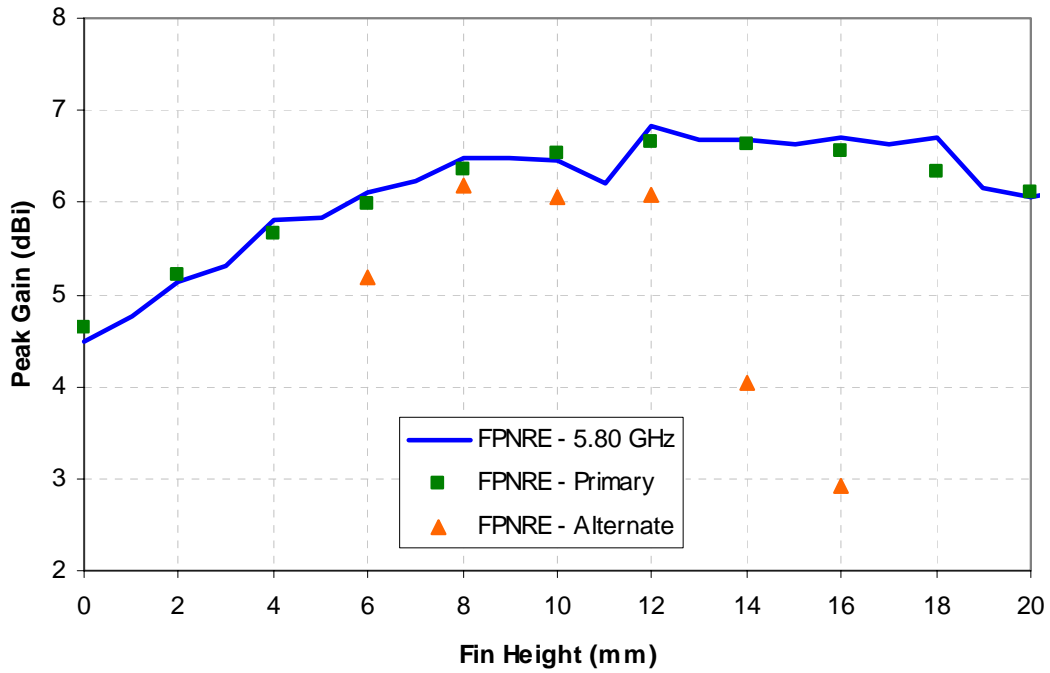


Figure 5-55. Frequency-tracking comparison of simulated peak gain vs. fin height for 3-fin FPNRE heatsink antenna

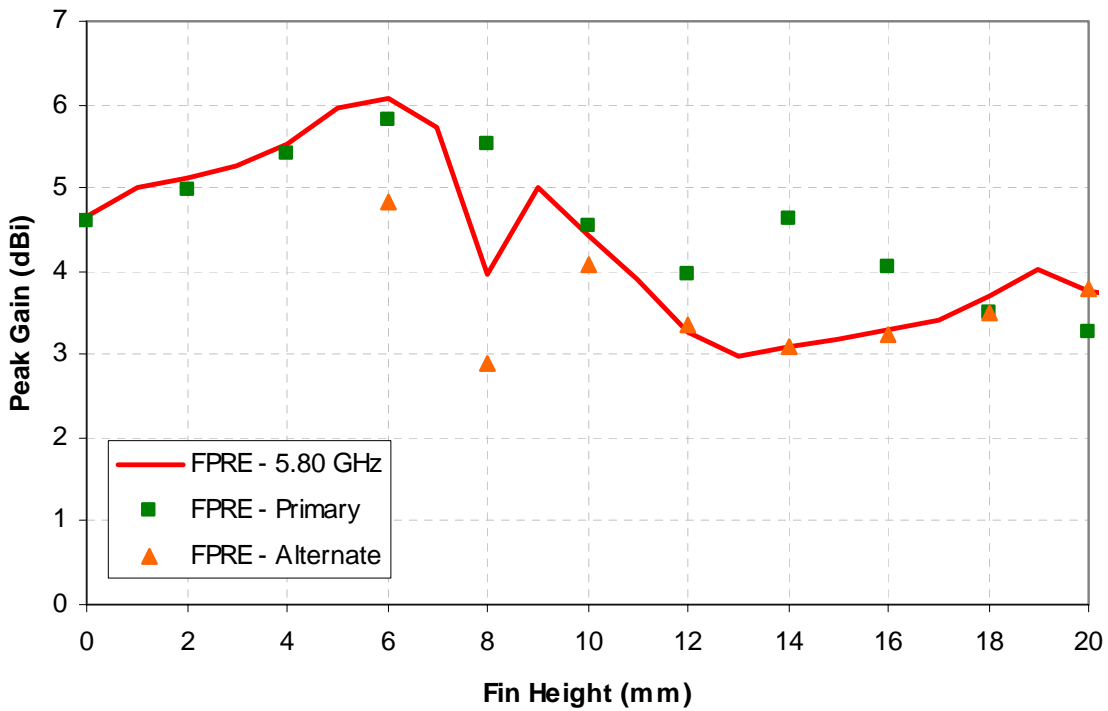


Figure 5-56. Frequency-tracking comparison of simulated peak gain vs. fin height for 3-fin FPRE heatsink antenna

Table 5-3. Primary and alternate resonant frequencies associated used for frequency-tracking heatsink antenna parameters

Fin height (mm)	FPNRE primary resonant frequency (GHz)	FPNRE alternate resonant frequency (GHz)	FPRE primary resonant frequency (GHz)	FPRE alternate resonant frequency (GHz)
0	5.736	N/A	5.725	N/A
2	5.691	N/A	5.624	N/A
4	5.657	N/A	5.340	N/A
6	5.635	9.190	5.421	7.840
8	5.612	7.412	5.196	6.704
10	5.601	6.186	4.825	6.051
12	5.601	5.343	4.420	5.905
14	5.612	4.656	4.015	5.800
16	5.657	4.150	3.678	5.747
18	5.680	N/A	3.374	5.714
20	5.702	3.419	3.115	5.691

Notice the discontinuous jump in efficiency in Figure 5-52 for the FPRE case. This increase in efficiency occurs at both 5.80 GHz and at the primary resonance of the antenna; however, the efficiency of the alternate resonance is already at the higher efficiency level. As shown in the figure, the jump in efficiency occurs between the fin heights of 8 mm and 10 mm. In order to see what happens to cause such a dramatic shift in efficiency, the E-field vector and magnitude plots are shown in an E-plane cross-section for 6mm, 8 mm, and 10 mm FPRE cases (Figure 5-57). The E-field directions are similar in all cases, however, the magnitude plot shows much more confinement of the E-field underneath the patch and inside the lossy substrate at 10 mm fin height. At 10 mm the E-fields are much less confined and the dielectric losses are reduced resulting in the efficiency increase. At 10 mm, the radiation pattern for the primary resonance goes through a dramatic change from a single broadside lobe to two end-fire lobes (Figure 5-59).

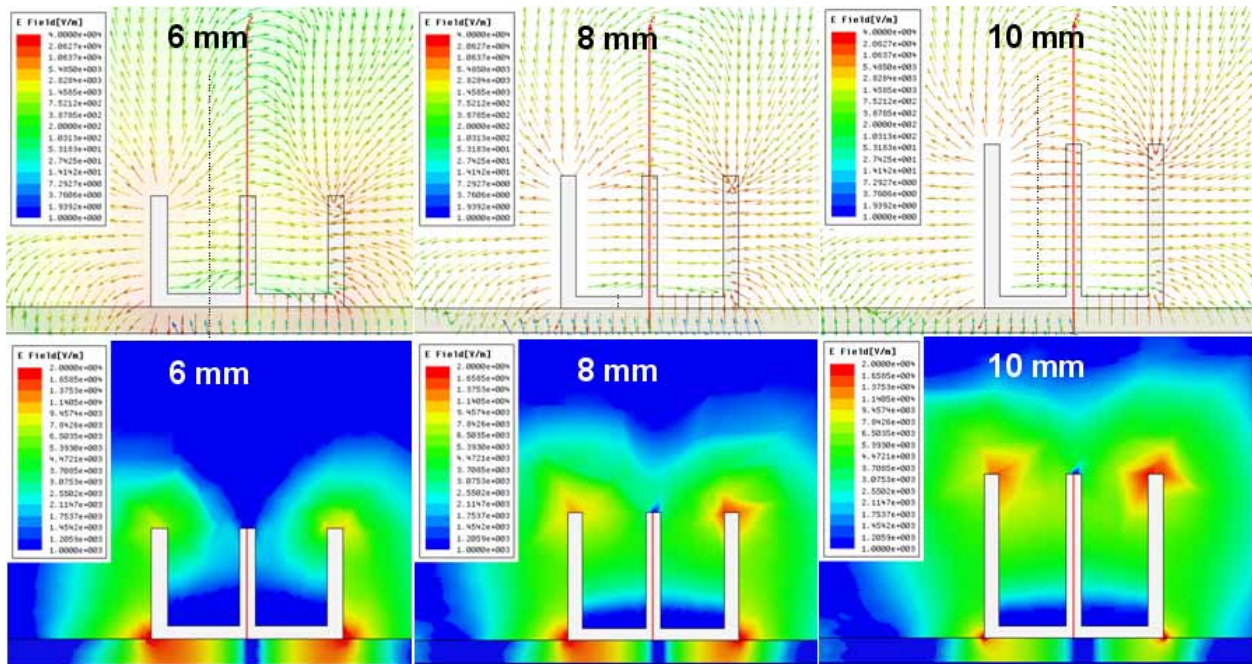
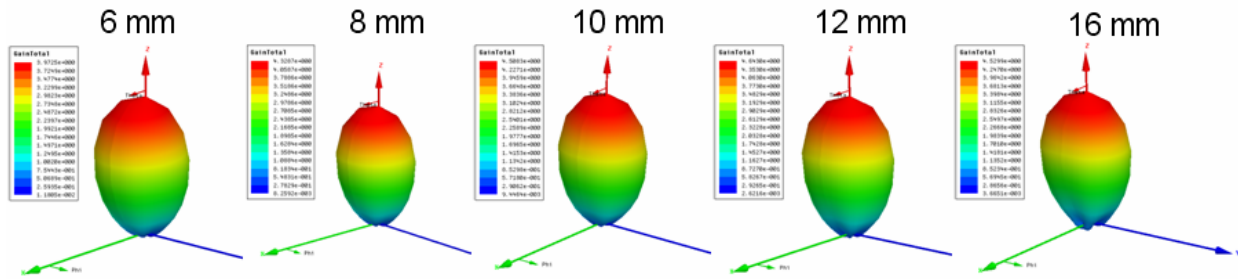


Figure 5-57. E-field vector (top) and magnitude (bottom) plots of FPRES heatsink antenna at 8 mm and 10 mm fin heights given at the respective primary resonances

The radiation patterns were given earlier in Figure 5-37 and Figure 5-38 for the FPNRE and FPRES orientations, respectively. However, these patterns were given at a constant frequency of 5.80 GHz for each fin height. Since the resonance frequency does not stay constant with fin height, it may also be important to understand how the radiation pattern changes with the primary and alternate resonances across the fin height range. The 3-D simulated patterns at the primary and alternate resonances for the FPNRE case and the FPRES case are shown in Figure 5-58 and Figure 5-59, respectively.

Primary resonance patterns:



Alternate resonance patterns:

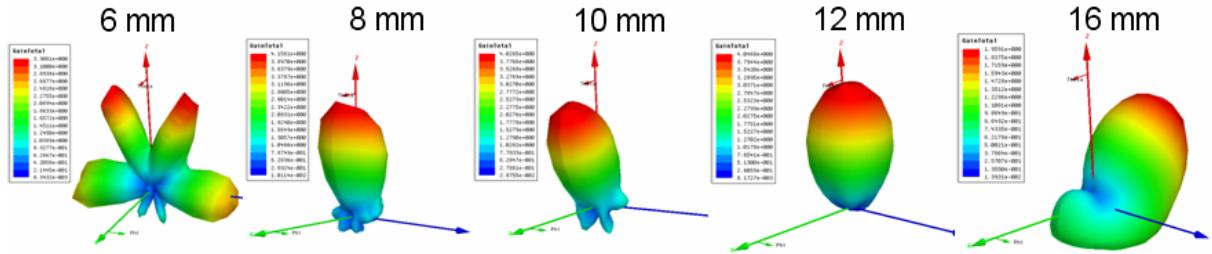
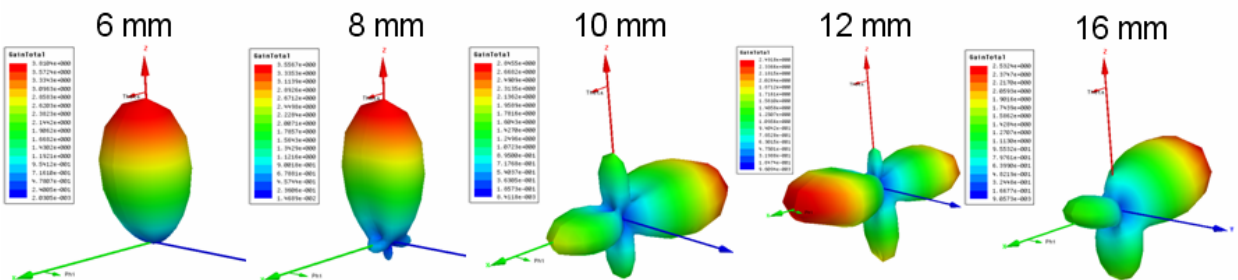


Figure 5-58. Simulated 3-D radiation patterns for fin height sweep of 3-finned extruded-fin heatsink antenna (FPNRE case) at both the primary and alternate resonances

Primary resonance patterns:



Alternate resonance patterns:

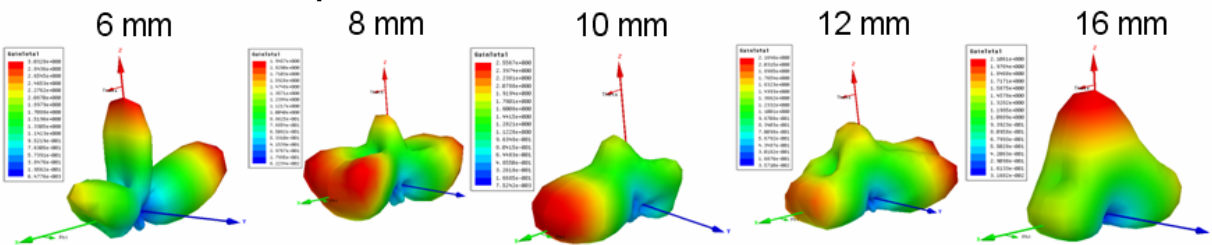


Figure 5-59. Simulated 3-D radiation patterns for fin height sweep of 3-finned extruded-fin heatsink antenna (FPRE case) at both the primary and alternate resonances

5.3.3 Fin Thickness Sweep

The fin thickness was also varied in simulations to determine its effect on the antenna parameters. Three fin thicknesses (1.0 mm, 1.6 mm, and 2.2 mm) were used in the fin height simulations. The heatsinks in these simulations have a base thickness of 1 mm which is different from the heatsink of the previously shown data which had a base thickness of 0.8 mm. The reason is in consequence of the fact that these simulations with a base thickness of 1 mm were performed before the custom heatsinks were machined, and the machine shop could not meet the heatsink specifications due to tooling limitations, etc. Nevertheless, the results of the fin thickness sweep for the radiation efficiency, peak directivity and peak gain are shown in Figure 5-60, Figure 5-61, and Figure 5-62, respectively. As shown, the fin thickness has very little effect on the trend of the efficiency, directivity and gain versus fin height. However, the largest deviations with fin thickness occur with the fins parallel to the radiating edges. The maximum deviations of radiation efficiency for the non-radiating and radiating edge cases are 3.5 and 9.4 percentage points, respectively. For the peak directivity, the maximum deviations for the non-radiating and radiating edge cases are 0.46 dB and 1.57 dB, respectively. The maximum deviations of the gain for the non-radiating and radiating edge cases are 0.56 dB and 1.33 dB, respectively.

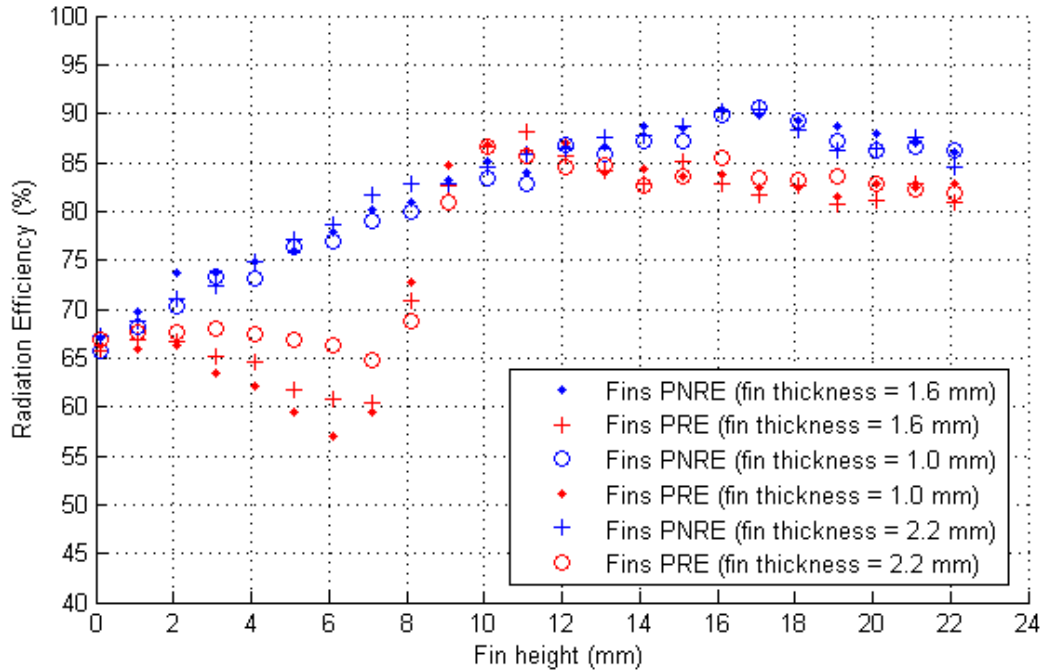


Figure 5-60. Fin thickness sweep for radiation efficiency vs. fin height for 3-finned antennas with a heatsink base thickness = 1 mm at 5.80 GHz

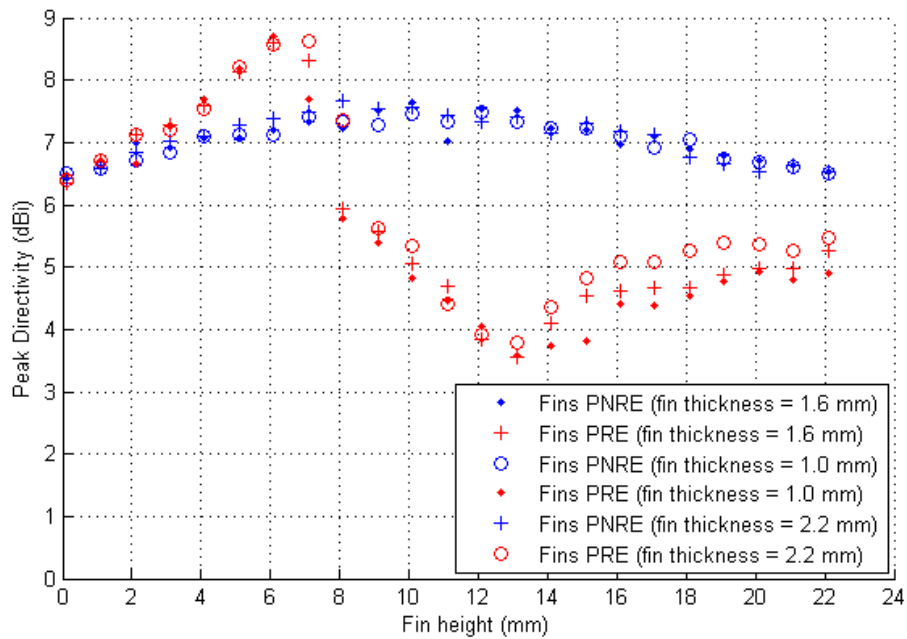


Figure 5-61. Fin thickness sweep for peak directivity vs. fin height for 3-finned antennas with a heatsink base thickness = 1 mm at 5.80 GHz

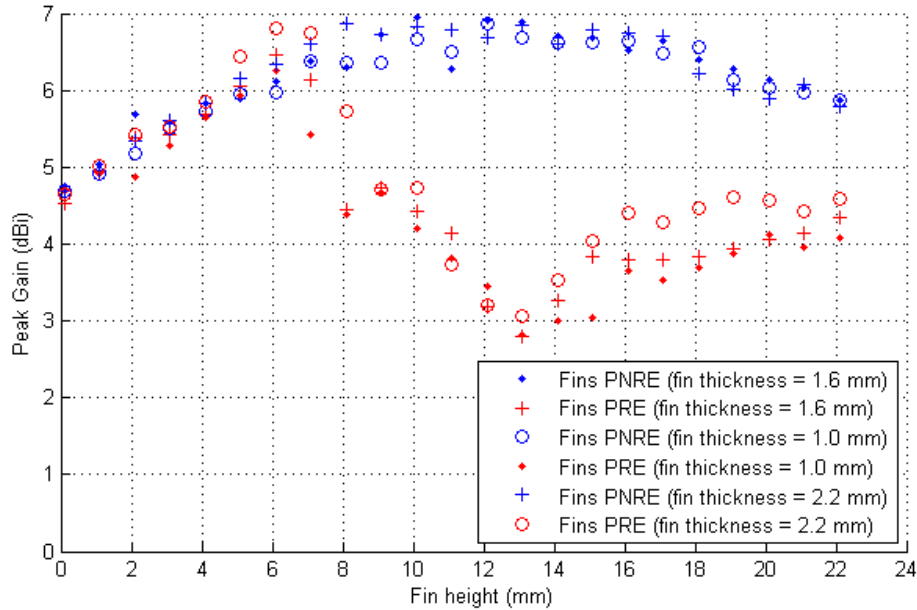


Figure 5-62. Fin thickness sweep for peak gain vs. fin height for 3-finned antennas with a heatsink base thickness = 1 mm at 5.80 GHz

5.4 Two-Finned Heatsink Antenna Results

Next, two-finned heatsink antennas were simulated by removing the center fin. This allows the effect of the center fin to be isolated and evaluated. The center fin was effectively removed by reducing its height to 0.001 mm. The results are compared with the results of the 3-finned antennas discussed previously.

5.4.1 Resonant Frequency and Input Reflection Coefficient

The primary resonant frequencies of the 2-finned and 3-finned antennas are compared in Figure 5-63 and Figure 5-64 for the radiating edge and non-radiating edge orientations, respectively. For the radiating edge orientation, the primary and alternate resonant frequencies are nearly identical as shown. For the non-radiating edge orientation, the primary resonant frequencies are also nearly identical for the 2-finned and 3-finned antennas; however, the alternate frequency is not present in the 2-finned case. Therefore, while the center fin has very

little effect on the primary resonant frequency, it is the cause of the alternate resonance for the non-radiating edge (FPNRE) orientation. In the radiating edge (FPRE) orientation, the center fin has almost no effect on either the primary or alternate resonant frequencies.

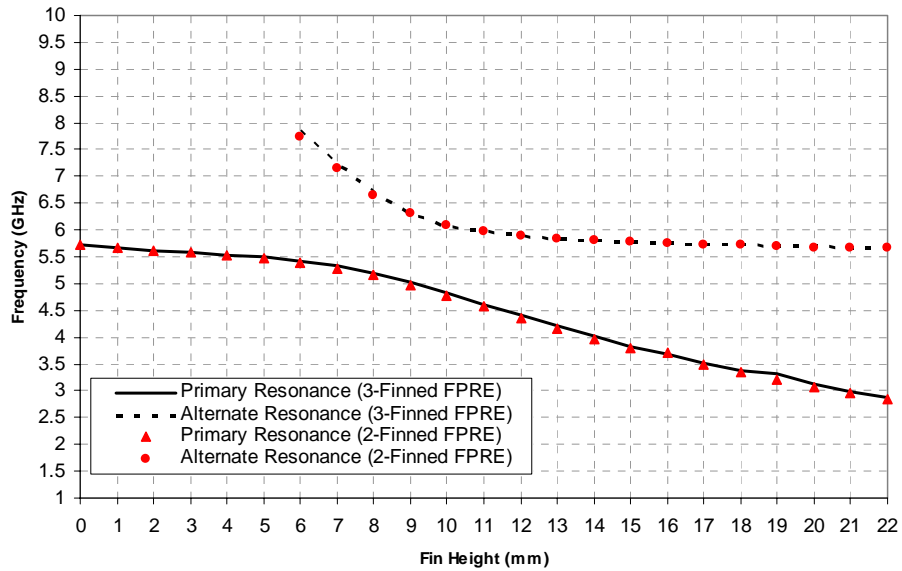


Figure 5-63. Simulated resonant frequencies of 2-finned and 3-finned antennas vs. fin height for fins parallel to the radiating edges (FPRE)

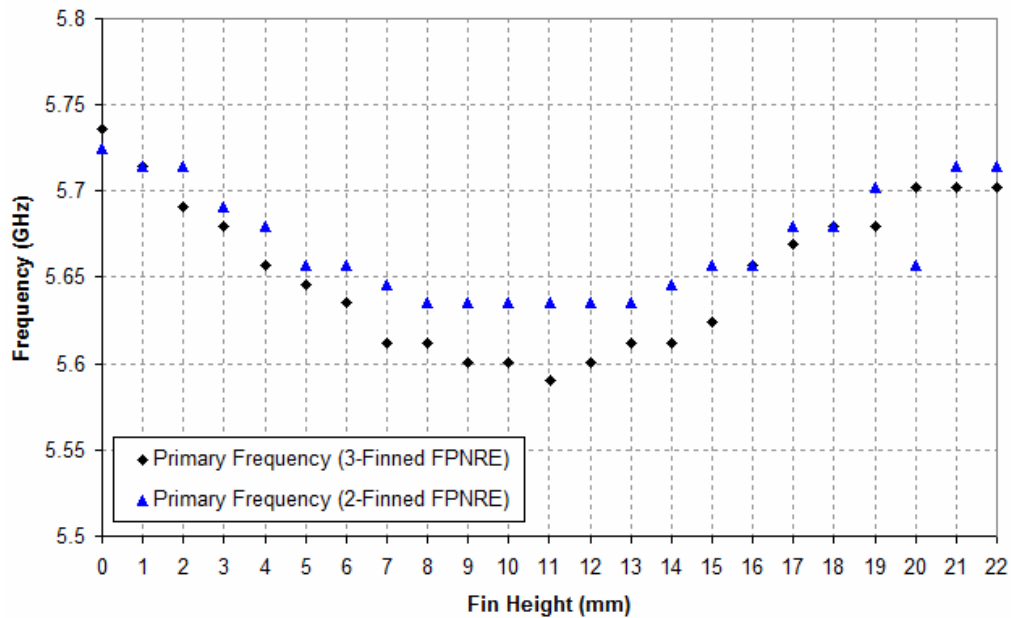


Figure 5-64. Simulated primary resonant frequencies of 2-finned and 3-finned antennas vs. fin height for fins parallel to the non-radiating edges (FPNRE)

The simulated return losses for the 2-finned heatsink antennas are compared with the return losses of the 3-finned heatsink antenna. Figure 5-65 through Figure 5-69 compare the return loss of the non-radiating edge antennas for fin heights of 2 mm, 6 mm, 12 mm, 16 mm, and 20 mm. The return loss for the radiating edge cases are shown in Figure 5-70 through Figure 5-74. As the figures show, the 2-fin and 3-fin return loss data match very well for all fin heights and orientations; however, in the FPNRE orientation, the alternate frequency is not present for the 2-fin antenna.

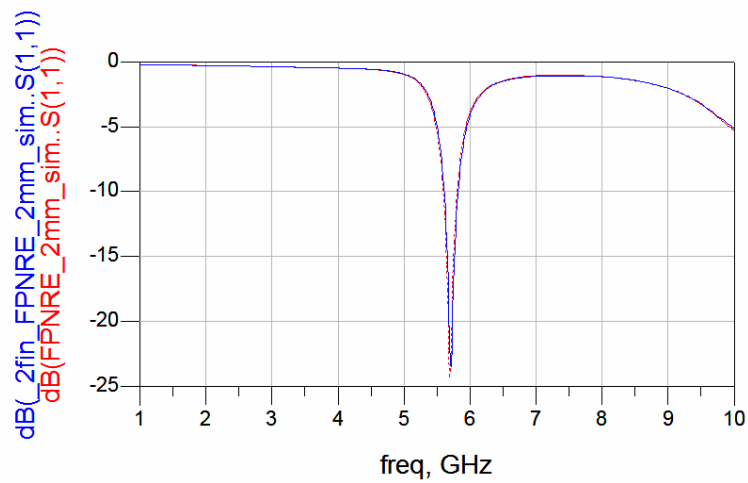


Figure 5-65. Comparison of simulated return loss data for 2-finned vs. 3-finned heatsink antennas at a fin height of 2 mm with fins along the non-radiating edges (FPNRE)

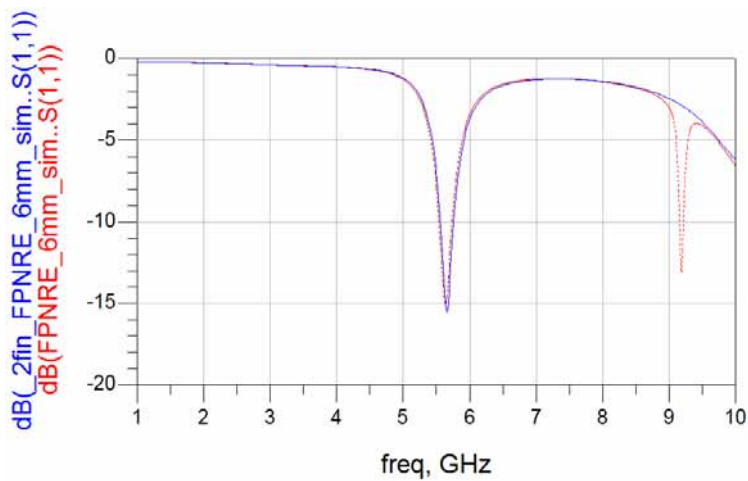


Figure 5-66. Comparison of simulated return loss data for 2-finned vs. 3-finned heatsink antennas at a fin height of 6 mm with fins along the non-radiating edges (FPNRE)

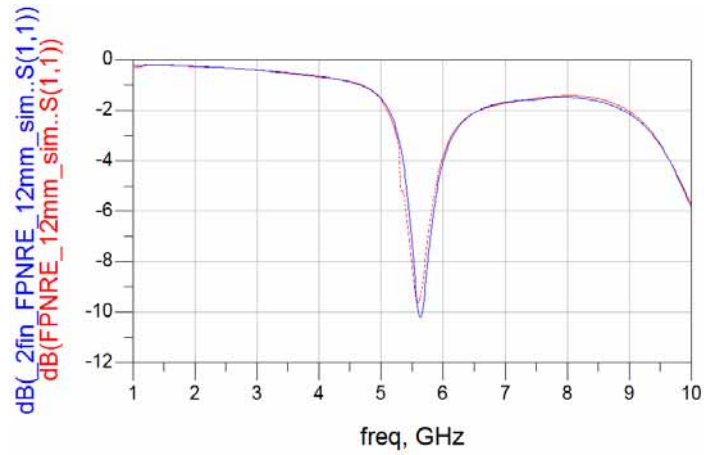


Figure 5-67. Comparison of simulated return loss data for 2-finned vs. 3-finned heatsink antennas at a fin height of 12 mm with fins along the non-radiating edges (FPNRE)

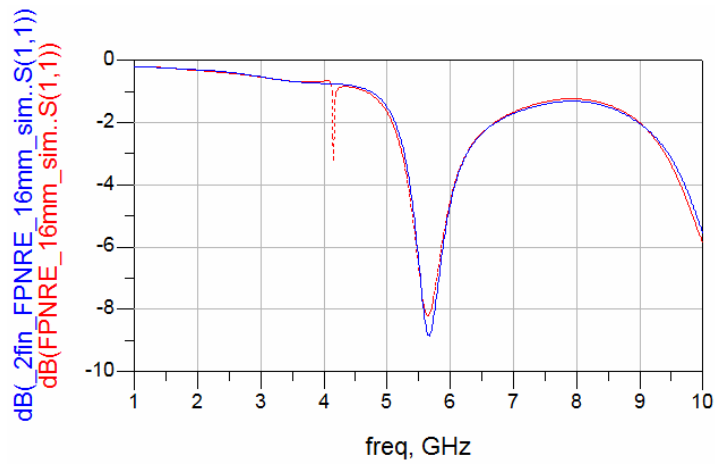


Figure 5-68. Comparison of simulated return loss data for 2-finned vs. 3-finned heatsink antennas at a fin height of 16 mm with fins along the non-radiating edges (FPNRE)

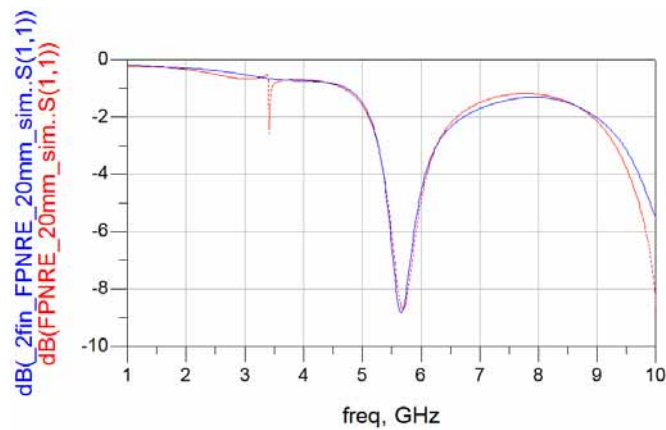


Figure 5-69. Comparison of simulated return loss data for 2-finned vs. 3-finned heatsink antennas at a fin height of 20 mm with fins along the non-radiating edges (FPNRE)

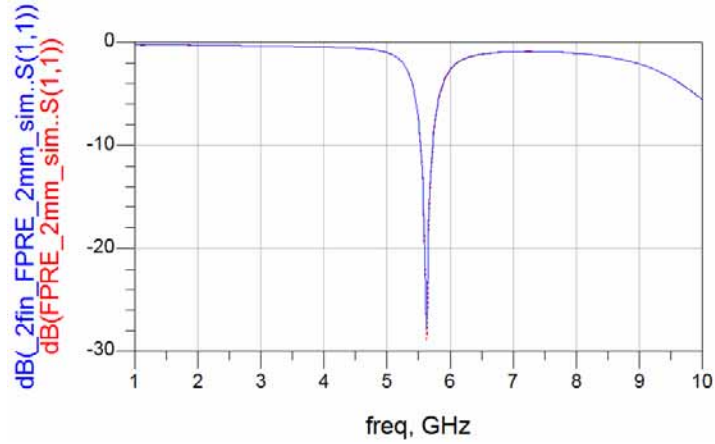


Figure 5-70. Comparison of simulated return loss data for 2-finned vs. 3-finned heatsink antennas at a fin height of 2 mm with fins along the radiating edges (FPRE)

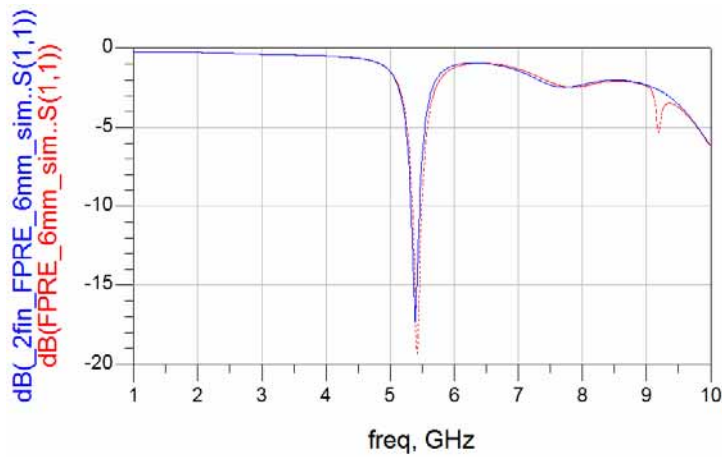


Figure 5-71. Comparison of simulated return loss data for 2-finned vs. 3-finned heatsink antennas at a fin height of 6 mm with fins along the radiating edges (FPRE)

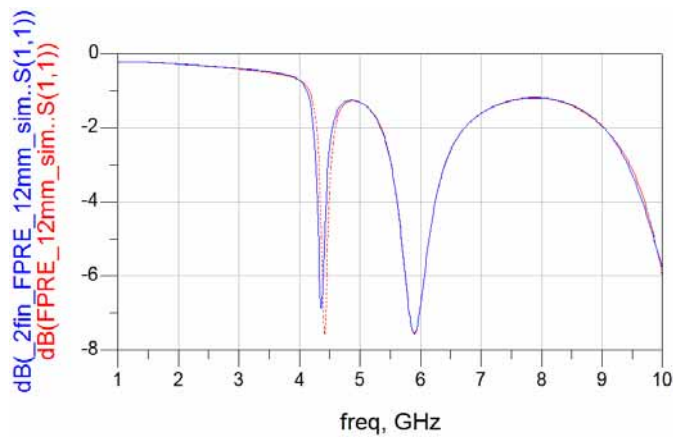


Figure 5-72. Comparison of simulated return loss data for 2-finned vs. 3-finned heatsink antennas at a fin height of 12 mm with fins along the radiating edges (FPRE)

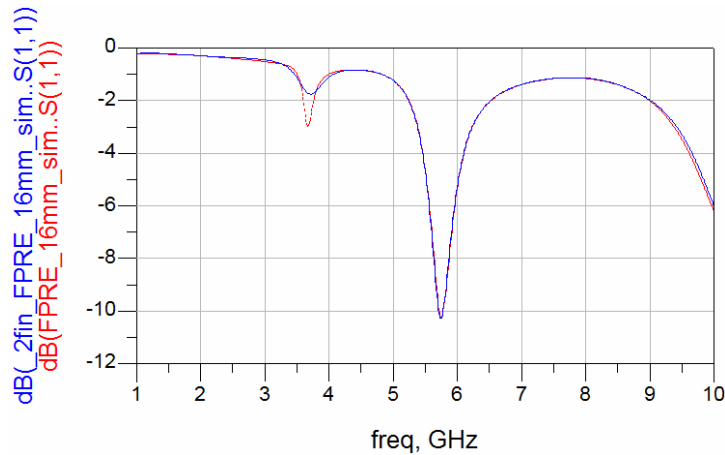


Figure 5-73. Comparison of simulated return loss data for 2-finned vs. 3-finned heatsink antennas at a fin height of 16 mm with fins along the radiating edges (FPRE)

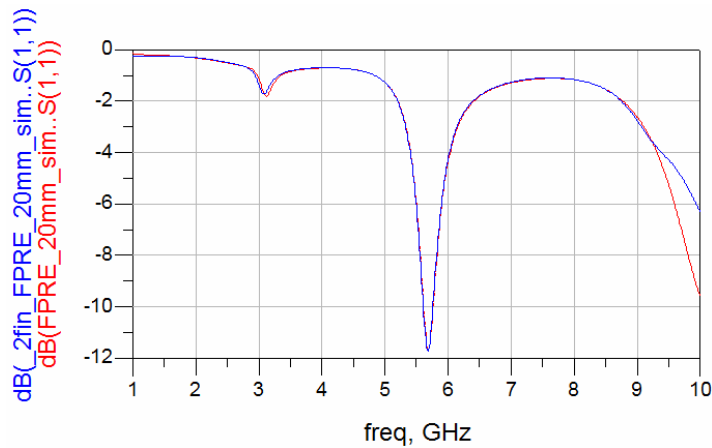


Figure 5-74. Comparison of simulated return loss data for 2-finned vs. 3-finned heatsink antennas at a fin height of 20 mm with fins along the radiating edges (FPRE)

5.4.2 Antenna Parameters

The antenna parameters for the 2-finned antennas of both orientations were compared with the data from the 3-finned simulations. The heatsink base thickness is 0.8 mm and the fin thickness is 1.0 mm. The results for the radiation efficiency, peak directivity, and peak gain are reported in Figure 5-75, Figure 5-76, and Figure 5-77, respectively. As shown in the figures, the antenna parameters for the 2-finned track very closely with the parameters of the 3-finned antennas over the fin height range shown. This implies further that the center fin has very little effect on the antenna behavior and performance other than being responsible for the alternate

resonance in the FPNRE case. Vertical currents generated on each side of the center fin are in the opposite direction and have relatively the same magnitude (Figure 5-36).

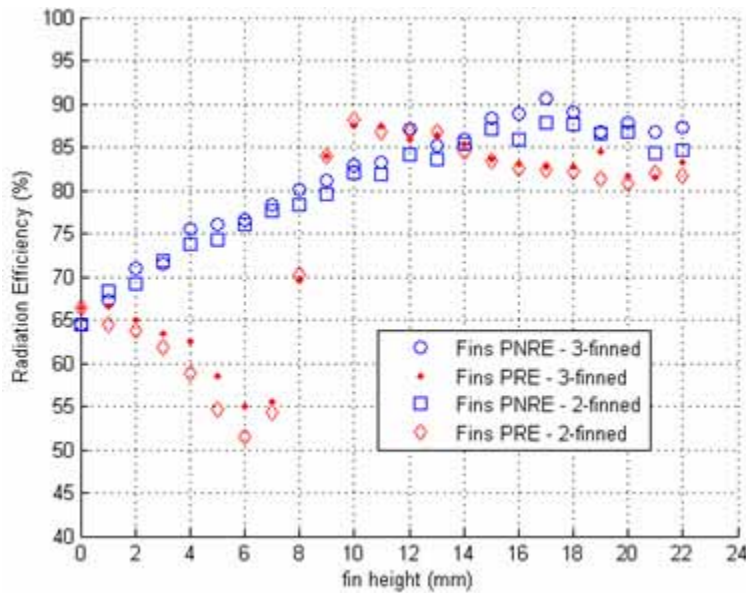


Figure 5-75. Comparison of radiation efficiency vs. fin height for 2-finned and 3-finned 5.8 GHz heatsink antennas

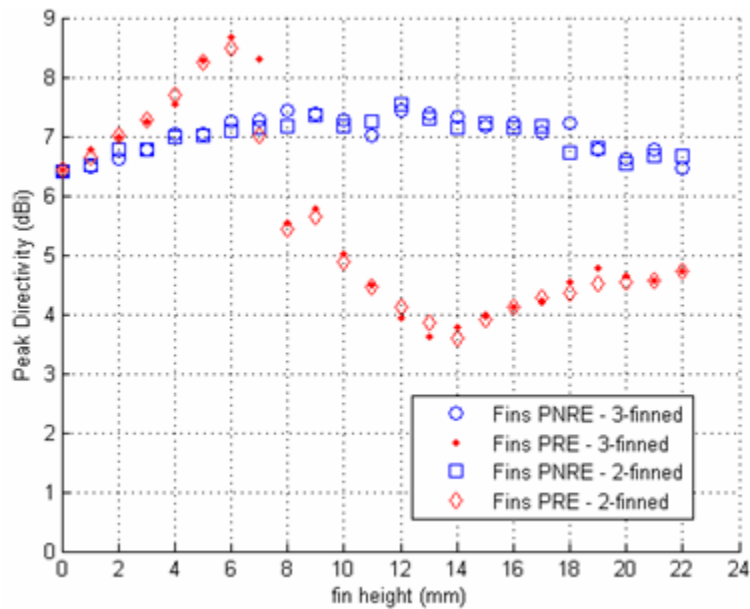


Figure 5-76. Comparison of peak directivity vs. fin height for 2-finned and 3-finned 5.8 GHz heatsink antennas

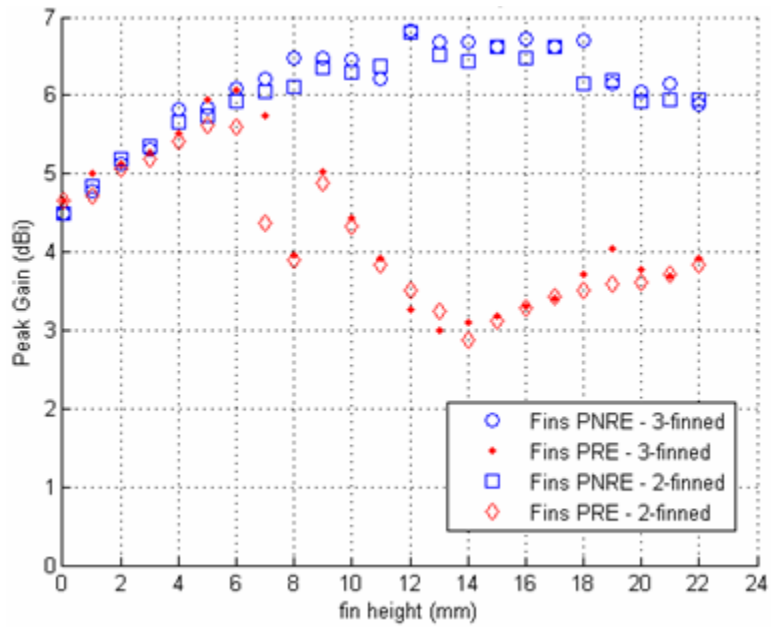


Figure 5-77. Comparison of peak gain vs. fin height for 2-finned and 3-finned 5.8 GHz heatsink antennas

5.5 Multiple Fin Results

Previously, three- and two-finned heatsink antennas were studied. Next, the number of fins on the heatsink was increased up to six fins in both orientations. The fin height was swept in simulation in order to observe the effect of adding multiple fins on the antenna parameters. The heatsink base thickness is 0.8 mm and the fin thickness is 1.0 mm. The results are shown in Figure 5-78 through Figure 5-83.

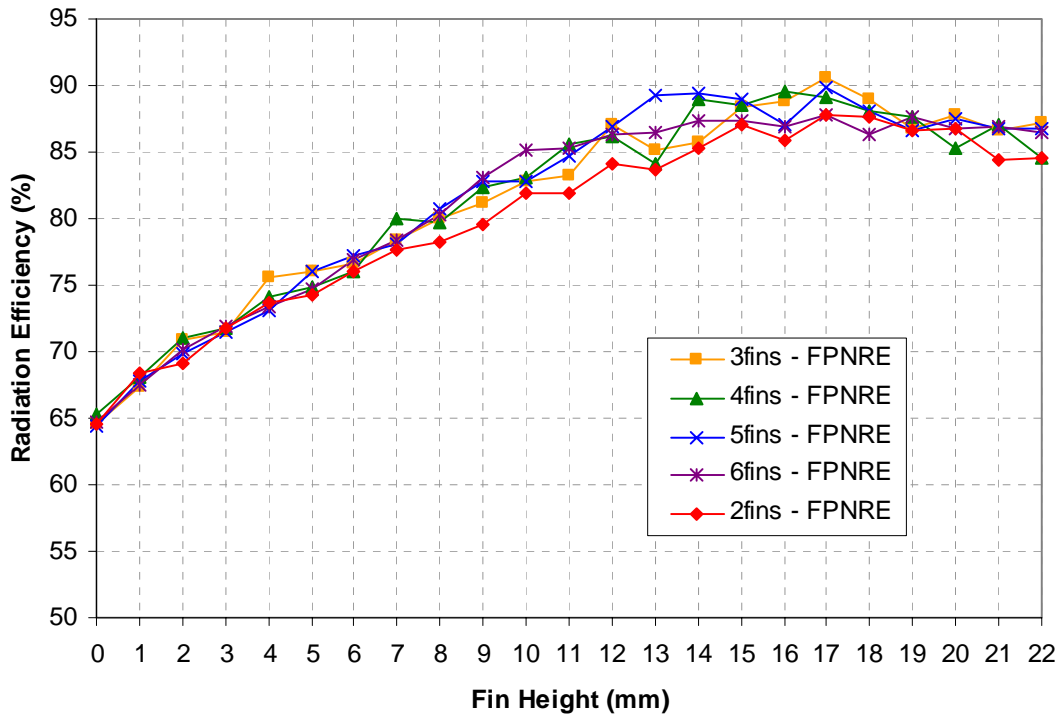


Figure 5-78. Comparison number of fins on radiation efficiency vs. fin height with fins parallel to the non-radiating edges (FPNRE) at 5.80 GHz

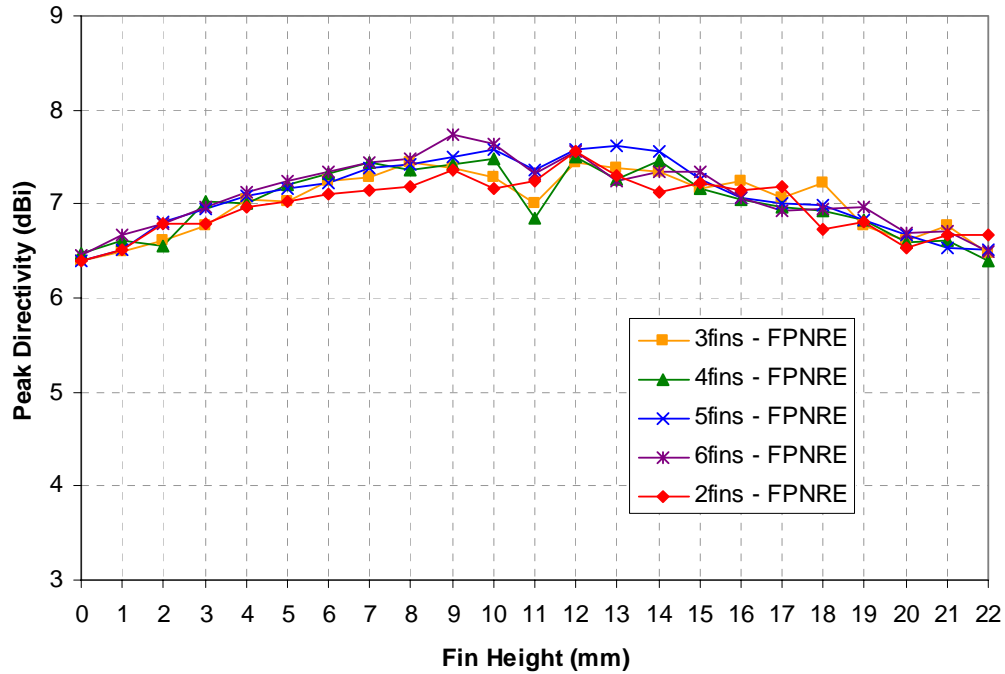


Figure 5-79. Comparison number of fins on peak directivity vs. fin height with fins parallel to the non-radiating edges (FPNRE) at 5.80 GHz

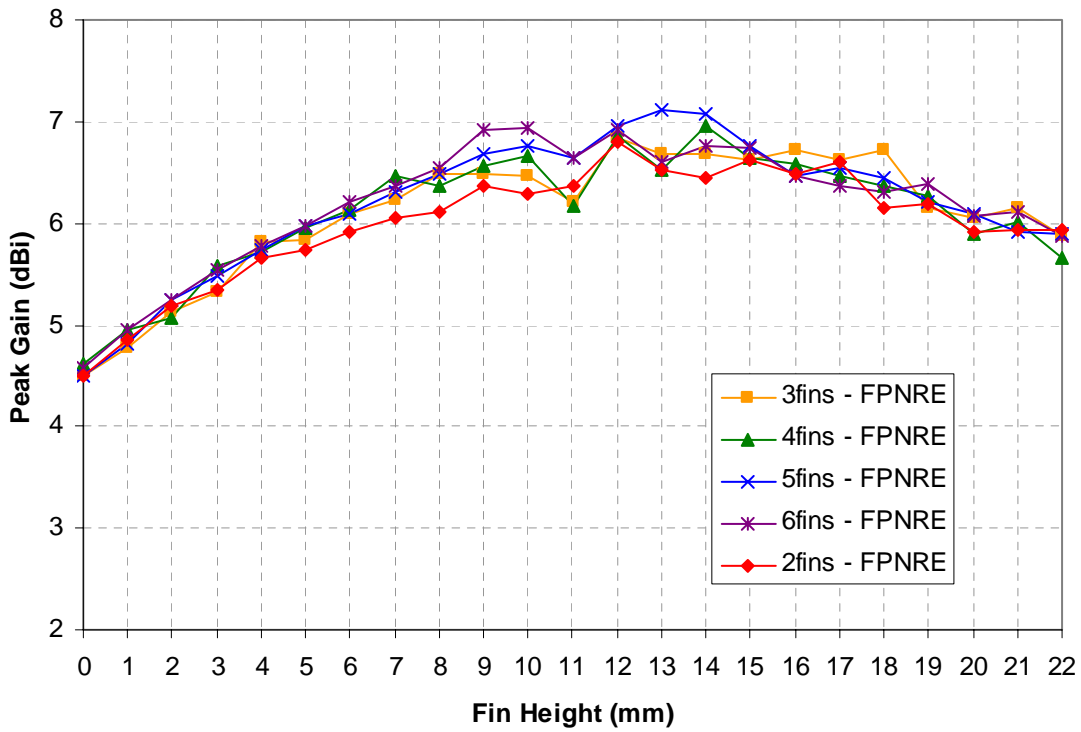


Figure 5-80. Comparison number of fins on peak gain vs. fin height with fins parallel to the non-radiating edges (FPNRE) at 5.80 GHz

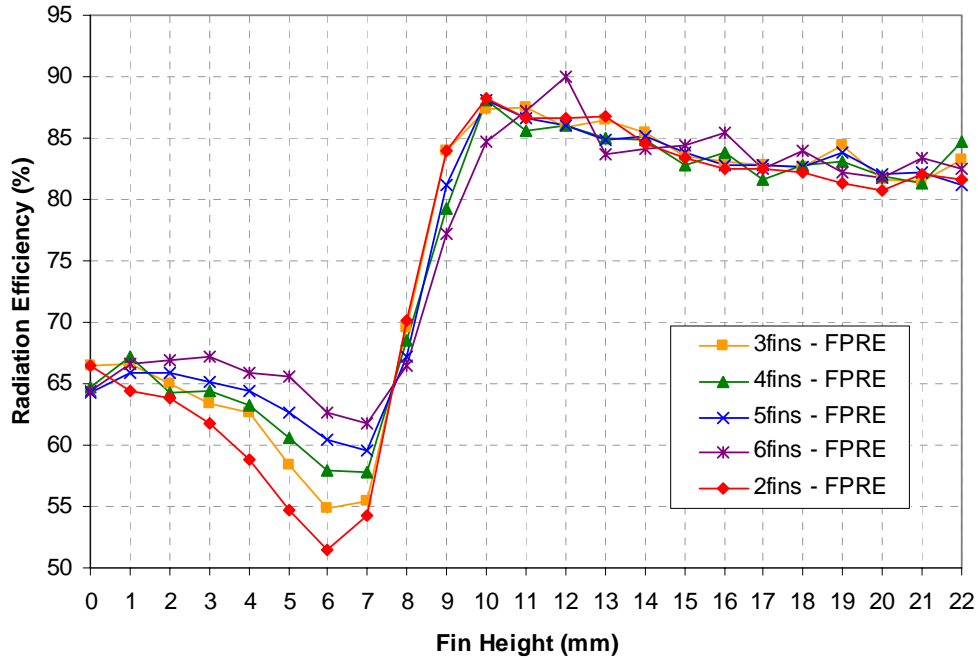


Figure 5-81. Comparison number of fins on radiation efficiency vs. fin height with fins parallel to the radiating edges (FPRE) at 5.80 GHz

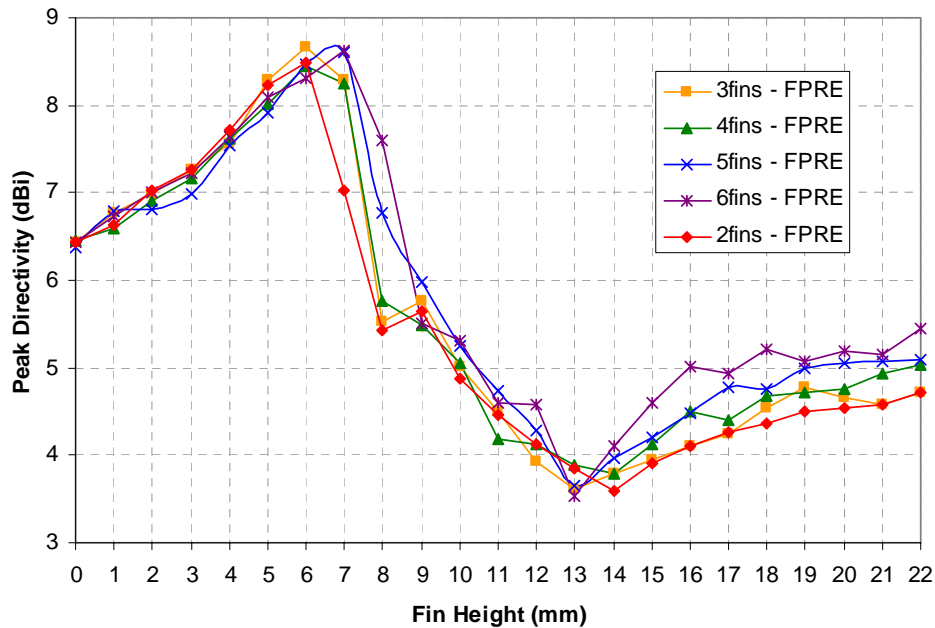


Figure 5-82. Comparison number of fins on peak directivity vs. fin height with fins parallel to the radiating edges (FPRE) at 5.80 GHz

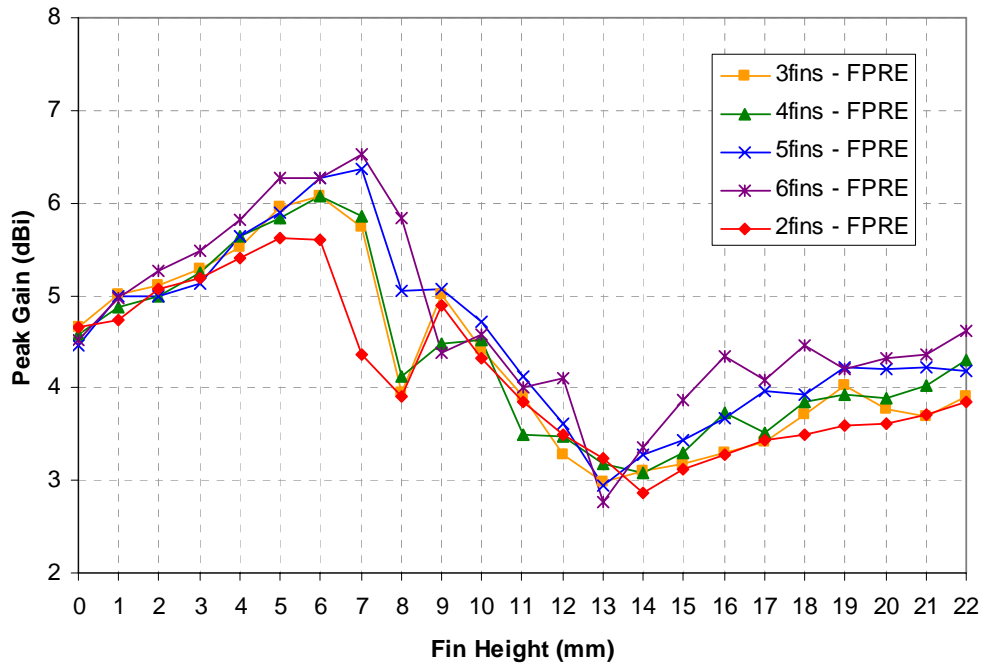


Figure 5-83. Comparison number of fins on peak gain vs. fin height with fins parallel to the radiating edges (FPRE) at 5.80 GHz

5.6 Pin-Fin Results

The pin-fin heatsink antenna from chapter 3 was revisited here for comparison to the extruded-fin heatsink antennas. A 36-fin (6 x 6) pin-fin heatsink was used on the same platform as the 6-fin 5.8 GHz extruded-fin heatsink antennas discussed in the previous section. Each fin has a thickness of 1 mm x 1 mm to remain consistent with the thickness of the extruded fins (1 mm) and a base thickness is 0.8 mm. The HFSS model is shown in Figure 5-84.

The resonant frequencies of the pin-fin heatsink antenna are shown in Figure 5-85. The data is compared with the resonant frequencies of the 3-finned extruded-fin heatsink antenna with fins parallel to the radiating edges (FPRE). As shown in the figure, both the primary and alternate resonant frequencies of the pin-fin heatsink antenna match almost identically with those of the extruded-fin heatsink with fins parallel to the radiating edges.

The radiation efficiency, peak directivity and peak gain versus fin height for the pin-fin heatsink antenna are compared with the 6-fin extruded-fin heatsink antenna in Figure 5-86, Figure 5-87, and Figure 5-88, respectively. As shown in the figures, the pin-fin parameters track very closely with the extruded-fin heatsink antenna with fins parallel to the radiating edges (Fins PRE). As with the extruded-fin heatsink with fins parallel to the radiating edges, the pin-fin heatsink prohibits the horizontal current flow on the fins (the direction of current on the patch). The 3-D radiation patterns for the pin-fin heatsink antenna are shown in Figure 5-89 for various fin heights. These patterns are very similar to the patterns of the FPRE extruded-fin heatsink antenna (Figure 5-38).

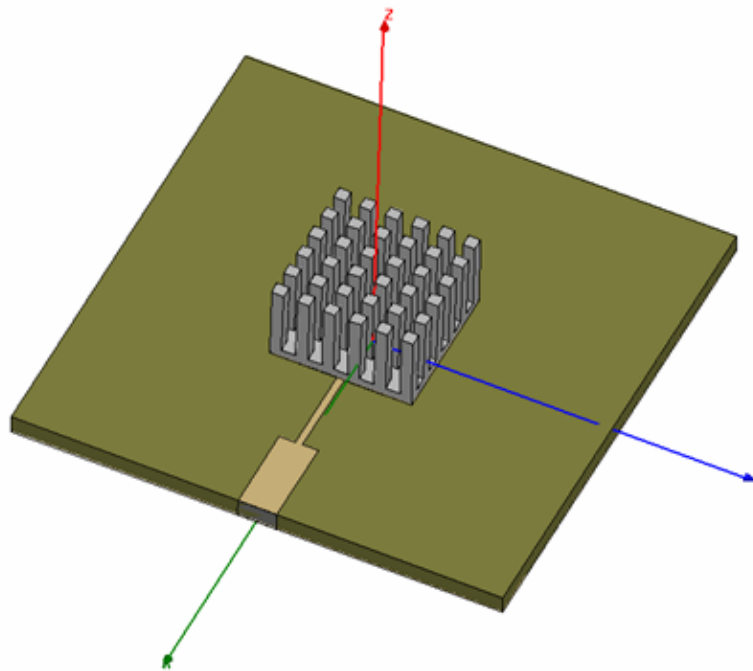


Figure 5-84. HFSS model of 36-fin (6x6) pin-fin heatsink antenna

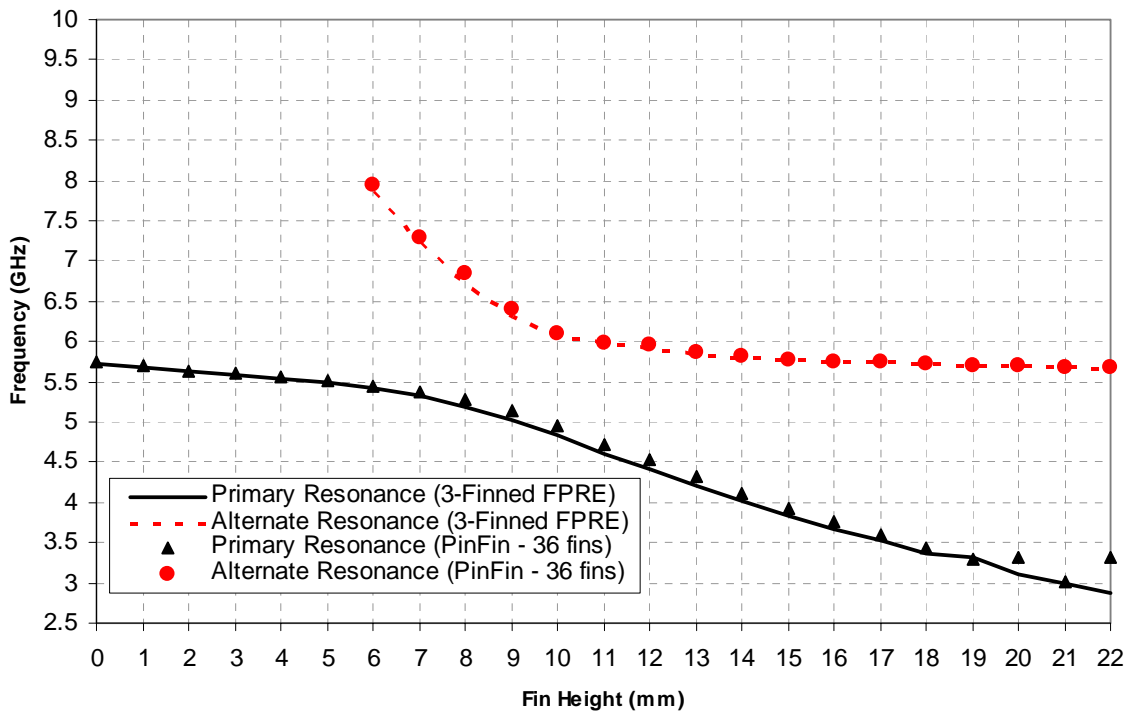


Figure 5-85. Resonant frequencies of the pin-fin heatsink antenna compared with the 3-finned extruded heatsink antenna with fins parallel to the radiating edges (FPRE)

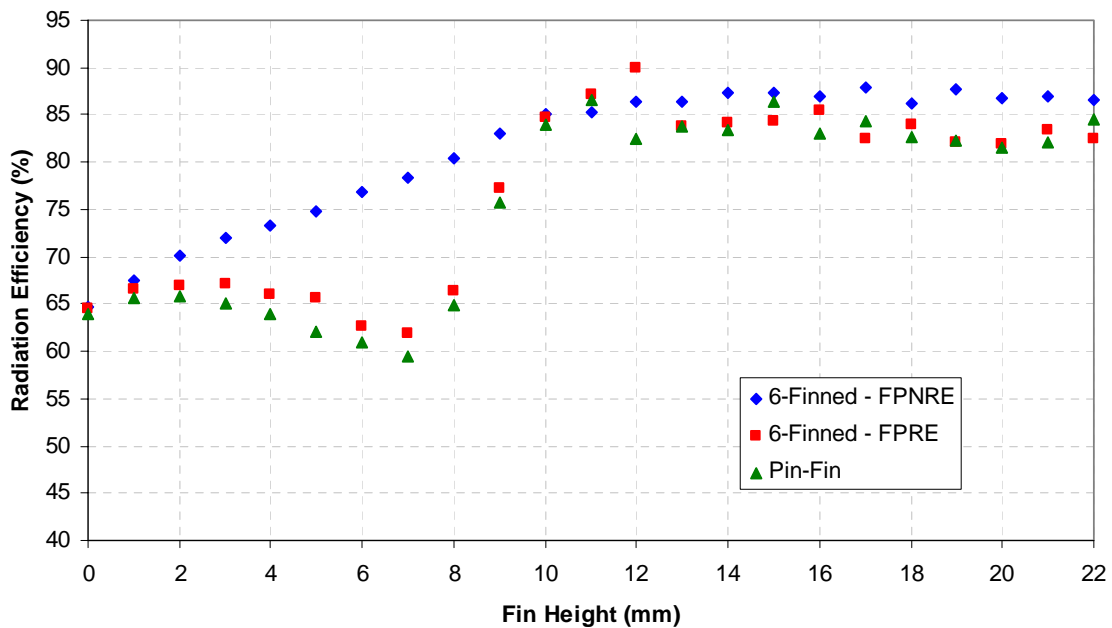


Figure 5-86. Comparison of pin-fin and extruded-fin heatsink antenna radiation efficiency vs. fin height

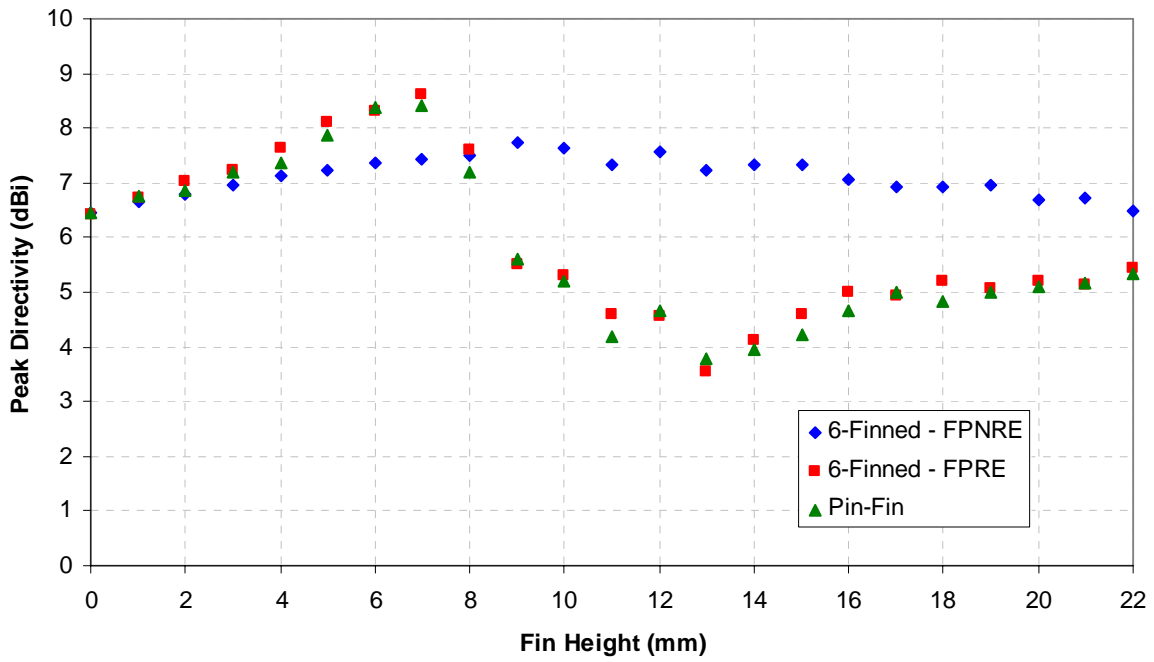


Figure 5-87. Comparison of pin-fin and extruded-fin heatsink antenna peak directivity vs. fin height

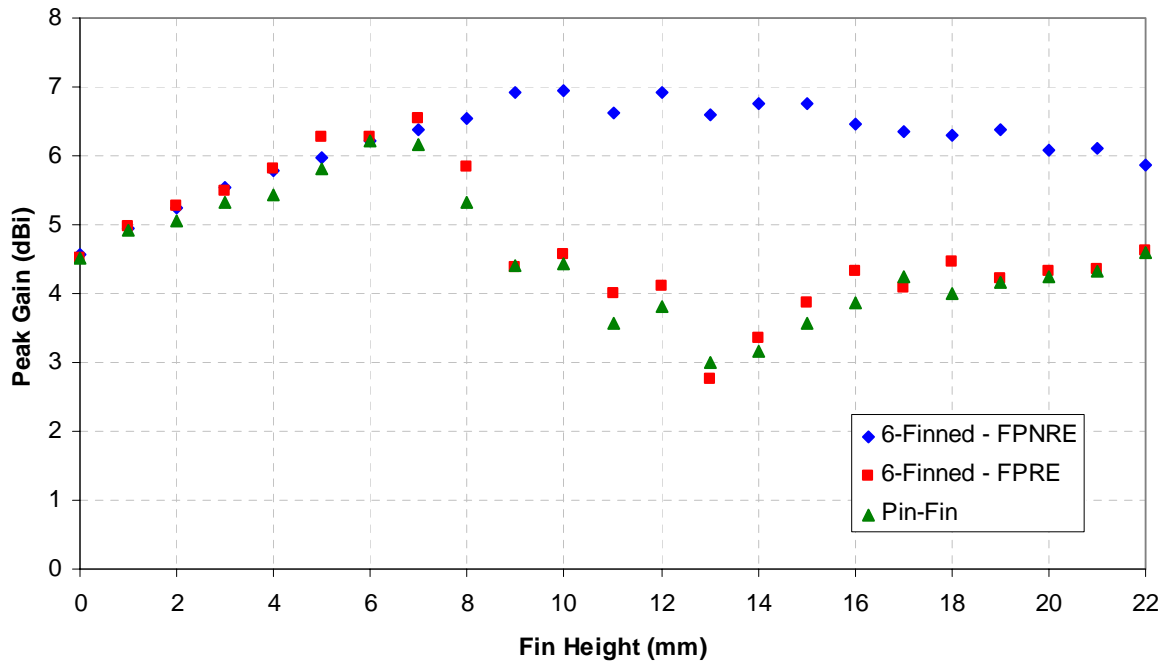


Figure 5-88. Comparison of pin-fin and extruded-fin heatsink antenna peak gain vs. fin height

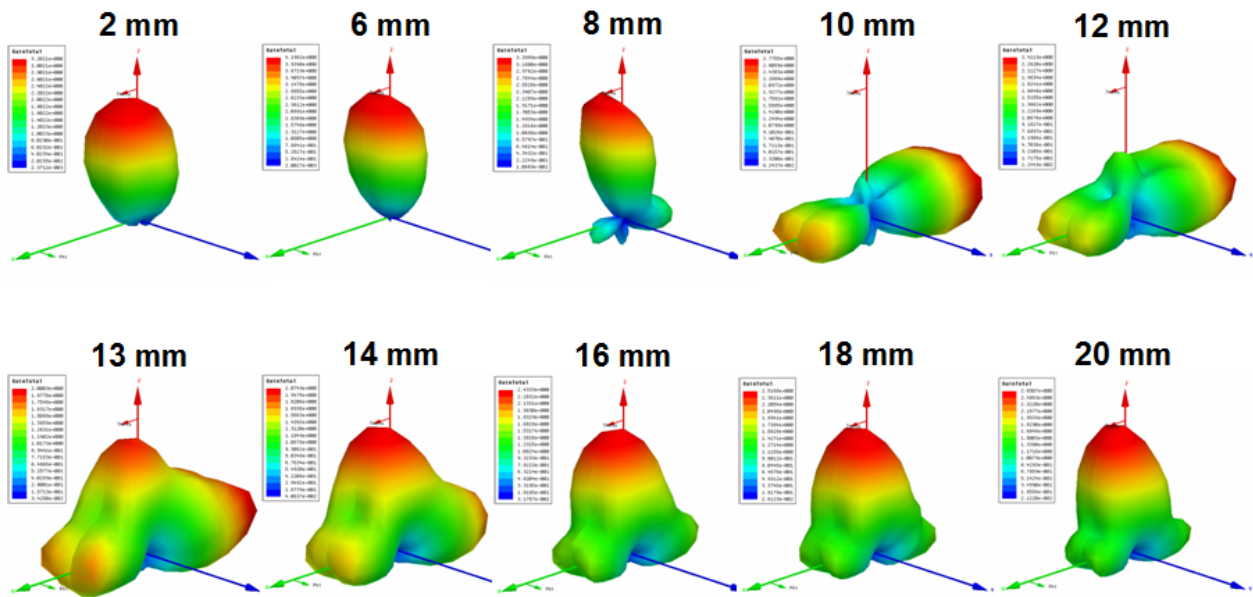


Figure 5-89. Simulated 3-D radiation patterns vs. fin height for 6x6 pin-fin heatsink antenna

5.7 Summary of Results

Sweeping the fin height of the 3-finned heatsink exhibited several interesting effects on the antenna parameters. Moreover, the orientation of the heatsink fins also plays an important role, thus, a discussion on the effects requires taking into account both fin height and orientation.

Dual-frequency behavior was demonstrated for both the radiating and non-radiating edge cases of the 3-finned heatsink antenna. Also, the effect of the fin height on the resonant frequency of the antenna is substantially different between the two heatsink orientations. For the case of the fins parallel to the non-radiating edges, the change in primary resonant frequency versus fin height is relatively small. For the radiating edge case, however, the primary resonant frequency changes significantly. The center fin creates an alternate resonance in the FPNRE case but has almost no effect in the FPPE case.

The radiation patterns of the heatsink antenna are highly dependent on orientation, and in the FPRE case, fin height. The FPNRE-oriented fins allow longitudinal fin currents while the FPRE-oriented fins prohibit longitudinal fin currents and allow vertical fin currents only. At fin heights comparable to a quarter-wavelength in the FPRE case, the antenna begins radiating end-fire lobes in the E-plane. This change in radiation pattern results in a peak directivity/gain trend which is highly dependent on fin height. This is in contrast to the relatively independent radiation patterns and peak directivity/gain of the FPNRE case versus fin height. The pin-fin heatsink antenna behaves very similarly to the extruded-fin FPRE heatsink antenna since both fin arrangements allow only vertical fin currents and prohibit longitudinal fin currents.

Both fin orientations provide efficiency enhancement; however, this degree to which this enhancement occurs is dependent upon the fin height and orientation. For low fin heights in the FPRE case, the efficiency actually decreased reinforcing the importance of fin orientation. The radiation efficiency is also altered by the 3-finned heatsink structure. In both orientations, the radiation efficiency increased as the fin height increased.

The 2-finned heatsink antenna was compared to the 3-finned heatsink antenna. The results of the 2-finned heatsink antenna matched closely with the antenna parameters of the 3-finned version. The results showed that the outer two fins play the dominant role in the behavior of the extruded-fin heatsink antenna. However, the center fin was shown to be responsible for the alternate resonance in the 3-fin extruded-fin FPNRE case. Other heatsink parameters such as fin thickness and number of fins were evaluated and shown to have a less significant effect compared with fin orientation and fin height.

5.8 Conclusion

The results reported in this chapter are the result of 589 separate, full-wave electromagnetic simulations in addition to the measurements reported. The large number of

simulations required was due to the many number of fin heights, the number of fin orientations, the number of fins, different heatsink types, the different fin thicknesses, and the different resonances. The results of these simulations were presented in such a manner to provide the reader with an understanding of how heatsink antennas based on common heatsink types behave over parametric sweeps of the heatsink physical parameters. The results show a significant difference in antenna performance between the two fin orientations. Interestingly, the pin-fin heatsink antenna behaved similarly to the extruded-fin heatsink antenna with the FPRE orientation. The results showed that the heatsink can improve performance over that of a patch antenna on the same substrate. Also, significantly different resonances, radiation patterns, and gains can be achieved by using a specific fin orientation and fin height.

The results demonstrated that if the antenna designer desires the antenna's primary resonant frequency to be relatively independent on fin height, then the fins should be oriented parallel to the non-radiating edges of the patch. This orientation also allows the primary resonant frequency, directivity and gain to be relatively independent of fin height. This facilitates optimization of thermal performance of the heatsink by modifying the fin height without dramatically changing the primary resonant frequency, directivity and gain simultaneously. This simplifies the optimization for the heatsink designer considerably. In contrast, the data show that if the antenna designer desires to exploit the effects of the fin height on the resonant frequency, directivity, and gain, the fins should be aligned parallel to the radiating edges of the patch. This orientation has a dramatic effect on these antenna parameters and allows higher gain and smaller antenna (planar size) to be designed for a given operating frequency.

In summary, key design tips are listed below for the heatsink antenna designer using the structure discussed in this study:

1. Maximum/minimum directivity → align fins parallel to radiating edges (can achieve highest and lowest directivity)
2. Maximize radiation efficiency with a compact, low-profile heatsink → align fins parallel to non-radiating edges since efficiency increase is observed even at low fin heights
3. Independence of heatsink fin height and antenna parameters → align fins parallel to the non-radiating edges
4. Smaller planar size → align fins parallel to the radiating edges since the primary resonant frequency reduces significantly with increases in fin height
5. Dual-frequency operation → possible with both orientations at larger fin heights; however, alternate resonances removed with 2-fin FPNRE heatsink antenna

CHAPTER 6 BOXED AND CUBIC HEATSINK ANTENNAS

6.1 Introduction

Chapter 5 discussed the 3-finned and 2-finned heatsink antennas and how the fin height and orientation affected the antenna parameters. A new type of heatsink structure is studied here (boxed and cubic heatsink antenna) and the results are compared to those from the previous chapter. The boxed heatsink has a top side identical to the heatsink base and three vertical fins. The cubic heatsink is just a solid block of aluminum (no fins). These new types are actually not good heatsinks and are used mainly as analytical tools. The boxed heatsink's modification induces noticeable changes in the antenna parameters including dual-frequency suppression, resonant frequency stabilization across the fin height range, and radiation pattern changes. In addition, a cubic, or block, heatsink was also studied here and compared with the results from the boxed heatsink antenna simulations.

6.2 Simulations and Results

6.2.1 Simulation Setup

The simulation setup for the boxed heatsink antenna was similar to the 5.8 GHz 3-finned antenna in Chapter 5; however, the heatsink structure was modified with an enclosed top. This top side bridges the gap between the fins and has the same thickness as the base. The heatsink antenna dimensions are reported in Table 6-1. The HFSS models for the boxed heatsink antennas are shown in Figure 6-1 and Figure 6-2.

A cubic, or block, structure was also simulated. The HFSS model is shown in Figure 6-3. Both the boxed and cubic structures are poor heatsinks due to its low surface area and poor airflow, but it they can be used as analytical tools for a better understanding of the heatsink antennas of Chapter 5.

Table 6-1. Antenna dimensions for HFSS setup (simulated)

Parameter (mm)	Boxed Heatsink Antenna
Planar patch dimensions	11.79 x 11.79
Quarterwave transformer width	0.63
Quarterwave transformer length	7.27
Fifty-ohm line width	3.24
Fifty-ohm line length	7.27
Heatsink base thickness	0.80
Heatsink base dimensions	11.79 x 11.79
Fin thickness	1.00
Heatsink top thickness	0.80

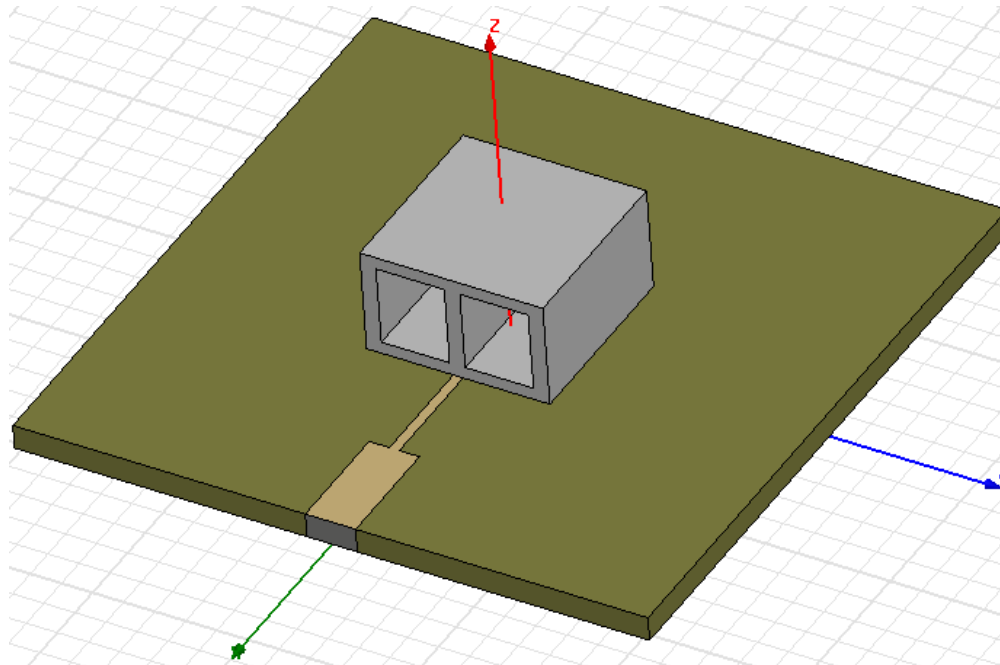


Figure 6-1. HFSS model of 5.8 GHz boxed heatsink antenna with 6 mm fins parallel to the non-radiating edges

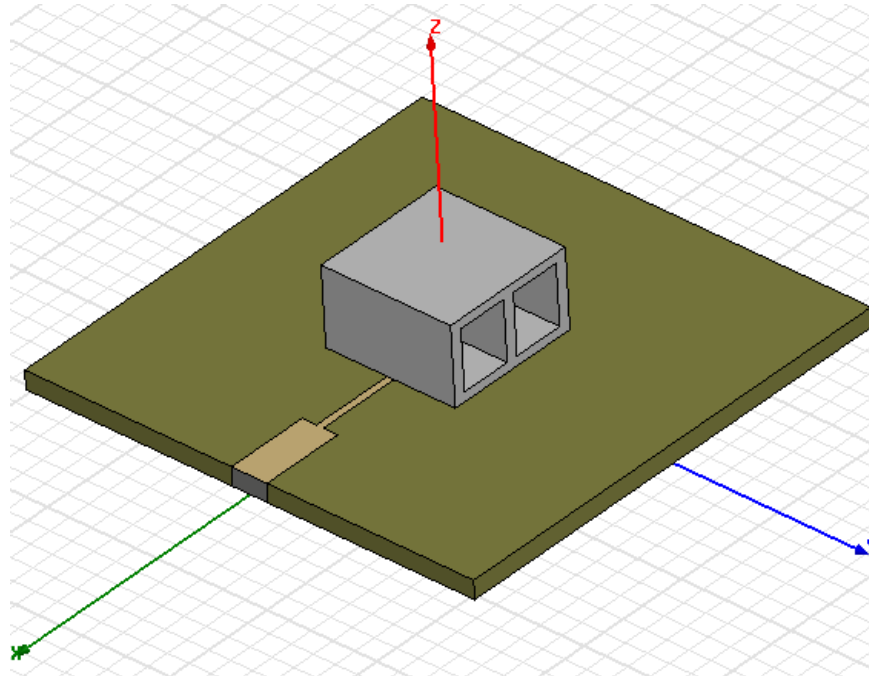


Figure 6-2. HFSS model of 5.8 GHz boxed heatsink antenna with 6 mm fins parallel to the radiating edges

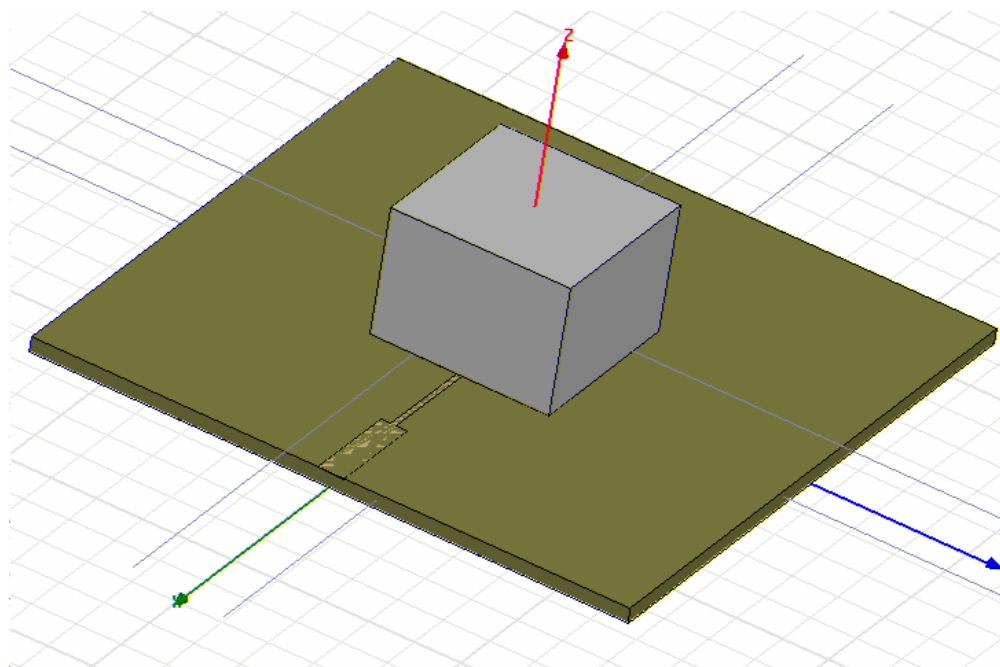


Figure 6-3. HFSS model of cubic heatsink antenna

6.2.2 Results of Boxed Heatsink Antenna Simulations

In Chapter 5, the heatsink had a significant effect on the resonant frequency with the fins parallel to the radiating edges of the patch. Furthermore, a dual-frequency resonance was observed for both radiating edge and non-radiating edge cases. Unique to the non-radiating edge case was the relative independence of the primary resonant frequency to the fin height.

The simulated return losses of the boxed and 3-finned heatsink antennas with 9 mm fins parallel to the non-radiating edges (FPNRE) are compared in Figure 6-4. The top of the boxed heatsink removes the alternate frequency present in the 3-finned case. Excluding the removal of the alternate frequency, the boxed heatsink shows no other difference in return loss from the 3-finned FPNRE case of Chapter 5.

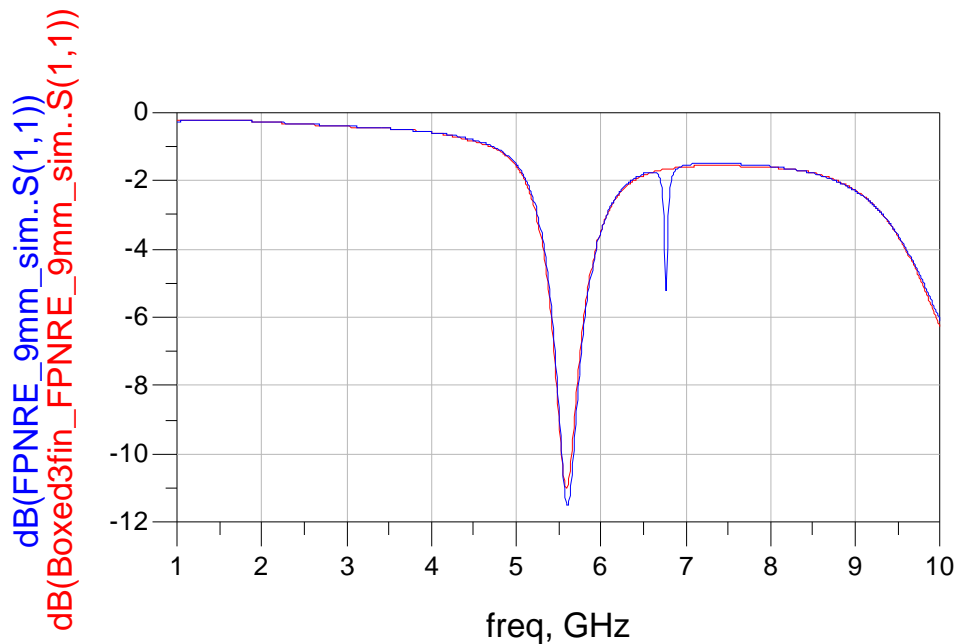


Figure 6-4. Simulated return loss of boxed and 3-finned heatsink antennas with 9 mm fins parallel to the non-radiating edges (FPNRE)

This is not the case for the FPPE orientation. The difference in return loss for the boxed heatsink and the 3-finned heatsink both with the FPPE orientation is significant. This is shown

in Figure 6-5. As shown in the figure, the boxed heatsink also removes the alternate resonance with this orientation.

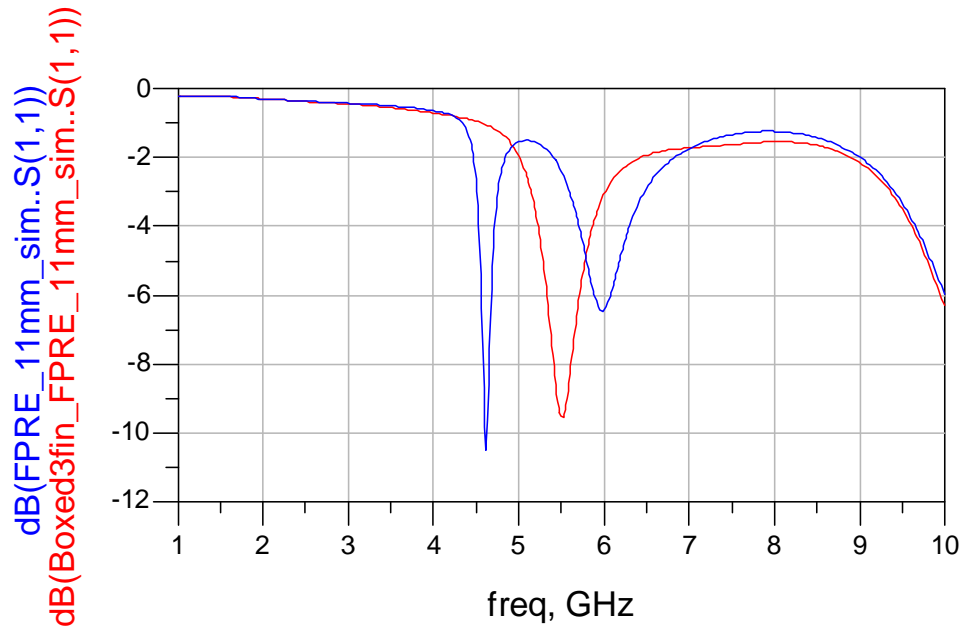


Figure 6-5. Simulated return loss of boxed and 3-finned heatsink antennas with 11 mm fins parallel to the radiating edges (FPRE)

Figure 6-6 displays the non-radiating edge resonant frequency data for the boxed heatsink antenna compared with the 3-finned heatsink results. The dual-frequency nature of the 3-finned heatsink is removed by the topside of the boxed heatsink up to 15 mm. From 16 mm to 22 mm, an alternate resonance appears. As with the 3-finned non-radiating edge case, this alternate resonance is very narrowband. The primary resonant frequency of the boxed heatsink in this case is almost identical to the primary resonant frequency of the 3-finned heatsink. Thus, in the non-radiating edge case, top plate of the boxed heatsink has very little effect on the primary frequency and removes the alternate frequency for lower fin heights.

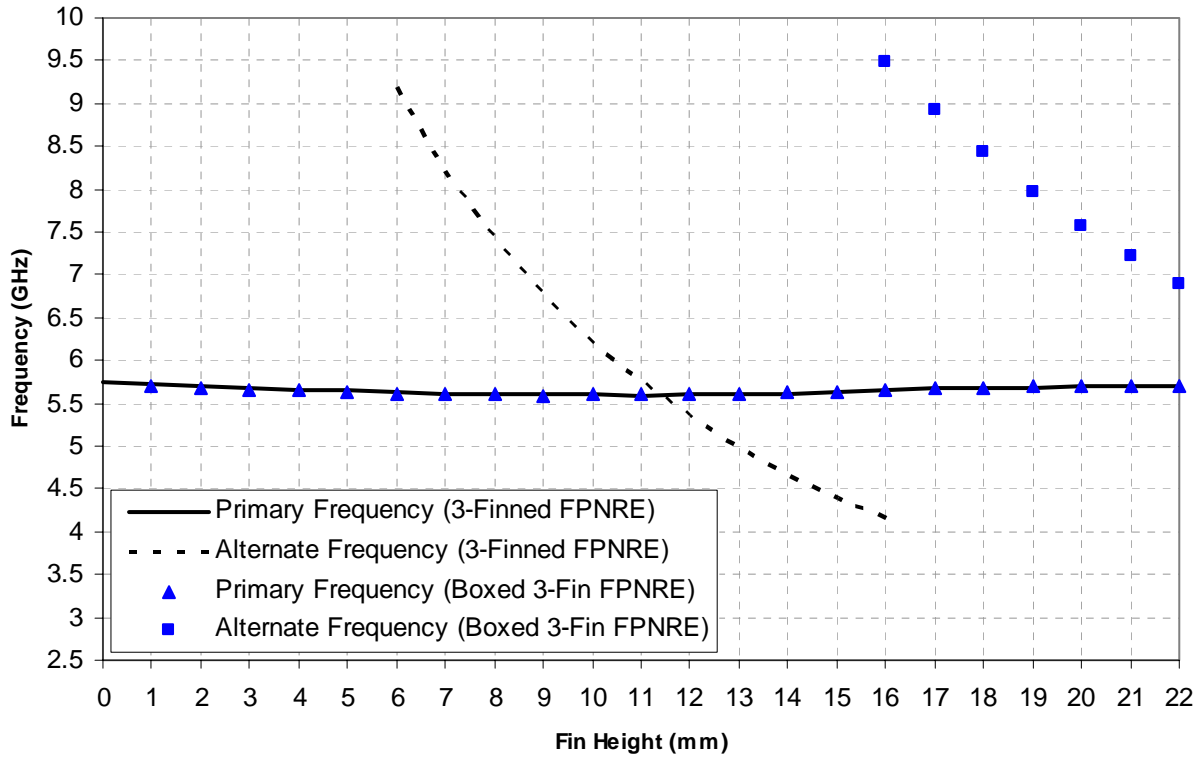


Figure 6-6. Resonant frequency of boxed and 3-finned heatsink antennas for the non-radiating edge case (FPNRE)

The top plate of the boxed heatsink in the FPRE case, however, has a dramatic effect on the resonant frequency. The resonant frequency versus fin height behavior is shown in Figure 6-7 for the boxed heatsink antenna for the FPRE orientation. This is compared with the 3-finned heatsink antenna data for the radiating edge case from the previous chapter. As shown in the figure, the dual-frequency nature of the 3-finned heatsink antenna is suppressed by the top of the boxed heatsink (up to 15 mm). Another resonance does appear with the boxed heatsink antenna from 16 to 20 mm. This alternate resonance is a weak and narrowband resonance in contrast to that of the 3-finned radiating edge case; therefore, for practical purposes, the boxed heatsink antenna only has a single resonance. Additionally, the heavily-influenced behavior of the primary resonant frequency by the fin height is, for the most part, removed. Thus, the boxed

heatsink creates resonant-frequency stabilization and dual-frequency suppression in the radiating edge case (FPRE) which is significantly different from its 3-finned counterpart.

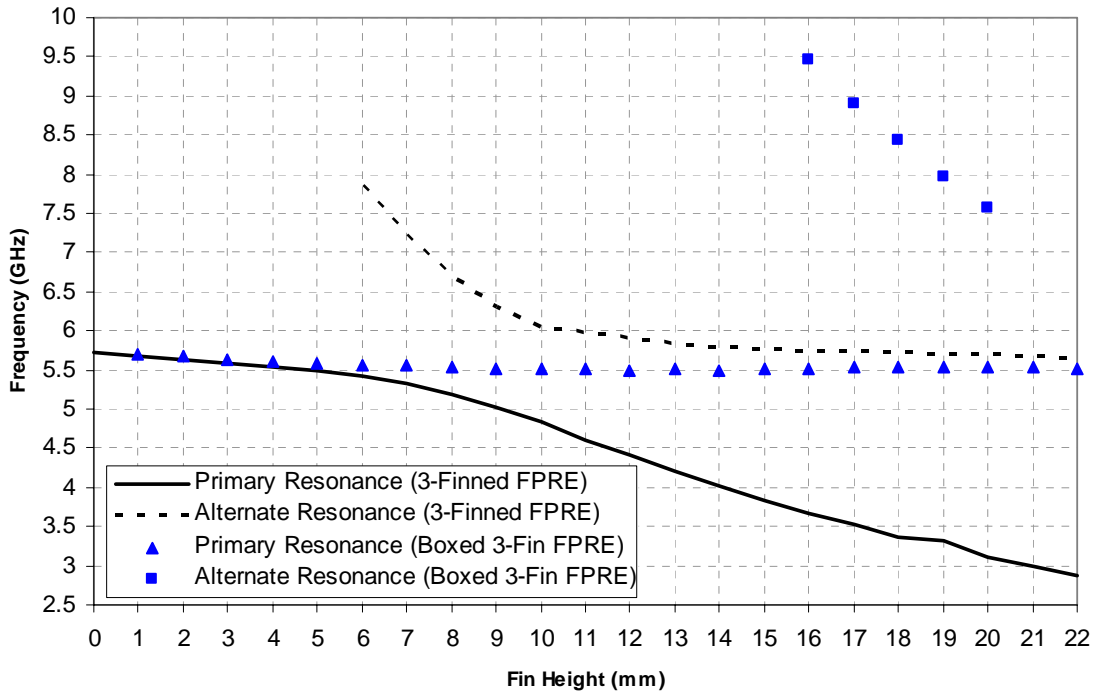


Figure 6-7. Resonant frequency of boxed and 3-finned heatsink antennas for the radiating edge case (FPRE)

The S_{11} data for various fin heights (1 mm to 21 mm in 4 mm increments) along the non-radiating edges and radiating edges are shown in Figure 6-8 and Figure 6-9, respectively. From the figures it is can be observed that increasing the fin height reduces the input resistance at resonance due to increased radiation (as discussed later) and thus reduced radiation resistance [Kum]. Also reduces the size of the loci on the Smith chart while the total distance traversed on the Smith chart versus frequency remains relatively the same. This reduction in locus size implies an increase in impedance bandwidth since a larger frequency range is tightly bound to a specific point. Bandwidth enhancement was also seen in Chapters 3 and 4. However, in order to benefit from the bandwidth improvement, the antenna would have to be matched due to the

alteration of the input impedance from 50 ohms. This could easily be done in a probe-fed configuration by shifting the feed-point closer to the edge (or further away from the center) thereby increasing the input resistance. Matching at each fin height is out of the scope of this study which is focused on the change in antenna parameters due to a parametric change in fin height and orientation.

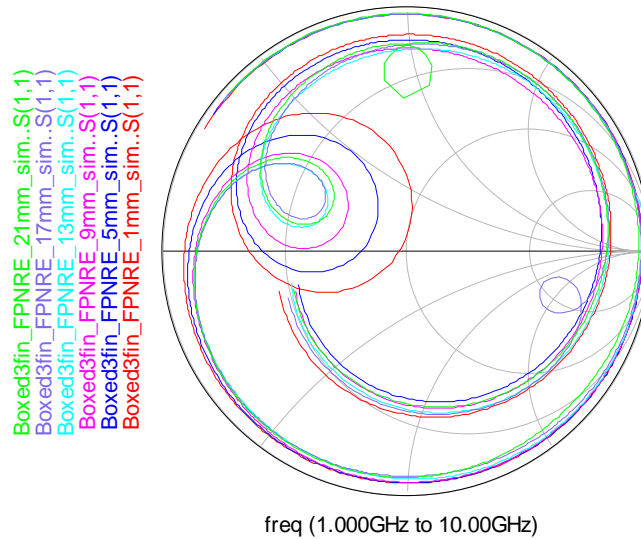


Figure 6-8. S_{11} of boxed heatsink for various fin heights (1 mm to 21.1 mm in 4 mm increments) along the non-radiating edges

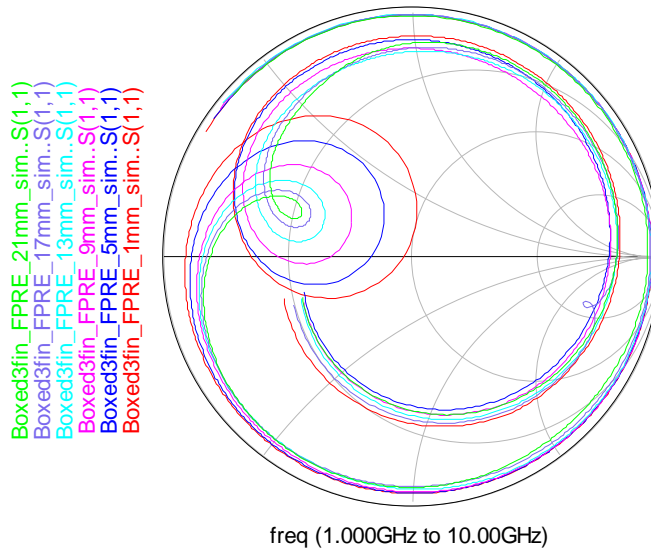


Figure 6-9. S_{11} of boxed heatsink for various fin heights (1 mm to 21 mm in 4 mm increments) along the radiating edges

The radiation efficiency, peak directivity, and peak gain versus fin height are reported in Figure 6-10, Figure 6-11, and Figure 6-12, respectively. Since the resonant frequency is relatively stable over the fin height range, the parameters are reported only at a constant frequency of 5.80 GHz. In Chapter 5, it was noted that in the radiating edge case for the 3-finned heatsink antenna, the radiation efficiency did not increase monotonically for low-fin heights as observed in the non-radiating edge case but instead actually exhibited a decreased in efficiency up to a fin height of 6 mm. From Figure 6-10 it can be seen that the boxed heatsink antenna does not suffer from this behavior and increases monotonically for almost all fin heights shown in both orientations.

The peak directivity and peak gain of the antennas versus fin height are shown in Figure 6-11 and Figure 6-12, respectively. For the non-radiating edge case, the directivity and gain of the boxed and 3-finned heatsink antennas are very similar. However, for the radiating edge case, the boxed heatsink antenna results are quite different from the 3-finned case. The radiation pattern of the 3-finned radiating edge case has two end-fire lobes for certain fin heights. This introduction of the end-fire lobes significantly lowers the directivity and gain leading them to be highly dependent on fin height. However, the boxed heatsink has no end-fire radiation, and the radiation pattern only has a single, broadside lobe (see the 3-D pattern plots in Figure 6-13). The fins no longer act like monopoles. The result is that the peak directivity and gain of the boxed heatsink (non-radiating and radiating edge case) follow more closely to those of the 3-finned non-radiating case which also has a single, broadside lobe as a radiation pattern.

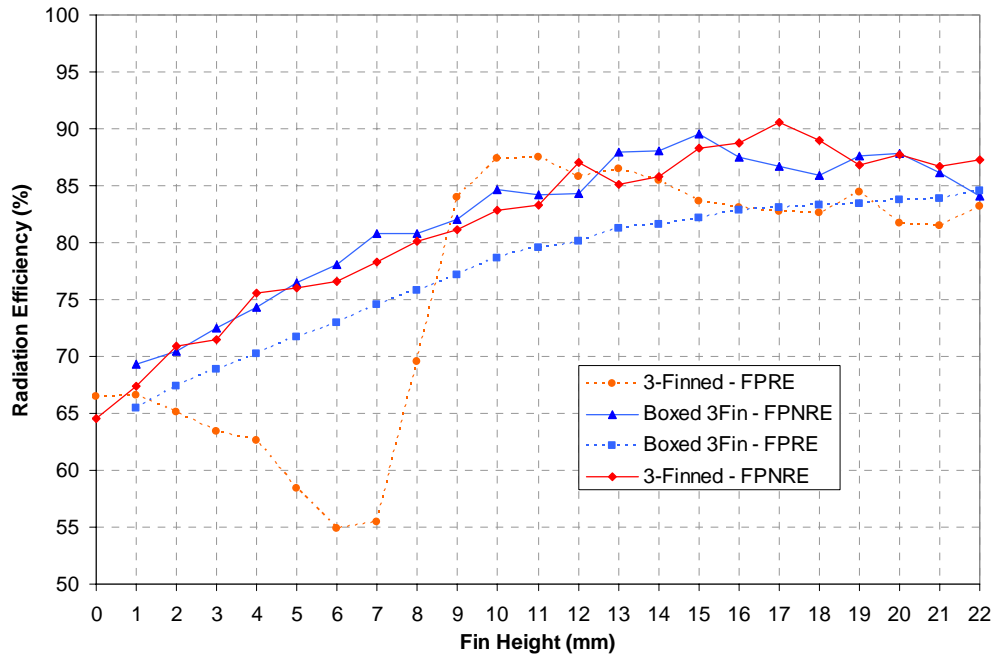


Figure 6-10. Radiation efficiency of boxed heatsink antennas compared to the 3-finned heatsink antennas at 5.80 GHz

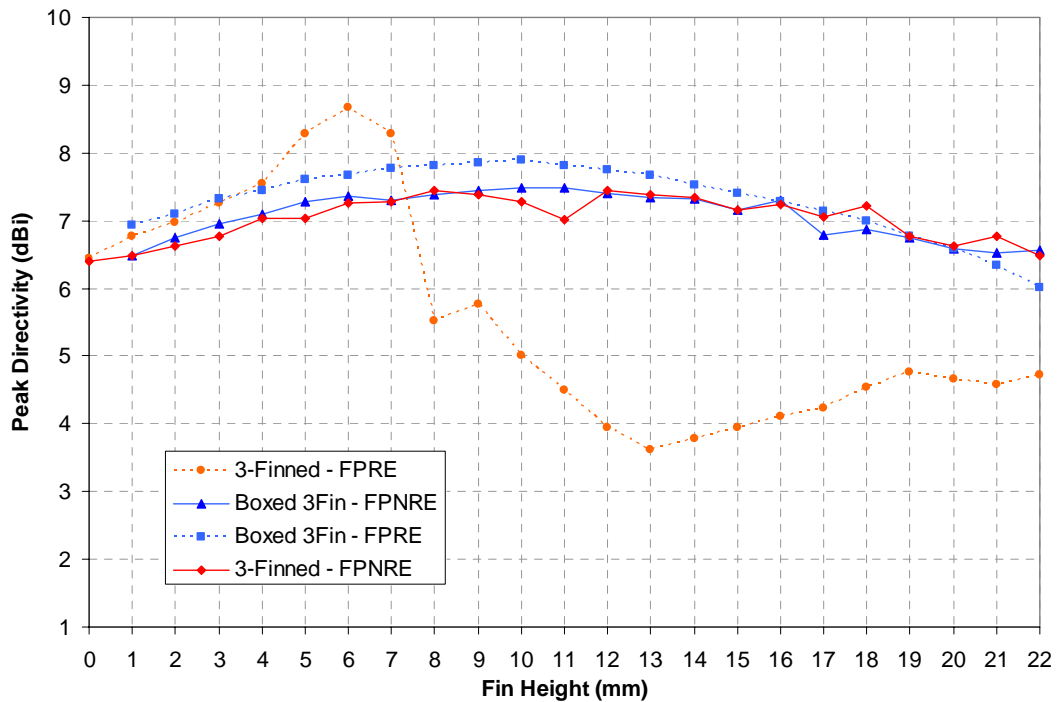


Figure 6-11. Peak directivity of boxed heatsink antennas compared to the 3-finned heatsink antennas at 5.80 GHz

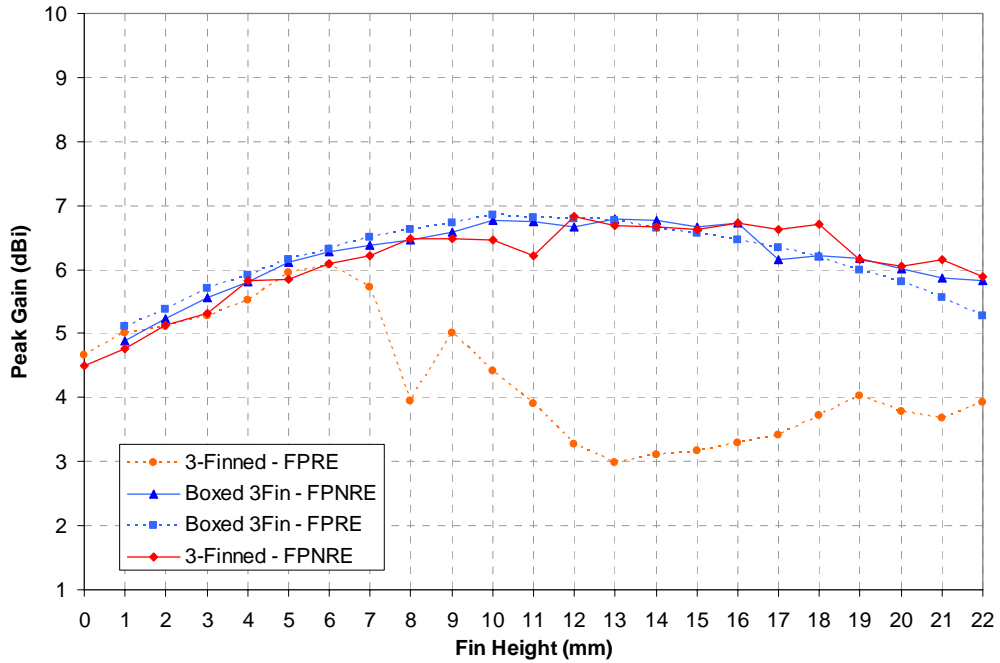


Figure 6-12. Peak gain of boxed heatsink antennas compared to the 3-finned heatsink antennas at 5.80 GHz

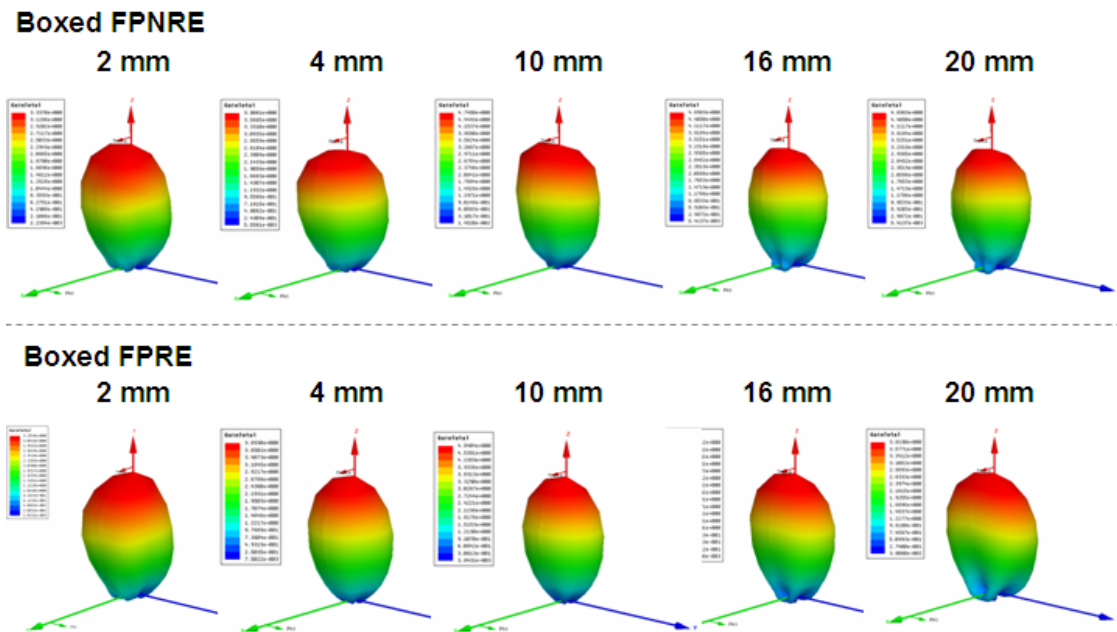


Figure 6-13. Three-dimensional gain patterns of boxed heatsink antenna versus fin height for both fin orientations (FPNRE and FPRE)

6.2.3 Results of Cubic Heatsink Antenna Simulations

The cubic heatsink antenna shown in Figure 6-3 was simulated. Because of its symmetry there is only one orientation. The cubic heatsink antenna exhibits only a single resonance in the 1 to 10 GHz range. The comparison of resonant frequency versus fin height for the cubic antenna and boxed antennas are shown in Figure 6-14. The resonant frequency of the cubic antenna remains between the resonant frequencies of the boxed radiating edge case and boxed non-radiating edge case for all fin heights shown and tracks more closely to the boxed non-radiating edge case.

The radiation efficiency of the cubic antenna versus fin height compared with the efficiency of the boxed heatsink antenna of both orientations is shown in Figure 6-15. The efficiency of the cubic antenna closely tracks that of the boxed heatsink antenna with fins parallel to the non-radiating edges. The directivity and gain of the cubic antenna compared with the other antennas are shown in Figure 6-16 and Figure 6-17, respectively. As with the radiation efficiency, both the directivity and gain of the cubic antenna track closely with those of the boxed antenna with fins parallel to the non-radiating edges.

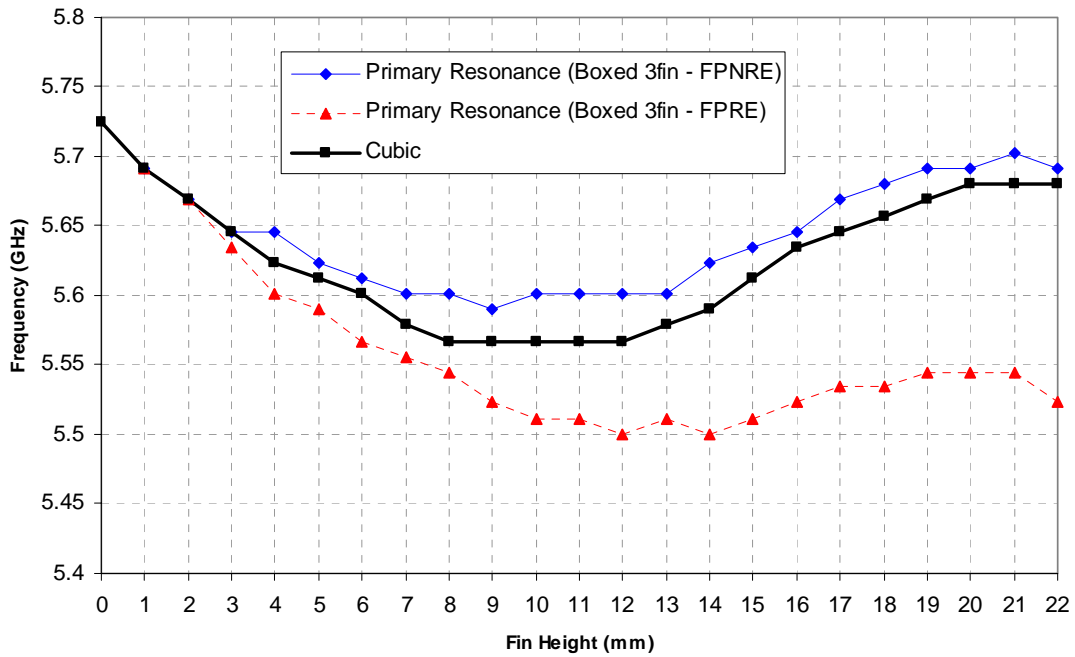


Figure 6-14. Resonant frequencies of cubic heatsink antenna compared to the boxed heatsink antenna primary resonances

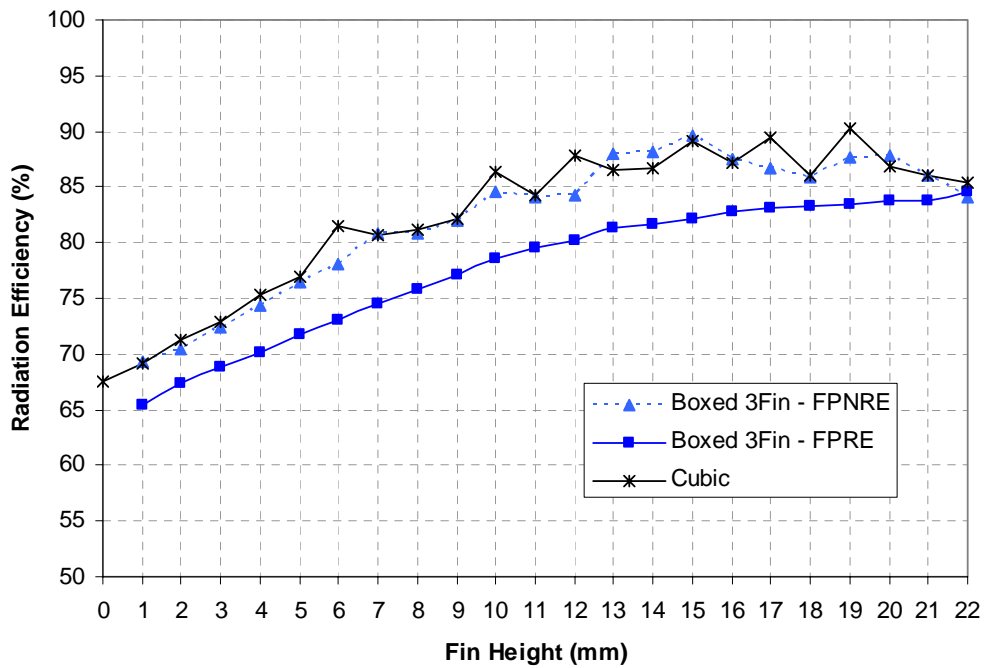


Figure 6-15. Radiation efficiency vs. fin height of cubic heatsink antenna compared with the boxed and 3-finned antennas

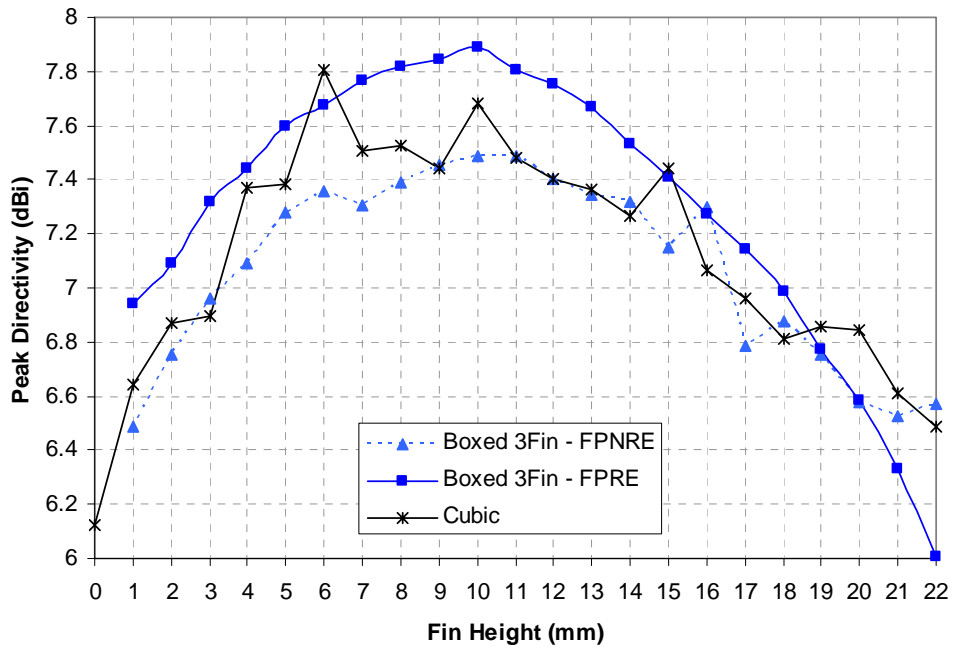


Figure 6-16. Peak directivity vs. fin height of cubic heatsink antenna compared with the boxed 3-finned antennas

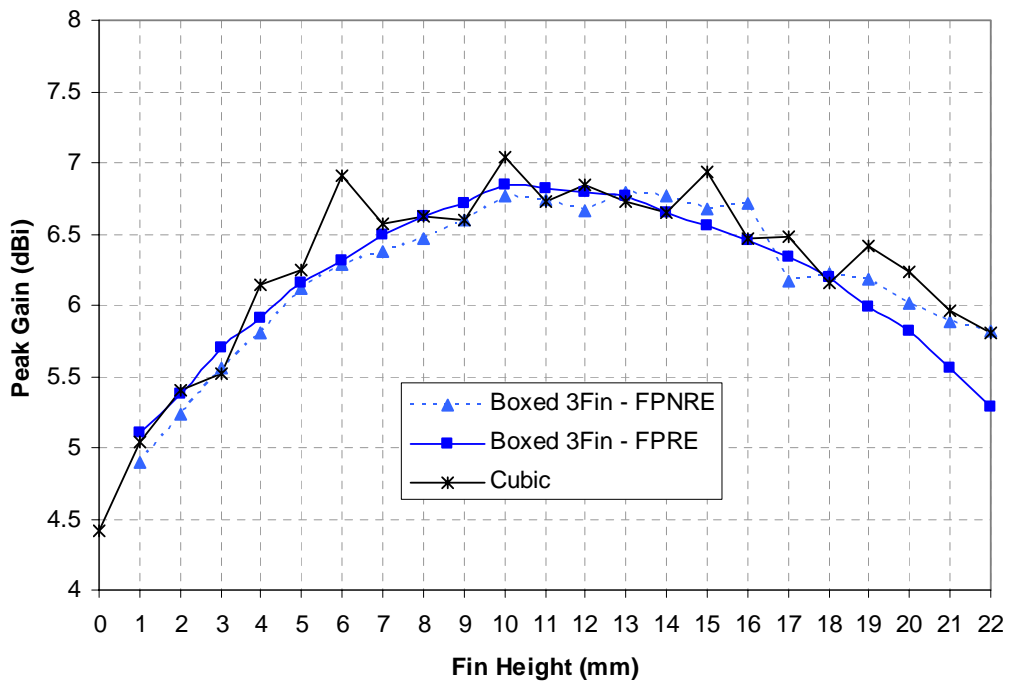


Figure 6-17. Peak gain vs. fin height of cubic heatsink antenna compared with the boxed 3-finned antennas

6.2.4 Summary of Results

The dual-frequency nature of the 3-finned heatsink was suppressed by the boxed heatsink for fin heights below 16 mm and by the cubic heatsink for all fin heights shown. The boxed heatsink of the FPNRE orientation showed very little change compared with the 3-finned FPNRE case. The return losses were nearly identical aside from the fact that the boxed heatsink suppressed the alternate resonance that was present with the 3-finned version. With nearly identical return losses, the primary resonances of the boxed and 3-finned heatsink antennas are also almost identical. Additionally, the radiation patterns and antenna parameters for the boxed and 3-finned FPNRE heatsink antennas are very similar.

In contrast, the top plate of the boxed heatsink antenna in the FPRE orientation leads to significantly different results than the 3-finned counterpart. In this case, the boxed heatsink also removed the alternate resonances that were present with the 3-finned version. Moreover, the primary resonance of the boxed heatsink shows little variation over fin height. This is considerably different than the 3-finned FPRE case whose primary resonance exhibited substantial change with fin height. The radiation patterns are also affected by the top plate of the boxed heatsink in this orientation. The radiation patterns of the boxed FPRE heatsink consist of only a broadside lobe in contrast to the additional end-fire lobes of the 3-finned FPRE heatsink antenna. Another important difference between the boxed FPRE heatsink and the 3-finned FPRE heatsink deals with the radiation efficiency. The boxed FPRE heatsink did not suffer from the initial decrease in efficiency for fin heights from 0 mm to 6 mm as did the 3-finned FPRE case.

The cubic heatsink antenna also suppressed the alternate resonances across the entire fin height range shown. The cubic heatsink antenna had simulation results more consistent with the boxed FPNRE heatsink antenna than the boxed FPRE case. By a similar argument that the 3-

finned FPFE heatsink and the pin-fin heatsink antenna prohibit longitudinal fin currents, both the cubic and boxed FPNRE heatsink antennas allow longitudinal fin currents.

6.3 Conclusion

A boxed heatsink structure was introduced and compared with the 3-finned heatsink antenna discussed previously in Chapter 5. This 3-finned heatsink antenna provided efficiency enhancement, increases or decreases in directivity and gain depending on the fin height and orientation, and also dual-frequency operation in addition to the antenna's built-in thermal management capabilities. However, dual-frequency operation is not always desired since a single frequency antenna has inherent filtering outside of its operating band. Thus the boxed heatsink antenna provides one solution for a high-efficiency, bandwidth-enhanced, single-frequency antenna while simultaneously providing thermal management. However, the top plate of the boxed heatsink antenna may reduce the airflow and degrade the thermal performance.

CHAPTER 7
INTEGRATED POWER AMPLIFIER AND HEATSINK ANTENNA MODULE

7.1 Introduction

Previous discussions claim the heatsink antenna as a dual-function structure: a radiator of both thermal and electromagnetic energy. However, the heatsinks were not being used for their fundamental purpose: as heatsinks. In order to validate the idea, it is necessary to successfully integrate a power amplifier with a heatsink antenna while simultaneously using the heatsink as a thermal mass to protect the power amplifier. In this manner, the use of a heatsink as an antenna was shown to be a practical and sound solution. This chapter introduces the integrated PA and heatsink antenna module and presents the measurement results.

7.2 Description

A high power linear amplifier (RF2126) from RFMD was used for the power amplifier/heatsink antenna (PA/HSA) integration. The PA has an SOIC-8 package with a slug on the backside of the chip as the chip ground which is also used as a thermal sink. The PA has a maximum RF output power of 1.3 Watts (approximately 31 dBm) and a gain of 12 dB. The maximum continuous dissipated power is 1.3 Watts.

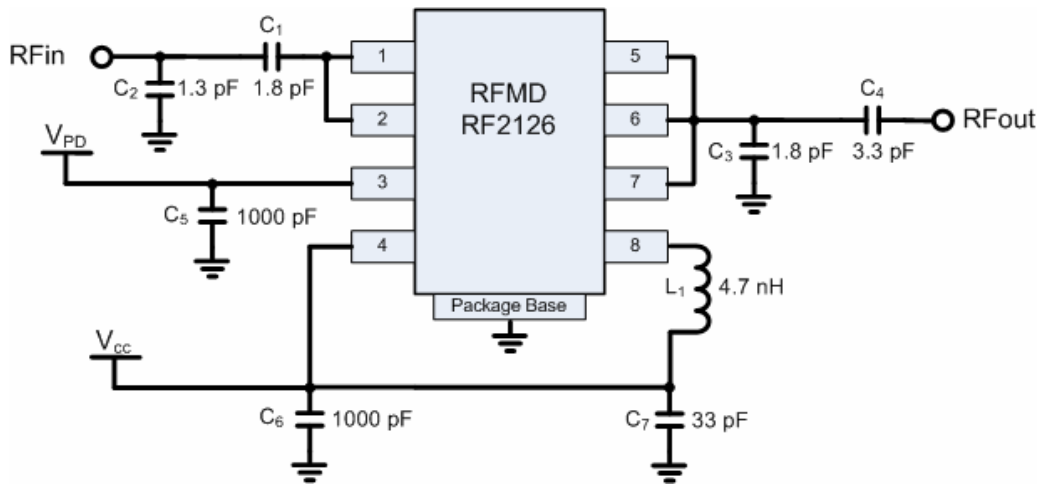


Figure 7-1. Power amplifier schematic for 2.45 GHz operation [Dat]

The circuit schematic designed to operate at 2.45 GHz is shown in Figure 7-1. Input and output matching networks are required externally and are shown in the figure (C_1 , C_2 , C_3 and C_4). All passive elements in the circuit were realized using surface-mount components. The circuit was fabricated on a single-layer FR4 PCB using the same layer for both the signal traces and the ground plane. The layout for the single-layer circuit is shown in Figure 7-2 where the gray traces and surrounding gray field represent the ground plane. All other traces are shown in red.

The SMA connectors and the IC are shown in green. Underneath the IC, the ground plane is connected to the package ground. As shown in the figure, a hole is cutout in the ground plane directly beneath the IC. This is a thermal via (not electrically conductive) to draw heat away from the IC to the heatsink on the opposite side of the PCB. Duralco 128 thermal epoxy was used for the thermal via. The thermal via is illustrated more clearly in Figure 7-3.

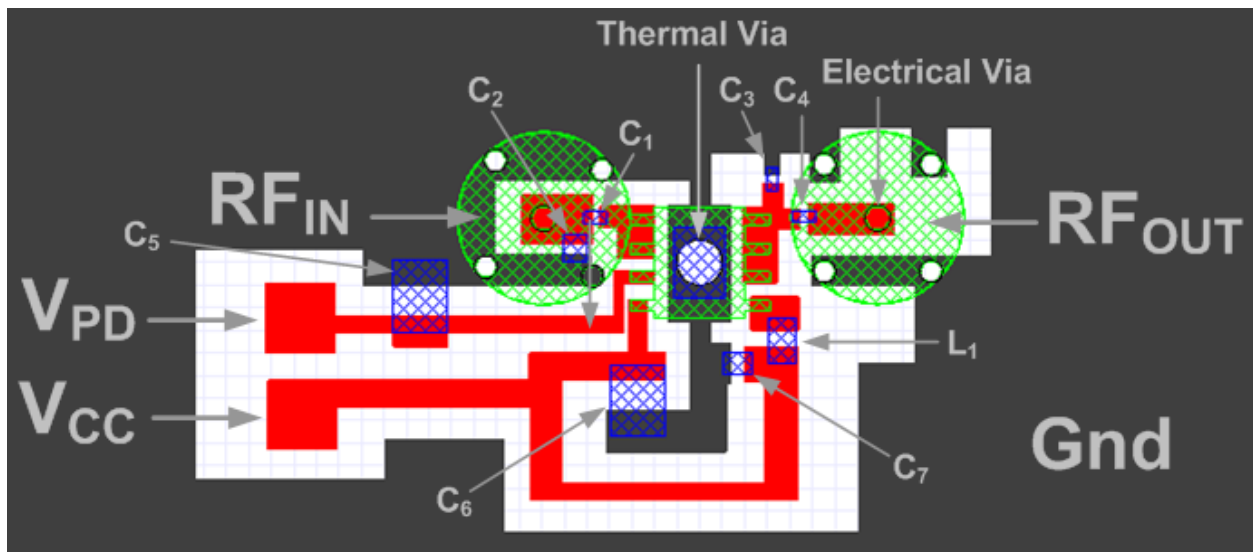


Figure 7-2. Layout of power amplifier circuit

The thermal via is located directly underneath the IC to efficiently transfer heat from the chip to the heatsink through the PCB. The electrically-insulating property of the thermal via removes the added complexity of the antenna (heatsink) being shorted to ground. Certainly, shorting pins have been shown to be beneficial to the performance of patch antennas [Gar2, Wat2]. However, removing the short also removes the added complexity for this initial design (later designs may include an electrically-conductive thermal via to exploit the benefits of a shorting pin). A separate electrical via is used to feed the antenna as shown in the illustration. This probe feed was constructed using a vertical-mount SMA connector. In this manner, the pin from the SMA connector provides a via while also allowing direct measurement of the antenna in circuit. The output matching circuit was removed before the antenna was measured to isolate the antenna from the rest of the circuit in order to achieve an accurate measurement.

Table 7-1. Thermal conductivity of materials

Material	Thermal conductivity (W/m-K)
FR4	0.27
Thermal epoxy	4.33
Copper	401
Aluminum	237

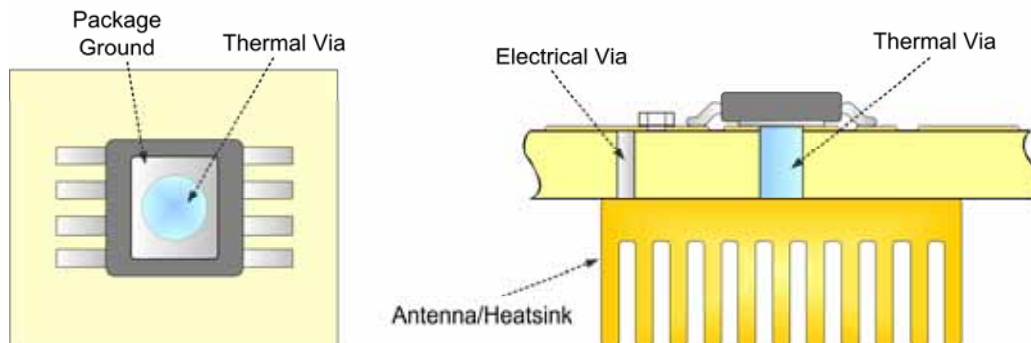


Figure 7-3. Diagram showing top view (left) and side view (right) of electrical and thermal vias (note: not to scale, heatsink rotated 90 degrees for illustrative purposes)

The backside (or circuit side) of the module is shown in Figure 7-4. The backside serves as the ground plane for the antenna in addition to containing the circuit in the same layer. The

SMA connector at the output (on the right in Figure 7-4) is tilted since part of the output matching circuit is located underneath the connector (as shown in Figure 7-2). This allows removal and replacement of the surface-mount capacitor to facilitate direct measurement of the antenna.

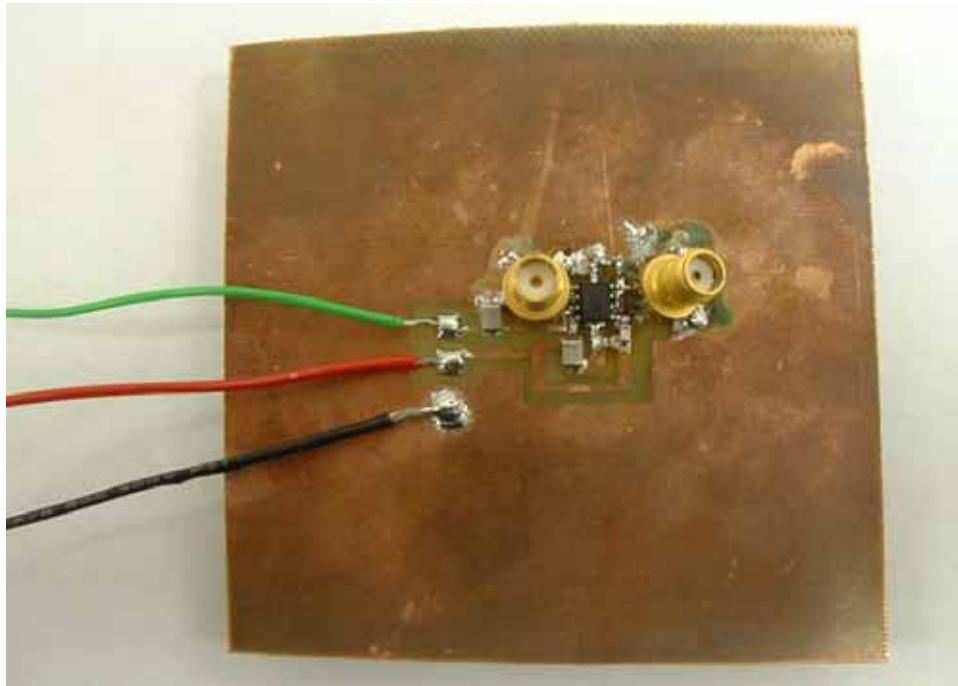


Figure 7-4. Backside of heatsink antenna/PA module showing circuit

The topside of the module is shown in Figure 7-5. This side of the module has no trace layer since the heatsink antenna is probe-fed and the bottom of the heatsink replaces the patch. The input impedance of the antenna is determined by the placement of the feed-point. Since the feed-point is fixed, the input impedance is determined by the placement of the heatsink with respect to the probe. This placement was determined experimentally to achieve an acceptable input reflection coefficient at the operating frequency of the PA. The placement was also held to the constraint of having the thermal via roughly centered underneath the heatsink for more

efficient heat transfer. The heatsink was fixed and electrically connected to the probe with silver epoxy.

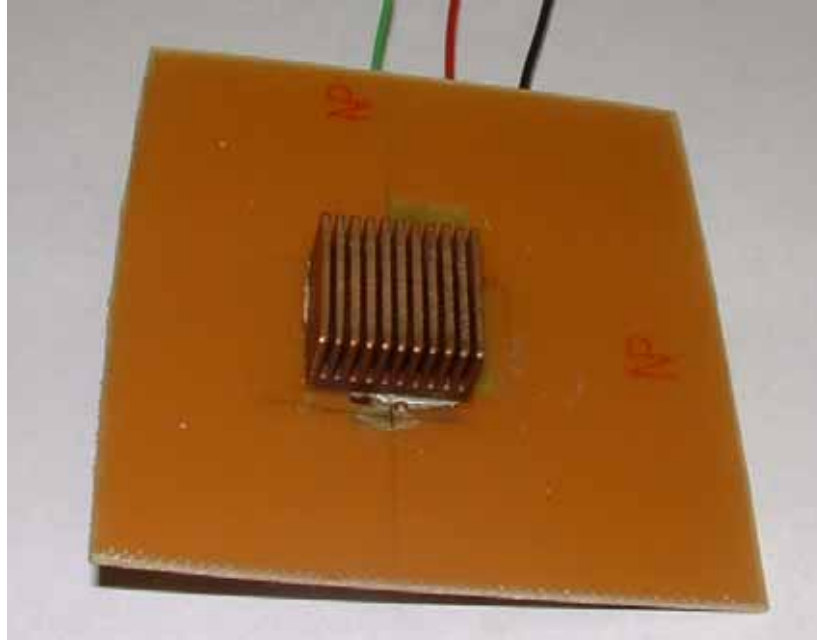


Figure 7-5. Topside of heatsink antenna/PA module

7.3 Results

The design of the module allowed the antenna to be measured in-circuit using the SMA connector following the output matching network of the PA. The components making up the output matching network (capacitors C_3 and C_4 in Figure 7-1) were removed prior to the antenna measurement to isolate the antenna from the PA. The input reflection coefficient from 1 to 5 GHz for the antenna is shown in Figure 7-6. The antenna demonstrates multi-band performance over the 1 to 5 GHz frequency range shown. However, for this application the return loss at the operating frequency of the PA was most important. At 2.45 GHz, the magnitude of S_{11} is -12.3 dB (or 94.1% of the power incident on the antenna is accepted into the antenna as shown below).

$$\frac{P_{acc}}{P_{inc}} = 1 - |\Gamma|^2 = 1 - |S_{11}|^2 = 1 - \left(10^{(-12.3/20)}\right)^2 = 0.941 \quad (7-1)$$

$$\text{Mismatch losses for heatsink antenna} = 10 \log_{10} \left(\frac{1}{0.914} \right) = 0.26 \text{ dB} \quad (7-2)$$

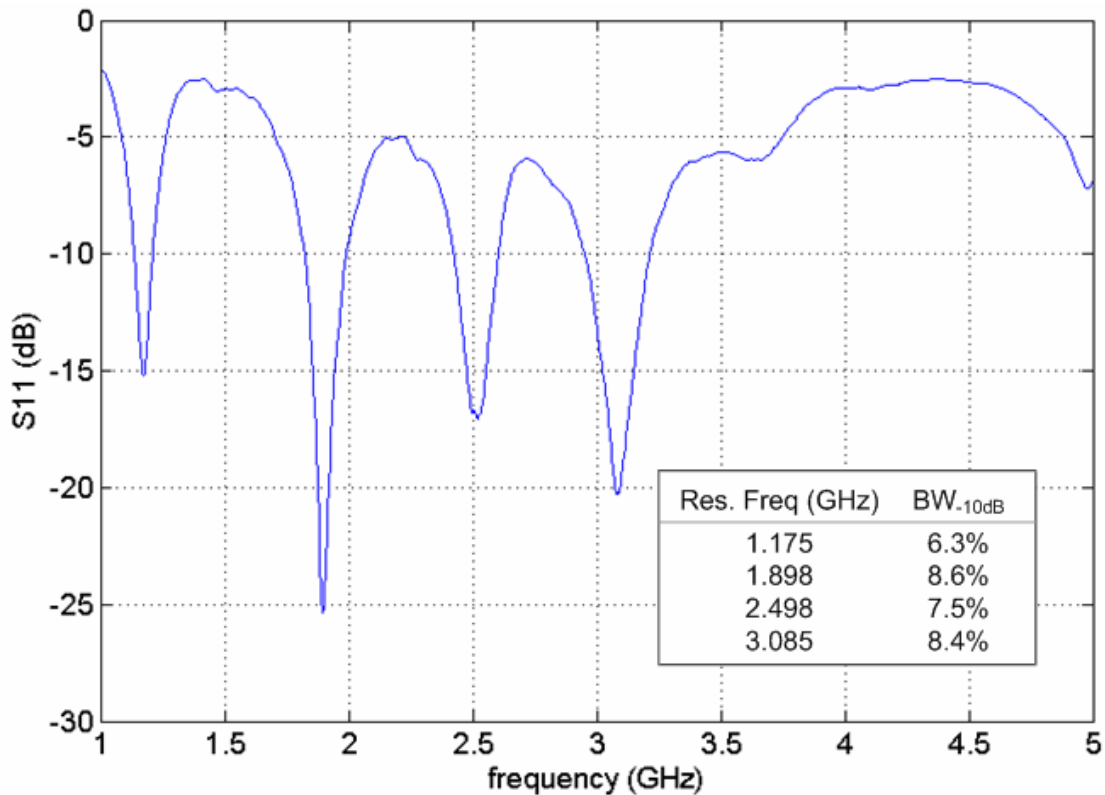


Figure 7-6. Measured return loss of heatsink antenna

Next, the peak gain of the antenna on the PA/heatsink antenna module was measured by the absolute method [Kra] using a signal generator, a spectrum analyzer, and a receiving patch antenna with a known gain as shown in Figure 7-7. The output matching network components were replaced on the PA/heatsink antenna module to connect the output of the PA to the antenna. Table 7-2 reports the parameters used to perform the measurements. The PA was driven with 19 dBm of RF input power at 2.45 GHz, a V_{CC} of 3.6 volts and 3.0 volts on the power control (PD) pin. At this bias point and input power level, the PA outputs 27 dBm of RF output power. The maximum bias for this PA is a V_{CC} of 6.0 volts with an RF input power of 19 dBm. This bias and drive level would enable the PA to operate at its maximum output power (31 dBm).

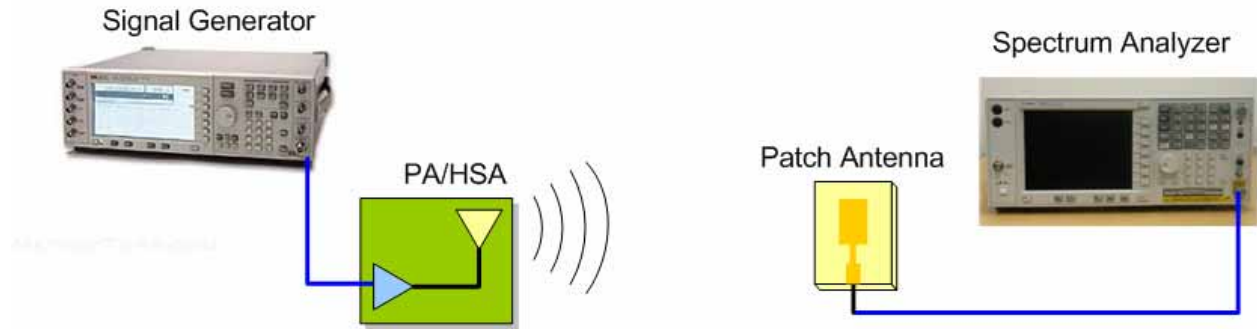


Figure 7-7. Measurement setup for the PA/HSA testing

Table 7-2. Parameters used in gain measurement

Parameter	Value
Frequency (GHz)	2.45
P_{in} (to PA) in dBm	19
V_{CC} (V)	3.6
V_{PD} (V)	3.0
P_{out} (dBm) @ given bias and P_{in}	27
G_r (patch antenna) (dBi)	4.46
Cable loss (dB)	0.5
Heatsink antenna mismatch loss (dB)	0.26
Patch antenna mismatch loss (dB)	0.21

The measured results for the gain experiment are reported in Table 7-3 at different ranges (distance between the transmit and receive antennas). The antenna gain is then calculated from a modified version of the Friis equation to include losses as shown in Eq. 7-3.

$$G_t (dBi) = 10 \log_{10} \left[\left(\frac{4\pi R}{\lambda} \right)^2 \right] + P_r (dBm) - P_t (dBm) + G_r (dBi) + losses (dB) \quad (7-3)$$

where P_r is the received power, P_t is the transmitted power ($P_t = P_{out} = 27$ dBm in this case), G_r is the gain of the receiving antenna (4.46 dBi in this case), and G_t is the gain of the transmitting antenna (the heatsink antenna on the PA/HSA module).

The losses in Eq. 7-3 include a measured cable loss of 0.5 dB and mismatch losses for both antennas. The mismatch loss for the heatsink antenna is 0.26 dB (as shown in Eq. 7-2). The input reflection coefficient of the patch antenna (receiving antenna) is -13.17 dB. Using Eqs. 7-1 and 7-2, this equates to a mismatch loss of 0.21 dB for the receiving antenna. These three losses are summed together to create the last term in Eq. 7-3. The received power at various ranges is reported in Table 7-3. The heatsink antenna gain is calculated from Eq. 7-3 and is also reported in Table 7-3. The gains are peak gains as the measurements were performed with both antennas oriented in the direction of maximum radiation (broadside to the dielectric).

Table 7-3. Measured received power at various distances from PA/HSA module with corresponding calculated peak antenna gain

Distance (R) (ft.)	P_r (dBm) (upper bound)	P_r (dBm) (lower bound)	G_t (dBi) (upper bound)	G_t (dBi) (lower bound)
2	-20.9	-21.4	11.69	11.19
4	-25.2	-25.9	13.41	12.71
5	-27.5	-27.9	13.05	12.65
8	-32.5	-32.5	12.13	12.13
10	-33.9	-34.3	12.67	12.27

The PA operated without incident at the input drive and bias levels stated in Table 7-2 for the gain measurement. Next, the maximum drive and bias levels were applied to the PA in order to measure the heatsink and package temperatures. The temperatures of the chip and the heatsink were measured with the power amplifier at biased at $V_{CC} = 6.0$ V and with an RF input drive level of 19 dBm. The chip package temperature was 62°C and the heatsink temperature was 43°C. The ambient temperature was 23°C. However, at this maximum drive level the PA eventually burnt out within a couple of minutes. Therefore, the material used for the thermal via is not a good choice and has a low thermal conductivity as shown in Table 7-1. Despite the fact that the thermal epoxy has a thermal conductivity 16 times greater than that of the FR4 substrate, the thermal conductivity is still not high enough to efficiently transfer enough heat away from

the PA to the heatsink at the maximum drive levels. However, at the drive level used to measure the gain, the heatsink is not only being used as an antenna, but it is also being used in its traditional manner. To the author's knowledge this is the first time a heatsink has been used both as a heatsink for a power amplifier while at the same time being used as an antenna driven by the PA.

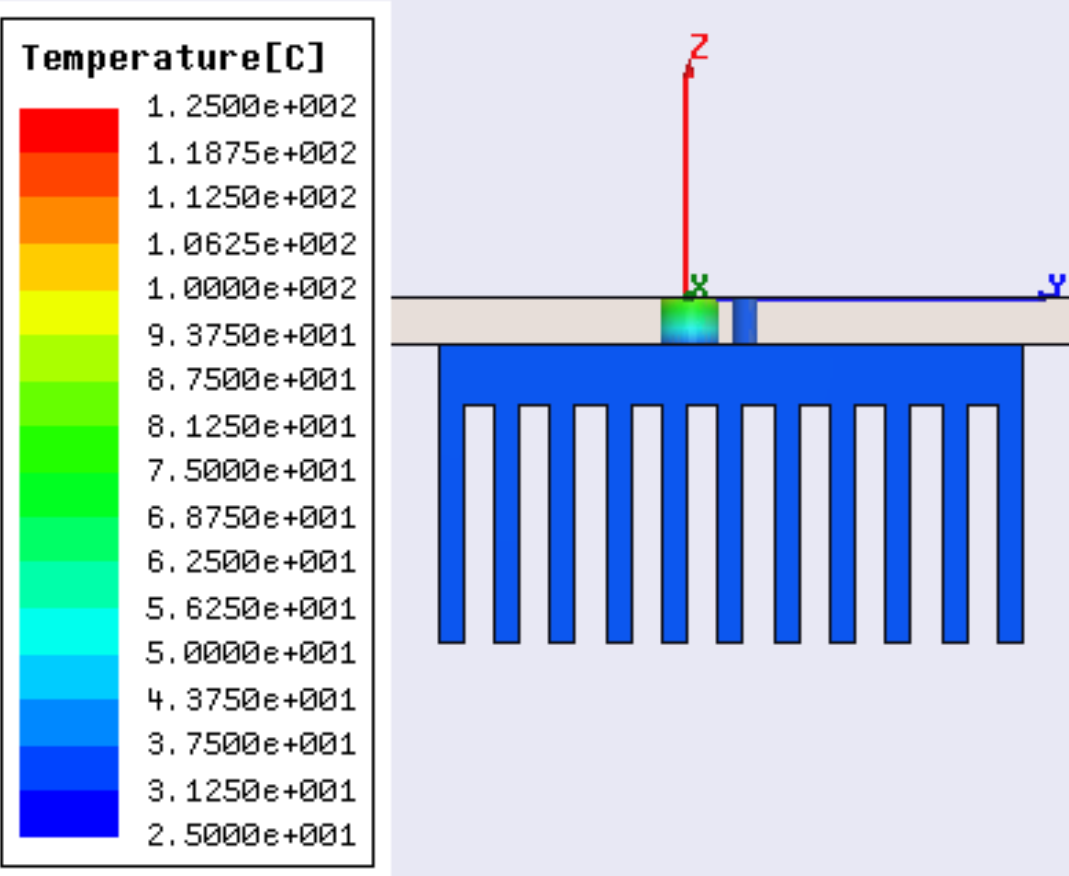


Figure 7-8. Simulated temperature distribution in the heatsink, thermal via, and electrical via at an output power level of 27dBm

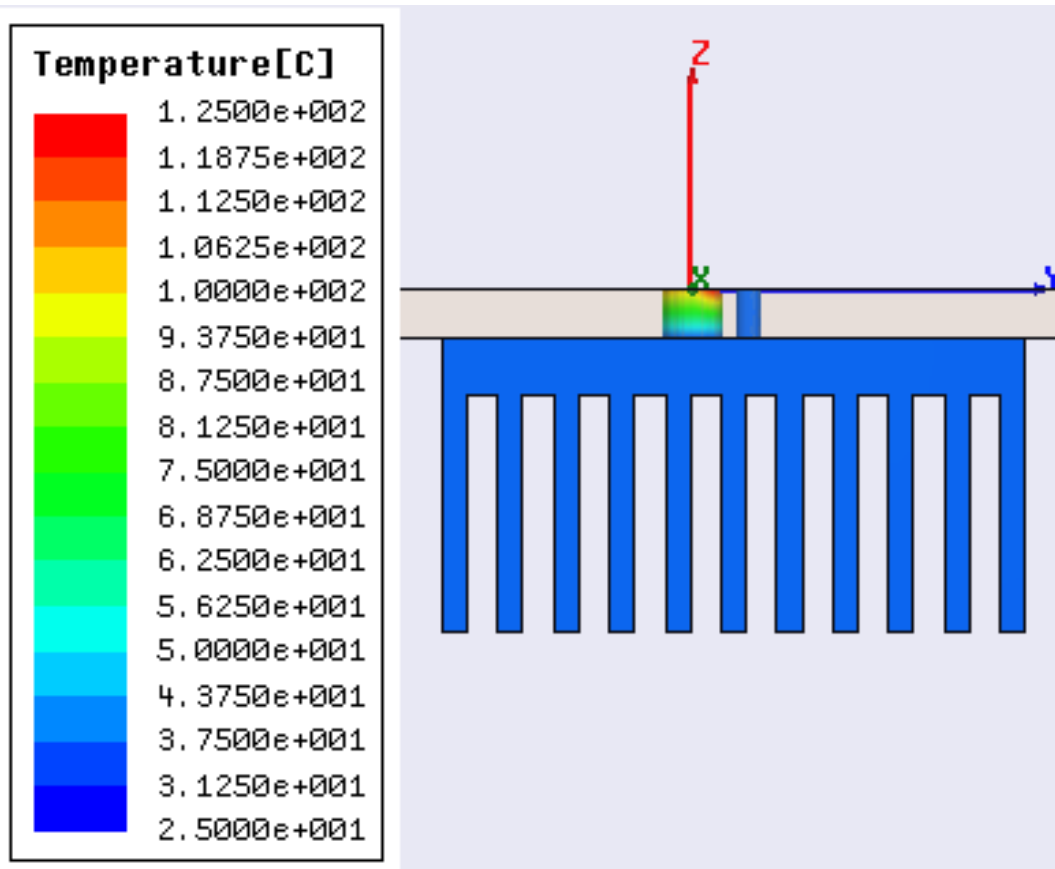


Figure 7-9. Simulated temperature distribution in the heatsink, thermal via, and electrical via at an output power level of 31dBm

Thermal simulations were performed in Ansoft ePhysics by Joaquin Casanova, another student in the RFSOC lab. The thermal simulation results are shown in Figure 7-8 and Figure 7-9 for PA output powers of 27 dBm and 31 dBm, respectively. Improvements in the thermal performance may be achieved by using a material with a higher thermal conductivity for the thermal via. It is also possible to use a metal as the thermal via such as copper or aluminum. In this case the thermal conductivity would be high enough to efficiency transfer the heat. However, the sink on the backside of the PA is also the ground. Using a metal as the thermal via material would short the heatsink to ground. This can actually be beneficial as shorting pins (or posts) have been shown to improve antenna performance [Gar2, Wat2]. Another option is to use

a substrate other than FR4 that has a higher thermal conductivity or a thinner substrate; however, a thinner substrate may reduce the radiation efficiency.

7.4 Conclusion

An integrated PA/heatsink antenna module was successfully fabricated and measured. This validates the idea of using the PA's heatsink as the antenna and vice-versa and is the first reported integration of a PA and a heatsink antenna. An antenna gain of approximately 12 dBi was achieved using the PA's heatsink as the antenna. Using a lossy FR4 substrate, this is a considerable improvement in gain over the traditional patch antenna (patch antenna gain = 4.46 dBi). Normally, arrays must be used to achieve high gains with patch antennas. Though the profile of the heatsink antenna is larger than a patch, the planar size is much smaller than that of an array; therefore, the heatsink antenna demonstrates an alternative solution to achieving a high gain.

The device failed at the maximum drive and bias level suggesting that the thermal via was not sufficient at the maximum power. Therefore, this study reveals that the thermal performance needs to be improved. Possible improvements are using a higher thermal conductivity material as the thermal via or possibly using a type of metal which would create a shorting pin as well. Another option is to use a substrate other than FR4 that has a higher thermal conductivity or a thinner substrate.

CHAPTER 8 SUMMARY AND FUTURE WORK

8.1 Summary

The use of a heatsink as an antenna was validated. 2.4 GHz pin-fin and 5.8 GHz extruded-fin heatsink antennas were designed, simulated, fabricated and measured. The results show significant increases in radiation efficiency for both cases. This is important since one application of the heatsink antenna is to use it as the antenna in a high-power transmitter in addition to a heatsink for the power amplifier. Microwave power amplifier design is a balancing act of output power, efficiency and linearity; and thus the corollary being that any increase in the antenna's radiation efficiency relaxes the design constraints for the PA.

Bandwidth enhancement was also achieved in the 2.4 GHz and 5.8 GHz heatsink antennas. Poor impedance bandwidth is one of the fundamental limitations of patch antennas. The heatsink antennas in Chapter 3 and 4 show significant increases in bandwidth allowing the antenna to operate over a wider range or band of frequencies with minimal input reflection.

The heatsink antennas in Chapter 3 and 4 also show increased gain over their basic patch counterparts. The consequence of which can be observed in the Friis equation from Chapter 2 by a reduction in free-space path losses. More power can be received, or less power can be transmitted in order to achieve a certain received power determined by the system specifications.

In addition to the fabricated 2.4 GHz and 5.8 GHz antennas of Chapter 3 and 4, ten heatsink antennas of different fin heights and orientations were fabricated and measured to validate the simulations in Chapter 5. Chapter 5 explored the effects of fin height and orientation in simulation and measurement on the 3-finned heatsink antenna properties and on multiple-fin and pin-fin heatsink antennas in simulation. The 3-finned structure creates a dual resonance (primary and alternate) for both radiating and non-radiating edge cases which allows the antenna

to be a dual-band antenna. Furthermore, the results showed that the alternate resonant frequency can be used to reduce the planar size of the patch antenna, since in the radiating edge case this frequency is significantly lowered by the heatsink from that of a basic patch antenna of the same dimensions.

The results also show that the orientation is important. For the radiating edge cases the primary resonant frequency changes significantly versus fin height, while the primary resonant frequency is relatively independent of fin height in the non-radiating edge cases. This may be important since the fin height could be increased or decreased depending on thermal resistance requirements without affecting the resonant frequency dramatically in the non-radiating edge case.

The 2-finned results tracked closely with the 3-finned results demonstrating that the center fin has little effect while the outer two fins play the dominant role in changing the antenna parameters versus fin height. However, the center fin was shown to be the cause of the alternate resonance in the non-radiating edge case, and removing the center fin makes the antenna a single-frequency antenna.

The radiation efficiency is also affected by the fin height and orientation as the results show in Chapter 5. The efficiency increases monotonically with fin height in the non-radiating edge case. However, the radiating edge case initially shows a decrease in efficiency as the fin height increases over the lower fin height range. Increasing the fin height further causes a discontinuous jump in efficiency to a level comparable to that of the non-radiating edge case. Increasing the number of fins or the fin thickness was shown to help reduce the effect of decreasing efficiency for the lower fin heights in the radiating edge case.

The effect of fin height on directivity and gain on the extruded-fin heatsink antennas is very different depending on the fin orientation. The directivity and gain both increase and decrease significantly for the radiating edge cases in Chapter 5. For the non-radiating edge case, however, the directivity changes very little with fin height. The reason for the large variation in directivity (and gain) in the radiating edge case is due to a significant change in the radiation pattern while the pattern changes very little in the non-radiating edge case. Thus the directivity/gain can be increased or decreased depending on the application. The advantage of increasing the gain can be seen from the Friis equation – less power must be transmitted. The transmitter could transmit less power to achieve the same received power by using a higher gain antenna. Accordingly, the power amplifier output power specification can be reduced dramatically. This is important since every dB of PA output power is hard-earned by the PA designer. Moreover, the reduction in output power can reduce or increase the thermal dissipation ($P_{diss} = P_{in} + P_{DC} - P_{RF}$) of the power amplifier depending on the drain efficiency ($\eta = P_{RF}/P_{DC}$) or power-added efficiency ($PAE = (P_{RF} - P_{in})/P_{DC}$). If the thermal dissipation is decreased, then this may be accompanied by a reduction in fin height, or vertical size of the antenna, since the thermal resistance requirement of the heatsink would be relaxed in this case giving a lower profile heatsink antenna.

Chapter 6 introduced the boxed heatsink antenna and cubic heatsink antenna. Results show that the boxed structure suppresses the dual-frequency nature of the 3-finned heatsink structure and also demonstrates an improvement in radiation efficiency over the 3-finned version. Bandwidth enhancement was also shown to be possible if proper input matching is designed for each specific fin height. The cubic antenna results matched very closely with the boxed antenna results (especially with fins parallel to the non-radiating edges) indicating that the

outer fins play the dominant role with this orientation and that fields within the boxed structure have little effect on the antenna parameters.

Furthermore, Chapter 5 demonstrated that the radiation pattern can be changed significantly and controlled by the fin height and orientation of the heatsink with the 3-finned antenna. With this structure, two- and three-lobe gain patterns were shown in addition to the traditional patch antenna broadside pattern. Chapter 6 demonstrated that the boxed antenna maintains the radiation pattern of a traditional patch antenna even at orientations and fin heights that created the two- and three-lobe patterns with the 3-finned antenna. Thus, the radiation pattern can be controlled by the heatsink parameters.

Chapter 7 reported the results of integrating a heatsink antenna with a commercial power amplifier to demonstrate the concept. The integration was successful and the heatsink provided an antenna gain of approximately 12.6 dBi while simultaneously being used to dissipate heat from the power amplifier. To the author's knowledge, this was the first time a power amplifier and a heatsink antenna have been integrated.

8.2 Future Work

The heatsink antenna design lies in the three-dimensional domain; and thus, more complex heatsink structures certainly exist but are yet to be studied. A study on the effects of electrically-connected versus non-electrically-connected heatsinks may also reveal interesting results. Heatsink antennas were developed at the board level. A next logical step would be to apply the concept of the heatsink antenna to the 3-D VLSI process developed by the University of Arkansas [Sch] which forms copper posts by electroplating. With this process, 3-D copper posts can be developed on-chip which may behave like a pin-fin heatsink antenna. The results presented in this dissertation laid the groundwork for how heatsinks behave as antennas over a substrate. Next, these principles can be applied when studying the performance of the heatsink

antenna when integrated with a 3-D SOC package. Also, thermal simulations should be performed to accompany the electromagnetic research.

LIST OF REFERENCES

- [And] T. J. Anderson, F. Ren, L. Covert, J. Lin, and S. J. Pearton, "Thermal Simulations of three-dimensional integrated multichip module with GaN power amplifier and Si modulator," *Journal of Vacuum Science & Technology B*, Vol. 24, No. 1, pp. 284-287, Jan./Feb. 2006.
- [Bal] C.A. Balanis, *Antenna Theory: Analysis and Design*. New York, NY: John Wiley & Sons, Inc., 1997, 3rd Edition.
- [Cas] M. Casto, "AlGaIn/GaN HEMT Temperature-Dependent Large-Signal Model Investigation, Generation, and Simulation," A thesis submitted to Wright State University, 2005.
- [Cha] C.-T. Chang, C.-Y. Chang, and J.-P. Sheu, "BlueCube: constructing a hypercube parallel computing and communication environment over Bluetooth radio system," *Proceedings of the 2003 International Conference on Parallel Processing*, pp. 447-454, 2003.
- [Cov] L. Covert and J. Lin, "Simulation and Measurement of a Heatsink Antenna: A Dual-Function Structure," *IEEE Transactions on Antennas and Propagations*, Vol. 54, No. 4, pp. 1342-1345, Apr. 2006.
- [Cul] D. E. Culler, J. P. Singh, and A. Gupta, *Parallel Computer Architecture: A Hardware/Software Approach*. San Francisco, CA: Morgan Kaufmann Publishers, Inc., 1999, pp. 764-778.
- [Cur1] W. R. Curtice, "User's guide for the C_FET Model for Agilent's Advanced Design Simulator," W. R. Curtice Consulting, 2005.
- [Cur2] W.R. Curtice and M. Ettenberg, "A Nonlinear GaAs FET Model for Use in the Design of Output Circuits for Power Amplifiers," *IEEE Transactions on Microwave Theory and Techniques*, Vol. MTT-33, pp. 1383-1394, December 1985.
- [Das] S.K. Das and T. Roy, "An investigation on radiated emissions from heatsinks," *IEEE International Symposium on Electromagnetic Compatibility*, Vol. 2, pp. 784-789, Aug. 24-28, 1998.
- [Dat] Datasheet: "RF2126 High Power Linear Amplifier," RFMD, 2006.
- [Dol] A. Dolente, U. Reggiani, and L. Sandrolini, "Comparison of radiated emissions from different heatsink configurations," *IEEE 6th International Symposium on Electromagnetic Compatibility and Electromagnetic Ecology*, pp. 49-53, Jun. 21-24, 2005.

- [Gar1] R. Gardelli, G. La Cono, and M. Albani, "A Low-Cost Suspended Patch Antenna for WLAN Access Points and Point-to-Point Links," *IEEE Antennas and Wireless Propagation Letters*, Vol. 3, No. 1, pp. 90-93, Jan. 2004.
- [Gar2] R. Garg, P. Bhartiet, I. Bahl, and A. Ittipiboon, *Microstrip Antenna Design Handbook*. Norwood, MA: Artech House, Inc., 2001, p. 285.
- [Geo] R. Georgerian and M. I. Montrose, "Product Safety and the Heat Sink – Dilemma of Minimizing Radiated Emissions and Maximizing Thermal Cooling," *2003 International Symposium on Electromagnetic Compatibility*, Vol. 1, pp. 134-137, Aug. 2003.
- [Het] K. Hettak, G. Y. Delisle, and M. G. Stubbs, "A new type of dual frequency CPW-coupled patch antenna configurations," *2001 IEEE Antennas and Propagation Society International Symposium*, Vol. 3, pp. 386-389, July 8-13, 2001.
- [Kim1] Y. Kim, N.J. Farcich, S.-C. Kim, S. Nam, P.M. Asbeck, "Size reduction of microstrip antenna by elevating centre of patch," *Electronic Letters*, Vol. 38, Issue 20, pp. 1163-1165, Sept. 26, 2002.
- [Kim2] Y. Kim, G. Y. Lee, and S. Nam, "Efficiency Enhancement of Microstrip antenna by Elevating Radiating Edges of Patch," *Electronics Letters*, Vol. 39, No. 19, pp. 1363-1364, Sept. 2003.
- [Kra] J.D. Kraus and R.J. Marhefka, *Antennas*, New York, NY, McGraw-Hill, 2002, pp. 856-857.
- [Kum] R. Kumar and K.P. Ray, *Broadband Microstrip Antennas*. Norwood, MA: Artech House, Inc., 2003, pp. 30-52.
- [Lee1] Lee, Thomas H., *The Design of CMOS Radio-Frequency Integrated Circuits*, Cambridge University Press, 2nd edition, New York, NY, 2004.
- [Lee2] C.S. Lee and K.-H. Tseng, "Size reduction of microstrip antennas," *Electronic Letters*, Vol. 37, Issue 21, pp. 1274-1275, Oct. 11, 2001.
- [Lu] J.-H. Lu, "Broadband dual-frequency operation of circular patch antennas and arrays with a pair of L-shaped slots," *IEEE Transactions on Antennas and Propagation*, Vol. 51, No. 5, pp. 1018-1023, May 2003.
- [Mac1] S. Maci and G.B. Gentili, "Dual-frequency patch antennas," *IEEE Antennas and Propagation Magazine*, Vol. 39, Issue 6, pp. 13-20, Dec. 1997.
- [Mac2] S. maci, G.B. Gentili, and G. Avitabile, "Single-layer dual frequency patch antenna," *Electronic Letters*, Vol. 29, Issue 16, pp. 1441-1443, Aug. 5, 1993.

- [Mck] W.E. McKinzie, "A Modified Wheeler Cap Method for Measuring Antenna Efficiency," *Digest of 1997 IEEE Antennas and Propagation Society International Symposium*, Vol. 1, pp. 542-545, July 13-18, 1997.
- [Mil] T. A. Milligan, *Modern Antenna Design*. New York, NY: McGraw-Hill, 1985, pp. 95-105.
- [Nea] D.A. Neamen, *Electronic Circuit Analysis and Design*. Boston, MA: McGraw Hill, 2001, 2nd Edition, pp. 477-480.
- [Pap] I. Papapolymerou, R. F. Drayton, and L. P. B. Katehi, "Micromachined Patch Antennas," *IEEE Transactions on Antennas and Propagation*, Vol. 46, No. 2, pp. 275-283, Feb. 1998.
- [Pio] S. Pioch and J.-M. Laheurte, "Size reduction of microstrip antennas by means of periodic metallic patterns," *Electronics Letters*, Vol. 39, Issue 13, pp. 959-961, June 26, 2003.
- [Poz1] Pozar, David M., "Microwave and RF Design of Wireless Systems," John Wiley & Sons, Inc., New York, NY, 2001.
- [Poz2] D. Pozar and B. Kaufman, "Comparison of Three Methods for the Measurement of Printed Antenna Efficiency," *IEEE Transactions on Antennas and Propagation*, Vol. 36, No. 1, pp. 136-139, Jan. 1988.
- [Rab] Rabaey, J. M., Chandrakasan, A., Nikolic, B., "Digital Integrated Circuits," Prentice Hall Electronics and VLSI Series, Upper Saddle River, NJ, 2nd edition, pp. 4-10, 2003.
- [Rah] A. Rahman and R. Reif, "Thermal Analysis of Three-Dimensional (3-D) Integrated Circuits (IC's)," *Proceedings of the IEEE 2001 International Interconnect Technology Conference*, pp. 157-159, June 4-6, 2001.
- [Raj] K.Z. Rajab, R. Mittra, and M.T. Lanagan, "Size reduction of microstrip antennas using metamaterials," *2005 IEEE Antennas and Propagation Society International Symposium*, Vol. 2B, pp. 296-299, July 3-8, 2005.
- [Rog] S.D. Rogers, J.T. Aberle, D.T. Auckland, "Two-Port Model of an Antenna for Use in Characterizing Wireless Communications Systems Obtained Using Efficiency Measurements," *IEEE AP-S Intl. Symp.*, San Antonio, TX, pp. 730-733, June 16-21, 2002.

- [Rya] N.J. Ryan, B. Chambers, and D.A. Stone, "FDTD modeling of heatsink RF characteristics for EMC mitigation," *IEEE Transactions on Electromagnetic Compatibility*, Vol. 44, Issue 3, pp. 458-465, Aug. 2002.
- [Sch] L. Schaper, S. Burkett, M. Gordon, L. Cai, Y. Liu, G. Jampana, and I.U. Abhulimen, "Integrated System Development for 3-D VLSI," *Proceedings of the 57th Electronic Component and Technology Conference (ECTC)*, Reno, NV, pp. 853-857, May 29-Jun 1, 2007.
- [Sha] H. Shaukatullha, W. R. Storr, B. J. Hansen, M. A. Gaynes, "Design and Optimization of Pin Fin Heat Sinks for Low Velocity Applications," *Proceedings of the Twelfth Annual IEEE Semiconductor Thermal Measurement and Management Symposium (SEMI-THERM XII)*, pp. 151-163, March 5-7, 1996.
- [She] W. Shen and X. Zhou, "Dual frequency planar inverted-L patch antenna with identical isosceles triangles," *2005 IEEE Antennas and Propagation Society International Symposium*, Vol. 1B, pp. 528-531, July 3-8, 2005.
- [Wat] R.B. Waterhouse, *Microstrip Patch Antennas: A Designer's Guide*. Norwell, MA: Kluwer Academic Publishers, 2003.
- [Wat2] R. B. Waterhouse and S. D. Targonski, "Performance of microstrip patches incorporating a single shorting post," *Proceedings of the IEEE Antennas and Propagation Symposium*, pp. 29-32, July 1996.

BIOGRAPHICAL SKETCH

Lance Covert was born in Meridian, MS, on September 13, 1978. He attended the University of Alabama in Tuscaloosa, AL earning both bachelor's and master's degrees in electrical engineering in 2001 and 2003, respectively. He worked as a co-op engineer at Adtran, Inc. in Huntsville, AL. for two semesters while an undergraduate. In August 2003, he came to the University of Florida to pursue his Ph.D. in electrical engineering. For his Ph.D. research, he worked under Dr. Jenshan Lin in the Radio Frequency System-on-Chip group working on dual-function heatsink antennas for high-density 3-D integration of high-power transmitters (funded by the Air Force Research Laboratory).

Mr. Covert has 14 publications in technical journals and conferences. In conjunction with his antenna studies, Mr. Covert is also researching GaN-based microwave power amplifiers for high-density integration.

Mr. Covert was the course instructor for Electronics II at the University of Alabama in summer 2003. He has also been a teaching assistance and/or lab instructor for ten classes including Antenna Systems, Bipolar Analog IC Design, Electronics II, Microcontrollers, Digital Logic, Programmable Logic Controllers and Electric Circuits.